5-2014

Multidimensional Simulations of Non-linear Cosmic Ray Production in Supernova Remnant Evolution

Joshua Wood
Clemson University, jdwood@clemson.edu

Recommended Citation

Wood, Joshua, "Multidimensional Simulations of Non-linear Cosmic Ray Production in Supernova Remnant Evolution" (2014). *All Dissertations*. 1515.
https://tigerprints.clemson.edu/all_dissertations/1515

MULTIDIMENSIONAL SIMULATIONS OF NON-LINEAR COSMIC RAY PRODUCTION IN SUPERNOVA REMNANT EVOLUTION

A Dissertation
Presented to
the Graduate School of
Clemson University

In Partial Fulfillment
of the Requirements for the Degree
Doctor of Philosophy
Physics and Astronomy

---

by
Joshua D Wood
May 2014

Accepted by:
Dr. Dieter H Hartmann, Committee Chair
Dr. Mark Leising
Dr. Bradley Meyer
Dr. Jens Oberheide

Abstract

When a high-mass star ($\gtrsim 4\,M_\odot$) explodes at the end of its life, a supernova occurs, leaving its degenerate core and a fast-moving shell of matter, known as a supernova remnant (SNR). The SNR shell lasts for many thousands of years, generating emissions from low-frequency radio ($\sim 10^{-7}$ eV) up to γ-ray regime ($\sim 10^{15}\,$eV). It is also believed that SNRs are the predominant source of galactic cosmic rays, accelerating a population of thermal ions, primarily protons, up to relativistic energies by means of the diffusive shock acceleration (DSA) mechanism.

The small population of thermal (Boltzmann) particles, $\mathtt{p} \sim 10^{-3}$ eV, that are accelerated to relativistic energies, $\mathtt{p} \sim 10^{15}$ eV, extract a significant amount of energy from the SNR shell. The existence of a small but highly energetic population of non-thermal particles feeds back into the dynamic evolution of the SNR, which, in turn, affects the production of new particles and the continued acceleration of particles already swept up in the shock.

Much research has been done in investigating the case of particles accelerated in spherically symmetric SNRs; we present here the first simulations of supernova remnant evolution with non-linear cosmic ray feedback in multiple dimensions. The research here presents a new approach to an old problem, allowing for a deeper investigation into the role of cosmic ray production in supernova remnant environments.

The findings here show that, at the early stages of SNR evolution, the presence of cosmic rays in the shocks modifies the growth of hydrodynamic instabilities; severely damping the Rayleigh-Taylor instabilities in particular. We also find that the young remnant produces a strong TeV population of CRs that can generate TeV emissions that could be observed with or without the SNR interacting with an adjacent molecular cloud. However, the GeV emissions that could distinguish between the hadronic and leptonic population of CRs could not be observed by *Fermi-LAT* without the interacting molecular cloud.

Acknowledgments

First and foremost, I thank God the Father, through whom all things are, God the Son, through whom we are blessed, and God the Holy Spirit, through whom we gain Wisdom. Without Him, this research would be still in Dieter's mind.

I'd like to thank my family: my parents and my brothers & sisters. I thank you for not complaining (much) about my living and raising your grandchildren/nephew & nieces so far away from you. I promise I won't make my nieces and nephews call me "Uncle Doctor Josh" (or some variation therein).

My wife's family also deserves a multitude of thanks. Grandmom & Grandpop Cornely, Mom-mom & Pop-pop Schmidt, Mom & Dad, Tom, Marykate, Frank & Jenna and their children (Isabel, Neil, & Caleb) have been a tremendous cast of supporters for my goals.

To my children: Joseph, Colette, Rosemarie, & Kathleen. Watching you four grow has been an amazing experience, one that I hope you can replicate, but doing so has proved to be a strong inspiration to work hard. I hope my example can prove to be useful for you and/or your spouse.

I owe a lot to Ken-Ichi Nishikawa (UAH), Phil Hardee (UA), and Yosuke Mizuno (TITech) for their assistance in helping me learn computational hydrodynamics in my early days at Clemson. Their continued offering of help, including the use of TACC's Stampede cluster which I used for most of simulations contained here, has not gone unappreciated.

I'd like to thank Dieter who has dealt with my insistence on getting/writing codes before working on the physics for the last $5^{1}/_{2}$ years with a great deal of patience. I suppose that as long as you remember that Fortran $90^{+} > \mathrm{C}$, it will have been worth it.

Lastly, I am most gracious of my wife's infinite patience and her complete support of me and my ambitions. Her well-wishing, pushy comments, tears, and, most of all, love gave me the

strength to keep plowing through, despite my doubts and trials. This thesis is dedicated entirely to her. Rachel: you are the joy of my life, and I thank God for every day I have with you.

Table of Contents

List of Tables

List of Figures

Page

Chapter 1

Introduction

In this chapter, we will discuss the origin and historical development of the theory of cosmic rays, 1.1. In Section 1.2, we will discuss the method by which the cosmic ray particles can gain their extreme energies. Then, in Section 1.3, we outline the dissertation.

1.1 Cosmic Rays

1.1.1 Historical Perspective

At the end of the 1800's, it was observed that an electroscope would discharge in the presence of radioactive materials (Becquerel, 1896). An electroscope provides a measure of ionization by measuring the rate at which a charged gold-leaf returns to a neutral position after being discharged (see Figure 1.1); thus if the leaf returned to the neutral position it was due to an oppositely charged particle neutralizing the charge of the leaf (L'Annunziata, 2007; Falkenburg & Rhode, 2012).

Further observations showed that, even in the absence of radioactive materials, the electroscope could spontaneously discharge. Conventional thought at the time was that the background radiation was coming from the surface of the earth. Thus, as one increases in altitude, the expected ionization rate should decrease. However, Wulf (1910) showed that the ionization rate decreased at a slower rate, a 13% decrease at 300 m instead of the expected 27% decrease at that altitude. However, his conclusions were refuted by the investigation by Dominico Pacini (Pacini et al., 2011; Walter & Wolfendale, 2012).

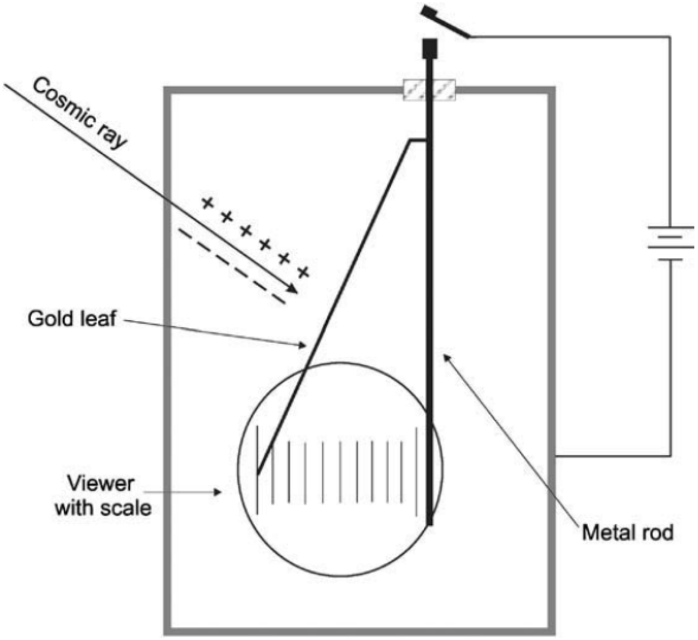

Figure 1.1: Schematic diagram of Rutherford's gold-leaf electroscope. As the (charged) cosmic ray particle comes into the vacuum chamber (the gray box), the ionized particle causes the leaf to be discharged, falling back towards the metal rod. Taken from L'Annunziata (2007)

In 1912, Victor Hess made his historical journey in a hot air balloon with three electroscopes (Hess, 1912), two of which measured the ionization rate of γ-rays with the third measuring β-particles. While increasing in altitude to a peak of ~ 5400 meters[1], Hess observed that the ionization rate was also increasing. Table 1.1 shows the data Hess collected in his flight for the detection of γ-rays.

Time	Height (m)	Appar. 1 $\left(\mathrm{cm}^{-3}\mathrm{s}^{-1}\right)$	Appar. 2 $\left(\mathrm{cm}^{-3}\mathrm{s}^{-1}\right)$
06:45 - 07:45	1,400	15.8	14.4
07:45 - 08:45	2,500	17.3	12.3
08:45 - 09:45	3,600	19.8	16.5
09:45 - 10:45	4,700	40.7	31.8
10:45 - 11:15	4,200	28.1	22.7
11:15 - 11:45	1,200	9.7	11.5
11:45 - 12:10	150	11.9	10.7
12:25 - 13:12	0	15.0	11.6

Table 1.1: Table of ionization rates as a function of height for flight 7, adapted from Hess (1912). The two data columns, Appar. 1 & 2, show the increase in ionization rate with height.

---

[1] The altitude fluctuated between 4400 and 5350 m, according to Hess' paper; the recorded values in Table 1.1 are the estimated mean values in the hour-long windows.

Hess called this radiation *Höhenstralung* ("radiation from above") as the results strongly suggested the radiation enters Earth's atmosphere from above, rather than emanating from the surface. Some of Hess's observations were made during the night, which also ruled out the sun as a possible source, leaving only cosmic sources. Robert Millikan coined the phrase "cosmic ray," believing that the ionizing radiation was made of photons and not matter (Millikan, 1925; Amato, 2014). Despite evidence showing that cosmic rays (CRs) are indeed highly energetic, charged particles (primarily protons, see Section 1.1.2), the name *cosmic ray* has persisted.

It wasn't until the early part of the 1930's that the remarkable proposal by Baade & Zwicky (Baade & Zwicky, 1934) brought to light a possible source for the high-energy CRs. Several years prior, the pair had discovered a new class of objects that they called super-novae (SNe), objects that were nearly as bright as their host galaxy; they proposed these objects were responsible for accelerating CRs Their argument relied on the energy output of supernova and the energy content in the observed cosmic rays.

The energy density of CRs is roughly $w_{cr} = 1\mathrm{eV/cm}^3$, which is of the same order of magnitude as thermal energy from stars and the magnetic field energy density (Parker, 1969; Gabici, 2011). If the particles are contained within the volume of the galactic disc, $V_D \approx 10^{67}\,\mathrm{cm}^3$, and remain there for a characteristic time-scale of $\tau \approx 10^7$ years before escaping the galaxy or destruction via collisions, then the required power to maintain a steady-state production of cosmic ray particles is,

$$L_{cr} = \frac{V_D \cdot w_{cr}}{\tau} \sim 10^{40}\,\mathrm{erg/s} \tag{1.1}$$

The SNe rate is roughly 2 per century; if each deposits the canonical 10^{51} ergs of kinetic energy, this amounts to $L_{SNe} \sim 10^{41}\,\mathrm{erg/s}$. Thus, if a SNe converts 10% of its kinetic energy into accelerating particles, then SNe alone can account for the production of CRs in the galaxy. Since this production should exist for a long duration, it is the supernova remnant (SNR) that should be the primary accelerator; see also Ginzburg & Syrovatskii (1964).

1.1.2 Modern Observations

The energies of CRs range from the MeV (Webber et al., 2011) to GeV/TeV (Panov et al., 2009; Adriani et al., 2013) and above the EeV range (Matthiae, 2010). The composition of these particles is primarily bare nuclei, accounting for approximately 98% of observed CRs; of this 98%, roughly 90% are protons, 9% are helium nuclei (α-particles) and the remaining 1% being heavier atoms (Schlickeiser, 2002; Olive & et al. (PDG), 2014), see also Figure 1.2.

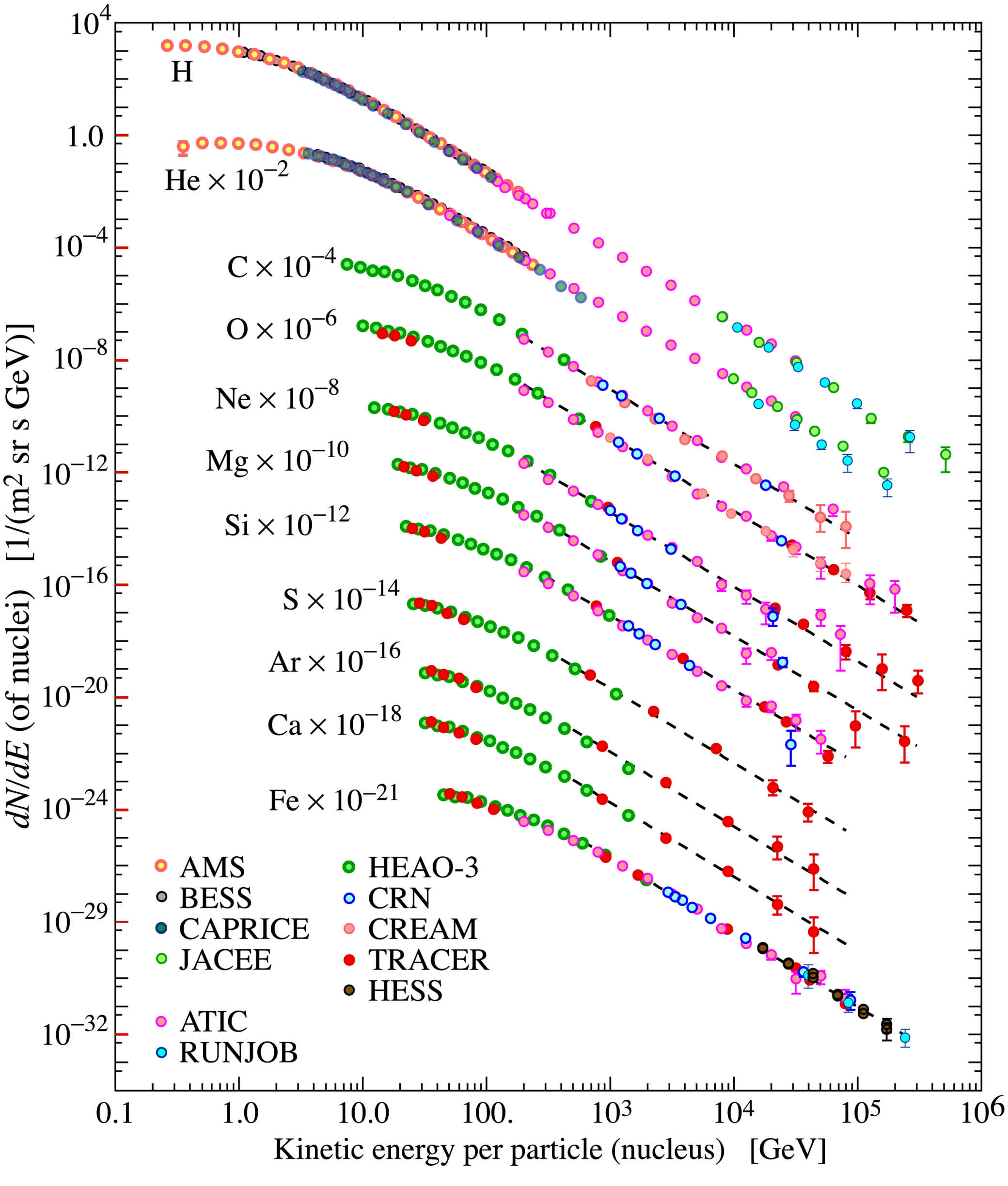

Figure 1.2: Fluxes of nuclei of the primary cosmic ray in particles/(energy/nucleus) as a function of energy/nucleus. The heavier nuclei have been scaled to fit on the plot. Taken from (Olive & et al. (PDG), 2014).

With these energies, and assuming a background magnetic field of $B \sim 1\,\mu G$, the gyroradius of a CR proton ranges from 10^{11} cm (roughly an AU) to 10^{24} cm (roughly a megaparsec); this indicates that particles with energies above 10^{18} eV must be extra-galactic in origin as the gyroradius is roughly a kiloparsec, a length that is larger than the height of the galactic disk.

As CRs are charged particles, they are reflected by the galactic magnetic field, disassociating their measured trajectory from their source (Strong et al., 2007). The observed energy spectrum follows a broken power-law,

$$J(E) \propto \begin{cases} E^{-2.7} & 10^{10}\mathrm{eV} < E \lesssim 10^{15}\mathrm{eV} \\ E^{-3.0} & 10^{15}\mathrm{eV} \lesssim E \lesssim 10^{18}\mathrm{eV} \end{cases} \tag{1.2}$$

as seen in Figures 1.2 and 1.3. This suggests that a single source is responsible for the acceleration to these high energies.

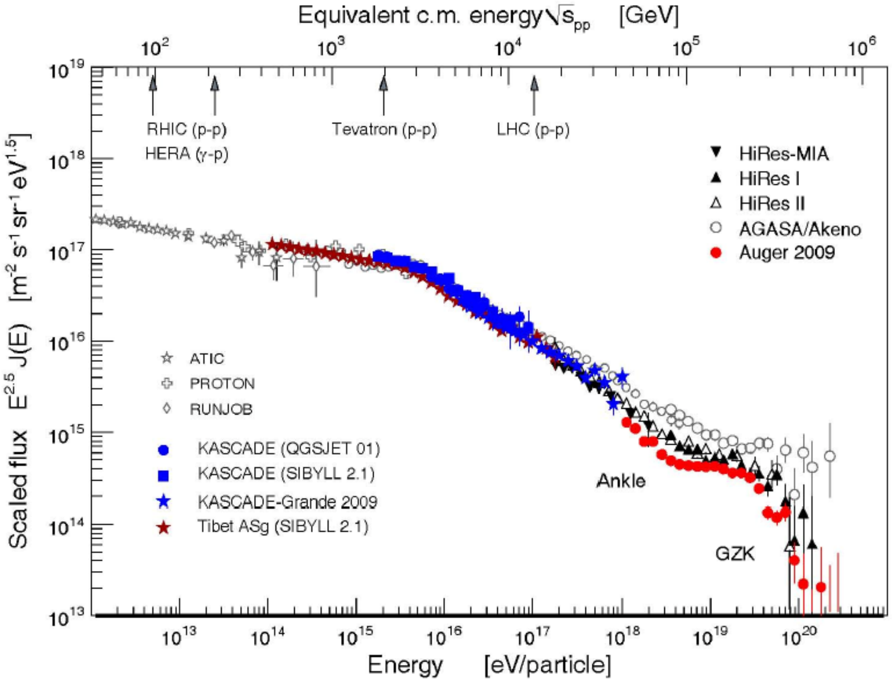

Figure 1.3: Cosmic ray spectrum above 1 GeV, from Matthiae (2010). The transition from galactic to extragalactic sources begins around the knee at $E \sim 3 \times 10^{15}$ eV.

The transition between the two cases is called the *knee* while the transition above 10^{18} eV is called the *ankle*. At the highest energies is the Greisen-Zatsepin-Kuz'min limit (GZK limit, Greisen (1966); Zatsepin & Kuz'min (1966)). This limit is the maximum energy of a CR before interactions with cosmic microwave background photons become possible, thereby destroying the particles; this limit is calculated to be $E = 5 \times 10^{19}\,\mathrm{eV}$. Despite this, particles with energies exceeding this limit have been observed, including the famous *Oh-my-God particle* (Linsley, 1963) with an energy $E \sim 3 \times 10^{20}\,\mathrm{eV}$.

At the lower end of the CR energy spectrum, in the MeV and GeV range, direct observations of CRs can be done by using calorimeters, scintillators and/or spectrometers on space-borne instruments, such as the Alpha Magnetic Spectrometer (AMS, Aguilar et al. (2013)), or balloon-borne instruments, such as the Advanced Thin Ionization Calorimeter (ATIC, Panov et al. (2009)). When a CR particle collides with a particle in Earth's atmosphere, the photons present in the resulting cascade of subatomic particles (which include electrons, muons and pions) can be detected with imaging air Cherenkov telescope (IACT) detectors, such as the High Energy Stereoscopic System (H.E.S.S., Aharonian et al. (1997)) into the TeV range.

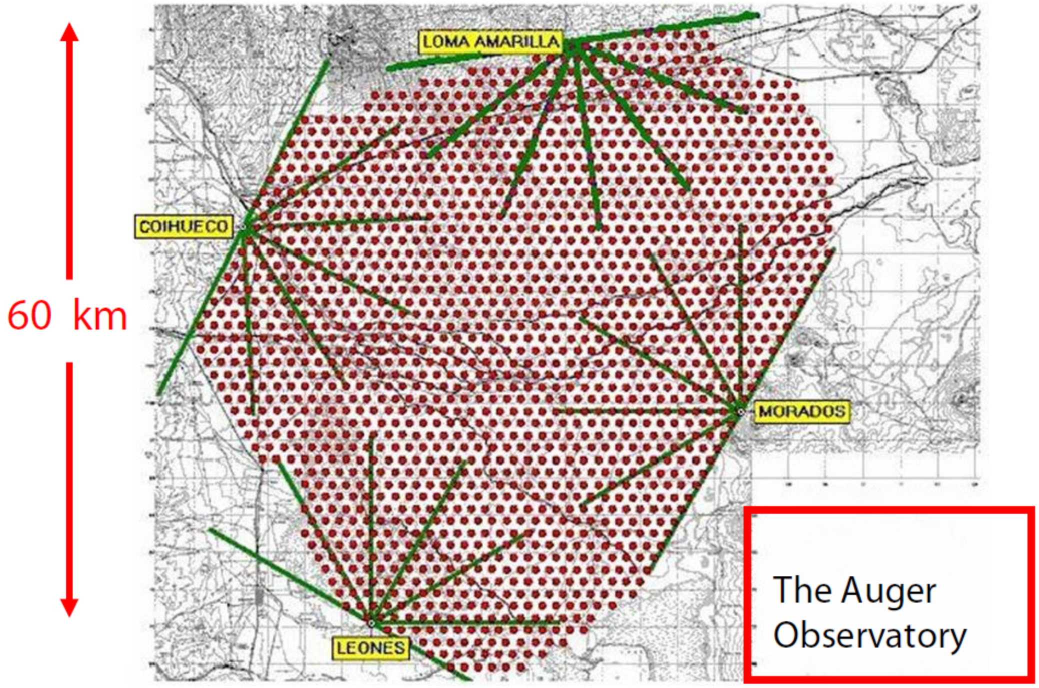

Figure 1.4: Sketch of the Pierre Auger Observatory site. The red dots indicate a water Cherenkov detector; the four labeled locations are the fluorescence sites with the green lines indicating their field of view. From Matthiae (2010).

Above this range, direct measurements of CRs rely on the aforementioned air showers, as the small fluxes ($<$ 1 particle per square-meter per year for $E >$ PeV) and small collector sizes of space-borne instruments cannot regularly detect CR particles. Small scintillator arrays ($A \sim (200\,\mathrm{m})^2$), such as Karlsruhe Shower Core and Array Detector (KASCADE, Antoni et al. (1999)), can be used to detect the muons and electrons produced in CR air showers, produced by CR primaries with energies in the PeV and EeV range. At the highest energies, $10^{18}\,\mathrm{eV}$ to $10^{20}\,\mathrm{eV}$, air fluorescence techniques, as used by High Resolution Fly's Eye (HiRes, Matthews (2001)) and Akeno Giant Air Shower Array (AGASA, Hayashida et al. (1994)), and water Cherenkov detectors, such as the Pierre Auger Observatory (Matthiae, 2010) (see Figure 1.4), can be used to detect the subatomic particles in the air showers.

In addition to the direct measurement of CR, indirect measurements of reactions involving them can be made. For leptonic CRs (electrons), bremsstrahlung and inverse Compton processes eject a γ-ray photon; for the hadronic CRs (protons, ions), collisions with ambient protons can produce either neutral pions, π^0, or charged pions, $\pi^\pm$, via interactions (Schlickeiser (2002); Reynolds (2008); see also Section 2.6), such as

$$p + p \rightarrow \begin{cases} p + p + \pi^0 \\ p + n + \pi^+ . \end{cases} \tag{1.3}$$

The pions produced in the above interactions quickly decay to[2]

$$\begin{aligned} &\pi^0 \rightarrow 2\gamma \\ &\pi^+ \rightarrow \mu^+ + \nu_\mu \end{aligned} \tag{1.4}$$

where the two γ's in the first interaction have an energy in the pion rest-frame of $E_\gamma = m_{\pi^0}/2 \sim 70\,\mathrm{MeV}$. The muons produced in the decay of the charged pion will further decay into neutrinos and electron or positrons. For typical assumptions of hadronic acceleration, approximately 8 γ-ray photons are produced for every three neutrinos (Kelner et al., 2006; Kappes et al., 2007).

The photons generated from the decay of the neutral pion can then traverse from their source unimpeded, where a high-energy photon detector, such as *Fermi-LAT* (Atwood et al., 2007) or H.E.S.S. (Aharonian et al., 1997), would be able to measure the particle's energy and trajectory. Figure 1.5 shows an emission map of γ-ray photons ($E_\gamma > 1\,\mathrm{GeV}$), as detected by *Fermi-LAT*, with point sources pulled from the H.E.S.S catalog that are known to be within the galaxy.

---

[2] The two decay modes shown are the largest branching ratios for those particles, each with $BR > 0.988$; there are other decay channels.

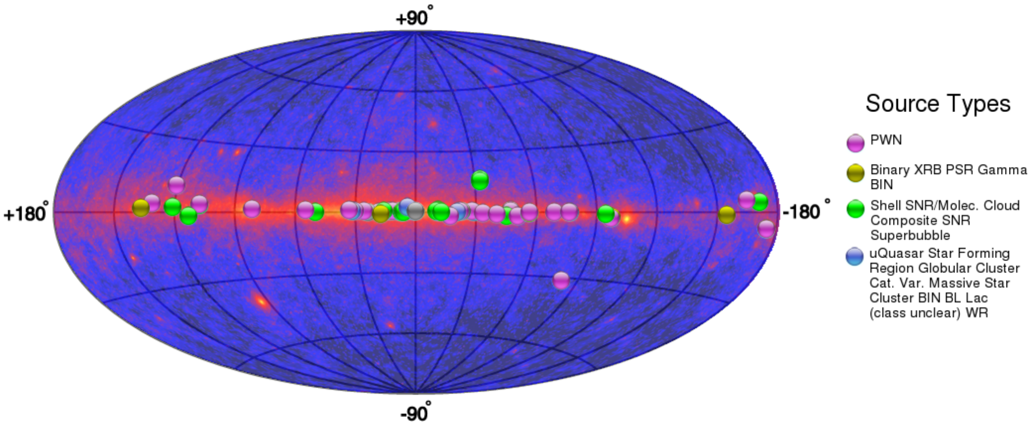

Figure 1.5: All-sky map of galactic point sources detected by H.E.S.S telescope array overlaid onto an all-sky map of the diffuse γ-ray emission as observed by *Fermi-LAT*. The types of points sources are described in the legend. Image credit: http://tevcat.uchicago.edu/

Due to the shape of the galaxy (Gerhard, 2002; Churchwell et al., 2009) and our location within it, it should be expected that the distribution of SNRs lies primarily along the galactic plane, as seen in Figure 1.5. A catalogue of galactic SNRs has been compiled (Green, 2014), as can be seen in Figure 1.6 below. The catalogue contains information, such as sizes and the types, on over 250 known galactic SNRs from radio observations, X-ray observations, γ-ray observations, and combinations thereof. A second catalog (Ferrand & Safi-Harb, 2012) contains over 310 objects measured in the X-ray and γ-ray energies, including pulsars and neutron stars in addition to the SNRs.

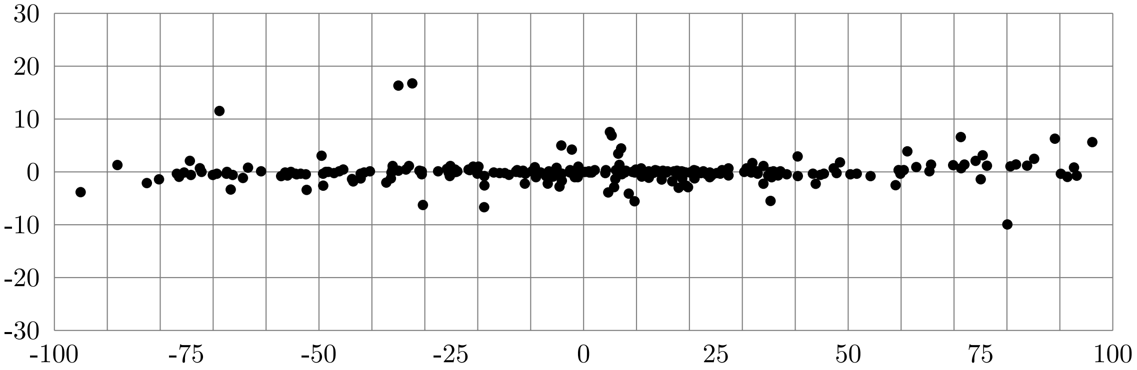

Figure 1.6: Zoom-in of the observed distribution of Galactic SNRS. Data selected from Green (2014), rejecting only the SNRs outside of the range $[-100, 100] \times [-30, 30]$.

1.1.3 Limiting Energies

As particles are accelerated, the gyroradius increases as well[3], $R_L \propto \mathtt{p}c$. As the gyroradius increases, it becomes increasingly difficult to confine the particle in the magnetic field of the accelerator. It then follows that there is some maximum energy that the particle can obtain while being accelerated; this maximum is given by (Hillas, 1984)

$$E_{max} \simeq 10^{15} Z \beta B_{\mu G} R_{L,pc} \text{ eV} \tag{1.5}$$

where Z is the atomic number, β the relative velocity of the particle, $B_{\mu G}$ is the magnetic field in units of micro-Gauss and $R_{L,pc}$ is the gyroradius in units of parsecs. Figure 1.7 depicts the required magnetic field strengths and gyroradii required for a proton of energy $E = 10^{15}$ eV (blue line) and $E = 10^{20}$ eV (red line). Any object *above* the line has the capability of accelerating a proton to those energies. As evidenced on the figure below, SNRs are capable of accelerating particles up to the knee ($E \sim 10^{15}$ eV).

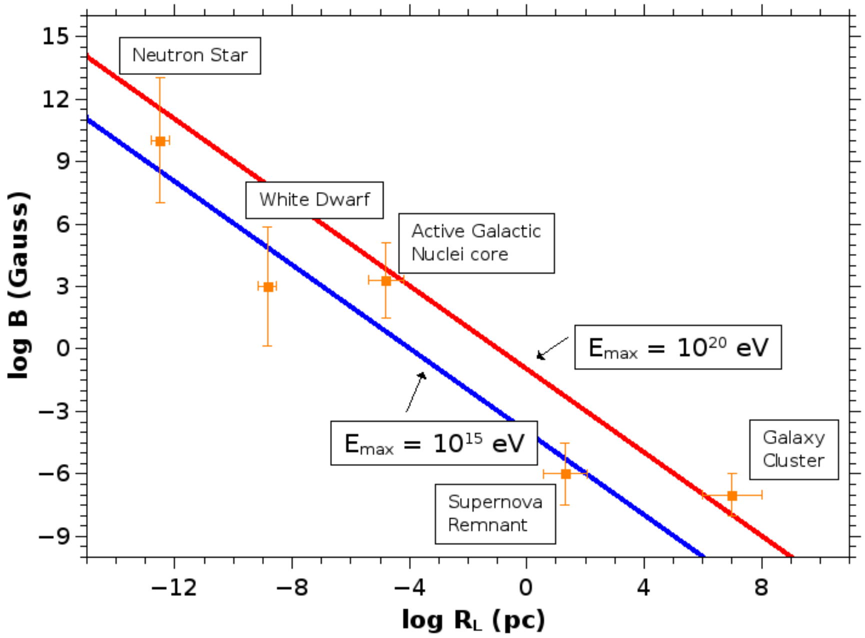

Figure 1.7: Hillas criteria for a proton with $v = c$; the points designate fiducial values of B and R for various astrophysical objects while the error bars represent the ranges of values.

---

[3] We will use $\mathtt{p}$ to denote the particle momentum and, later, p to denote gas pressures (typically with a subscript as well).

1.2 Acceleration Mechanism

1.2.1 Fermi Acceleration

The proposed mechanism of accelerating particles from thermal velocities to relativistic speeds is through the Fermi process. In this mechanism, we consider a collisionless shock, a discontinuous shift in physical states in which the mean-free-path of collisions is larger than the system, with the upstream region moving with velocity u_1 and the downstream region moving with velocity u_2 ($u_1 \gg u_2$). The magnetic field in the shock region is expected to be highly turbulent, leading to scattered motions of particles co-moving with the shock, see Figure 1.8.

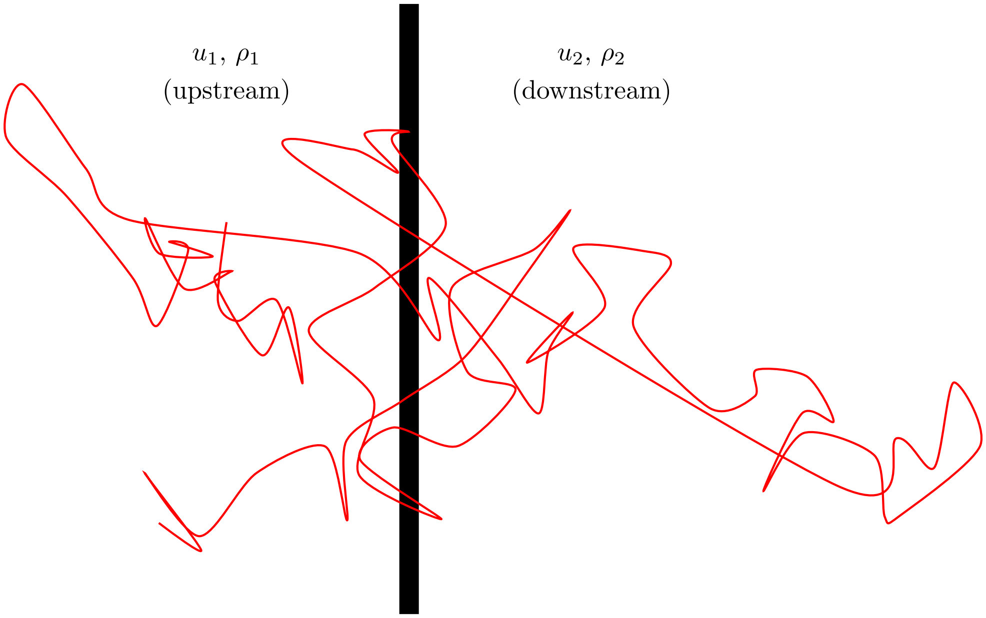

Figure 1.8: Graphical representation of a particle's trajectory as it scatters off a tangled magnetic field at the interface of a shock (thick black line).

Each time the particle crosses the shock front, it gains energy

$$E_1 = (1 + \alpha)E_0 \tag{1.6}$$

where $\alpha \propto u_1 - u_2$ is the fraction energy gain per crossing. If the crossing is repeated k times, the total energy after those k crossings is

$$E_k = (1 + \alpha)^k E_0. \tag{1.7}$$

For particles diffusing across the shock, the return probability depends on the downstream velocity:

$$P_{ret} \equiv 1 - \sigma u_2 \tag{1.8}$$

where $\sigma = \rho_1/\rho_2$ is the compression ratio, $\sigma = 4$ for the case of an ideal gas, with $\gamma = 5/3$, and a strong shock. After k crossings, the number of particles remaining is

$$N_k = N_0 P_{ret}^k \tag{1.9}$$

The differential particle population can be determined by manipulating Equations 1.7 and 1.9 to give a natural power-law function in E[4]:

$$\frac{dN}{dE} \propto \left(\frac{E}{E_0}\right)^{s-1} \tag{1.10}$$

where $s = \ln P_{ret} / \ln(1+\alpha)$. For $\sigma = 4$, we obtain $s = -1$, giving a slope of -2. This is reasonably close to the observed power law in the spectrum seen in Figure 1.3; the remaining difference can be accounted for in the propagation of the particles in the galaxy (Caprioli et al., 2010b).

1.2.2 Diffusive Shock Acceleration

The Fermi process can be modeled by the mathematical framework called *diffusive shock acceleration* (O'C Drury, 1983; Kirk, 1994; Malkov & O'C Drury, 2001). In this mechanism, we describe the particle population with a phase-space distribution, $f(\mathbf{p}, \mathbf{x}, t)$; the transport of the particles can then be modeled by the Lagrangian diffusion equation:

$$\frac{df}{dt} = \nabla \cdot (D \nabla f) \tag{1.11}$$

where $D = v r_g^2 / l_{coh}$ is the diffusion coefficient with particle speed v, r_g the particle gyroradius, and l_{coh} the coherence length of the magnetic field. When $l_{coh} \sim r_g$, we obtain the oft-used Bohm diffusion coefficient. As the diffusion coefficient depends on the magnetic field, it mimics the interaction of the Fermi process.

As the particles flow along with the moving shock, the bulk motion of the fluid must be

---

[4] See Appendix B for the derivation of this from the above and the value $s = -1$ claimed.

accounted for, modifying the above to

$$\frac{\partial f}{\partial t} + \mathbf{u} \cdot \nabla f = \nabla \cdot (D \nabla f) \tag{1.12}$$

where $\mathbf{u}$ is the fluid velocity. In order to conserve energy in the process, we need a term that represents the adiabatic change in energy associated with the compression and expansion of the cosmic ray gas. Following Parker (1969)[5], the above becomes

$$\frac{\partial f}{\partial t} + \mathbf{u} \cdot \nabla f = \nabla \cdot (D \nabla f) + \frac{1}{3} (\nabla \cdot \mathbf{u}) \, \mathtt{p} \frac{\partial f}{\partial \mathtt{p}} \tag{1.13}$$

Formally, there is also a source term, $\mathcal{Q}(\mathtt{p}, \mathbf{x}, t)$ that should be included in Equation 1.13, but we will ignore it for now, and hold off the discussion of it until Section 3.2.2.

In order to connect the DSA model to the Fermi process, we analyze Equation 1.13 in one-dimension for the steady-state solution:

$$u \frac{\partial f}{\partial x} = \frac{1}{3} \left(\frac{\partial u}{\partial x} \right) \mathtt{p} \frac{\partial f}{\partial \mathtt{p}} \tag{1.14}$$

which has a solution

$$f = f_0(\mathtt{p}) + f_1(\mathtt{p}) \frac{\mathtt{p}_x}{\mathtt{p}} \tag{1.15}$$

By matching boundary conditions at the shock, we obtain

$$\left[f_1 - \frac{u_1}{c} \mathtt{p} \frac{\partial f}{\partial \mathtt{p}} \right]_{up} = \left[f_1 - \frac{u_2}{c} \mathtt{p} \frac{\partial f}{\partial \mathtt{p}} \right]_{down} \tag{1.16}$$

In the downstream region, we expect that $f_1 = 0$ because the distribution of particles should be isotropic. In the upstream region, we expect $f_1 = 3 f_0 \, (u_1/c)$. Inserting this into the above, we obtain

$$(u_1 - u_2) \, \mathtt{p} \frac{\partial f}{\partial \mathtt{p}} = -3 u_1 f_0 \tag{1.17}$$

For the case of a strong shock, $u_1 = 4u_2$, which indicates that $f_0 \propto \mathtt{p}^{-4}$. The distribution $f(\mathtt{p}, \mathbf{x}, t)$

---

[5] Gleeson & Axford (1967) derive another elegant form of Parker's transport equation, but choose to work with the particle's kinetic energy, T, rather than the momentum $\mathtt{p}$.

is then related to the observed spectrum, dN/dE, via the integral over the momentum space:

$$\frac{dN}{dE} \propto \int f\left(\mathtt{p}, \mathbf{x}, t\right) \mathtt{p}^2 d\mathtt{p} \propto \mathtt{p}^{-2} = E^{-2} \tag{1.18}$$

From the relativistic relation $E \sim \mathtt{p}c$, we see that the diffusive shock acceleration mechanism also produces the characteristic E^{-2} power-law slope that the Fermi mechanism produces.

1.2.3 CR Diffusion

The diffusion coefficient in 1.13 is typically spatially dependent, $D = D\left(\mathtt{p}, \mathbf{x}, t\right)$, where the spatial dependence is satisfied through the magnetic field, similar to the treatment by Bohm. In the low-momentum limit, we expect $D \propto \mathtt{p}^2$ and in the high-momentum limit, $D \propto \mathtt{p}$ (Kang et al., 2000). These two limits and the magnetic field dependence give rise to a diffusion coefficient of the form,

$$D\left(\mathtt{p}, \mathbf{x}, t\right) = \frac{D_0}{B(\mathbf{x}, t)} \frac{z^2}{\sqrt{1+z^2}} \tag{1.19}$$

where D_0 is the diffusivity, $B(\mathbf{x}, t)$ is the magnitude of the magnetic field, and $z = \mathtt{p}/mc$. However, Malkov (1999) showed that for non-linear shock acceleration, as long as the particle diffusivity grows faster than $\sqrt{\mathtt{p}}$, the case over the whole range of momenta considered, the energy spectrum becomes independent of the shock compression.

As particles gain energy, they are capable of diffusing out further from the shock that accelerated it. As these higher-energy particles do so, their presence modifies the ambient, effectively warning the plasma of the oncoming shock by heating it and thereby modifying the shock structure (see Section 2.5). As this heating process increases the downstream temperature, the injection momentum will also be increased; however, the lower energy particles are virtually unaffected by this heating process.

The changes to the shock structure (Kirk, 1994; Jun & Jones, 1997) also changes the spectrum such that it is no longer defined by a single power-law (Kang et al., 2009; Caprioli et al., 2010a). Instead, the spectrum becomes curved and, in the case of the steady-state solution, takes the form

$$f(\mathtt{p}, t) \sim \left[f_0 \left(\frac{\mathtt{p}}{\mathtt{p}_{inj}} \right)^{-q_0} + f_1 \left(\frac{\mathtt{p}}{\mathtt{p}_{max}(t)} \right)^{-q_1} \right] \exp\left[- \left(\frac{\mathtt{p}}{\mathtt{p}_{max}(t)} \right)^{\alpha} \right] \tag{1.20}$$

where the constants depend on the shock conditions, the amplitude f_0 is the Maxwellian value at

$\mathtt{p} = \mathtt{p}_{inj}$, and the amplitude f_1 can be determined by the condition that $f_s(\mathtt{p}_{max}) \propto \mathtt{p}_{max}^{-4}$. In the general case, the spectrum becomes flatter at the higher energies where the shock compression ratio increases due to the preheating.

1.3 Research Goal

There have been many successful models produced of CR production in SNR shocks, such as Ellison & Bykov (2011) and Caprioli et al. (2010a). However, these models remain one-dimensional[6] for the fact their interests lie in reproducing the X-ray spectra of observed remnants, such as SNR RX J1713.7-3946 (Muraishi et al., 2000; Ellison et al., 2010), under the assumption of non-equilibrium ionization due to significantly increased computation times (see Teşileanu et al. (2008) for details on the numerics of this assumption).

The models put forth by Kang et al. (2002) and Jones & Kang (2005), while also focusing in planar shocks and spherically symmetric models, introduce adaptive mesh refinement (see Section 3.1) into the momentum-space of the particle distribution while focusing primarily on the structure of shock interactions (Jun & Jones, 1997; Kang et al., 2009), though some of their more recent interests have been in the radiation from CR-modified shocks (Edmon et al., 2011; Kang et al., 2012)

One of the first goals of this thesis is to study the role of knot-formation in the production of cosmic rays. The knots in supernova remnants develop due to instabilities in the fluids, particularly the Rayleigh-Taylor instability (Chevalier & Klein, 1978; Blondin & Ellison, 2001). There have been some studies into this instability in the presence of efficient particle acceleration (e.g., Blondin & Ellison (2001), Ferrand et al. (2010), and Fraschetti et al. (2010)), however, these studies mimicked the particle acceleration by modifying the adiabatic index, γ, to be less than the ideal gas value of $\gamma = 5/3$, rather than incorporating an active cosmic-ray production mechanism[7].

As SNR shocks are a site for accelerating protons, there should be some observational signature of the hadronic cosmic rays due to interactions of the accelerating particles and the thermal population of protons in the ambient ISM & SNR shell. The sensitivity of *Fermi-LAT* requires a molecular cloud to be near the SNR to provide a high-density target for the detection of the π^0-

---

[6] Formally, it is spherically symmetric with dependence in only one direction, r.

[7] In the case of Ferrand et al. (2010) and Fraschetti et al. (2010), the adiabatic index is turned into a hydrodynamic variable so it is dynamically changing, rather than the static-value approach taken by Blondin & Ellison (2001).

decay signature. We investigate the possibility of a *residual* pion spectrum that should exist around a “naked” SNR (one without a nearby molecular cloud) and the observational requirements therein to observe this emission.

Chapter 2

Supernova Remnant Evolution

In this chapter, we present the background theory on the dynamic evolution of supernova remnants (Section 2.1), the methods of modeling these objects (Sections 2.2, 2.3, 2.4), the role of cosmic ray production in the shocks (Section 2.5), and the observational signatures of these extreme explosions (Section 2.6).

2.1 SNR Evolutionary Phases

At the end of a massive[1] star's life, it explodes with a kinetic energy of $\sim 10^{51}$ ergs, roughly one percent of the total binding energy of the stellar collapse[2]. As the stellar ejecta progress outwards in the ambient medium, the remnant can be characterized in three distinct phases: (a) the free expansion phase, (b) the energy conserving phase, (c) the momentum-conserving phase. Each of these will be discussed below.

In the first phase of supernova remnant evolution, the free expansion phase, the shock wave generated by the explosion moves into an approximately homogeneous interstellar medium (ISM) with a very large Mach number ($M > 100$). Assuming that the initial energy, E_0, of the explosion is purely kinetic, then the maximum velocity is

$$v_{ej} = \left(\alpha \frac{2E_0}{M_{ej}} \right)^{1/2} \tag{2.1}$$

---

[1] The lower limit of "massive" is not well defined, ranging from $5M_\odot$ to $8M_\odot$, depending on the author.

[2] The other 99% are released in the form of neutrinos; see Rampp (2000).

where α is a constant that depends on the parametrization of the SNR density (Truelove & McKee, 1999). The shock radius scales as

$$R(t) = v_{ej}t = \left(\alpha \frac{2E_0}{M_{ej}}\right)^{1/2} t \tag{2.2}$$

The ISM gas is separated from the ejecta by a contact discontinuity, a surface where the pressure and velocity are approximately equal but with differing densities–this is unlike a shock in which all three quantities would change. Behind this contact discontinuity, a reverse shock develops in the ejected material. Ahead of the contact discontinuity, the ISM gas is being compressed to form a thin shell.

When the mass of the accumulated matter on the shell is approximately equal to the mass of the initial explosion, it enters the energy-conserving phase (often called the Sedov phase). In this phase, the position of the forward shock can be given by

$$R(t) = \beta E_{51}^{1/5} n_0^{-1/5} t_5^{2/5} \text{ pc} \tag{2.3}$$

where $E_{51} = E_0/10^{51}\,\text{erg}$, $t_5 = t/10^5\,\text{yr}$, $n_0 = n/10^0\,\text{cm}^{-3}$ and β a constant of $\mathcal{O}(1)$.

The amount of energy lost due to radiation is negligible up to this phase. However, as the remnant ages, the accumulated losses become significant. It is around this time that the remnant enters the third phase, the momentum-conserving phase (sometimes called the snow-plow phase). The momentum conditions requires

$$\frac{4\pi}{3} R^3 \frac{dR}{dt} = \frac{4\pi}{3} R_0^3 v_0 \tag{2.4}$$

which integrates to give

$$R(t) = R_0 \left[1 + 4\frac{v_0}{R_0}(t - t_0)\right]^{1/4} \tag{2.5}$$

where R_0 and v_0 are the location of forward shock via Equation 2.3, and velocity, respectively, at time $t = t_{rad} \simeq 10^4 E_{51}^{4/17} n_0^{-9/17}$ years (Blondin et al., 1998). Once the velocity of the forward shock is approximately equal to the sound speed of the ISM, $c_s^2 = \gamma p/\rho$, the SNR is no longer distinguishable from the ISM. This occurs after

$$t_{fade} \approx 10^6 E_{51}^{27/85} n^{-31/85} \left(\frac{c_s}{10\,\mathrm{km/s}} \right)^{-7/5} \text{ yr} \tag{2.6}$$

Figure 2.1 shows the the position of the forward shock of an SNR as a function of time, combining all three phases, where $E_0 = 10^{51}$ erg, $M_{ej} = 4\,M_\odot$, and $n = 1$ cm^{-3}.

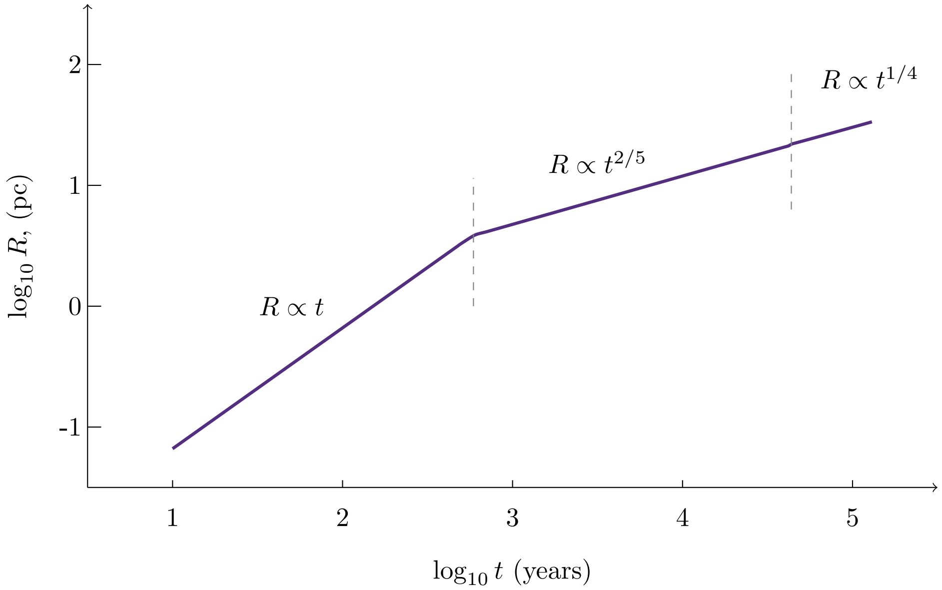

Figure 2.1: Position of the forward shock as a function of time, showing the different phases of the SNRs life. The dashed gray lines indicate the approximate separations between regimes.

2.2 Hydrodynamics

Being very hot plasmas, supernova remnant ejecta can be well modeled using the (ideal) Eulerian hydrodynamic equations,

$$\frac{\partial \rho}{\partial t} + \nabla \cdot \boldsymbol{\pi} = 0 \tag{2.7a}$$

$$\frac{\partial \boldsymbol{\pi}}{\partial t} + \nabla \cdot (\mathbf{u} : \boldsymbol{\pi} + p_{gas}\mathbf{I}) = 0 \tag{2.7b}$$

$$\frac{\partial E}{\partial t} + \nabla \cdot (\mathbf{u}E + \mathbf{u}p_{gas}) = 0 \tag{2.7c}$$

where ρ is the mass density, $\boldsymbol{\pi} = \rho\mathbf{u}$ is the momentum density, p_{gas} is the gas pressure, $\mathbf{I}$ is the identity tensor, and

$$E = \frac{1}{2}\frac{\boldsymbol{\pi}\cdot\boldsymbol{\pi}}{\rho} + \frac{p_{gas}}{(\gamma - 1)}$$

is the total energy[3] with γ the adiabatic index. The equations represent the mass conservation, momentum conservation, and energy conservation respectively. We also denote $\mathbf{u} : \boldsymbol{\pi}$ to indicate the dyad product, defined by

$$\mathbf{a} : \mathbf{b} = \begin{pmatrix} a_1b_1 & a_1b_2 & a_1b_3 \\ a_2b_1 & a_2b_2 & a_3b_3 \\ a_3b_1 & a_3b_2 & a_3b_3 \end{pmatrix} \tag{2.8}$$

2.2.1 Blast Waves

We first consider the Euler equations for a symmetric (planar, cylindrical or spherical) system. Rather than using the conservative form of Equation 2.7, we opt for the primitive form,

$$\frac{\partial\rho}{\partial t} + u\frac{\partial\rho}{\partial r} + \rho\left(\frac{\partial u}{\partial r} + \frac{su}{r}\right) = 0 \tag{2.9a}$$

$$\frac{\partial u}{\partial t} + u\frac{\partial u}{\partial r} + \frac{1}{\rho}\frac{\partial p}{\partial r} = 0 \tag{2.9b}$$

$$\frac{\partial p}{\partial t} + u\frac{\partial p}{\partial r} - \rho c_s^2\left(\frac{\partial u}{\partial t} + u\frac{\partial su}{\partial r}\right) = 0 \tag{2.9c}$$

where $c_s^2 = \gamma p/\rho$ is the square of the speed of sound and $s \in (0, 1, 2)$ represents the geometry (planar, cylindrical, spherical, respectively).

We can then consider simple scaling relations:

$$u \equiv \dot{R}U(\eta), \qquad \rho \equiv \rho_0\Omega(\eta), \qquad p = \rho_0\dot{R}^2P(\eta) \tag{2.10}$$

where η is the scaled coordinate, ρ_0 a constant, and U, Ω, P are functions that give the shape of the solution for all time and space. We can then recognize that

$$\frac{\partial h(\eta)}{\partial t} = \frac{\partial h}{\partial\eta}\frac{\partial\eta}{\partial t} = -\eta\frac{\dot{R}}{R}h' \tag{2.11}$$

$$\frac{\partial h(\eta)}{\partial r} = \frac{\partial h}{\partial\eta}\frac{\partial\eta}{\partial r} = \frac{1}{R}h' \tag{2.12}$$

---

[3] $p_{gas} = (\gamma - 1)E$ being the ideal gas equation of state, connecting the pressure to the internal energy.

which allows us to write Equation 2.9 as

$$[U-\eta]\,\Omega' + \Omega U' + \frac{s}{\eta}U\Omega = 0 \tag{2.13a}$$

$$\frac{R\ddot{R}}{\dot{R}^2}U\Omega + [U-\eta]\,U'\Omega + P' = 0 \tag{2.13b}$$

$$2\frac{R\ddot{R}}{\dot{R}^2}P + [U-\eta]\left[P' - \gamma P\frac{\Omega'}{\Omega}\right] = 0 \tag{2.13c}$$

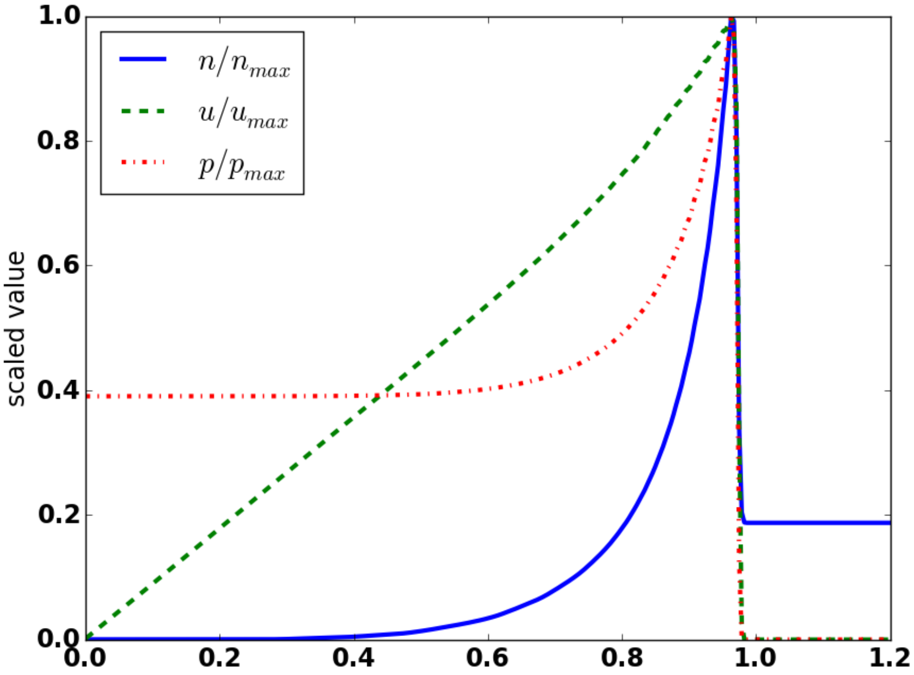

Figure 2.2: The evolution of the 1D blast wave due to an over-pressure in a very small region. All values are scaled to peak values at $r \simeq 1$.

For the blast wave problem, we can argue from dimensional analysis that

$$R(t) = \xi\left(\frac{Et^2}{\rho}\right)^{1/5} \tag{2.14}$$

where ξ is a constant that can be determined from the units chosen. The above scaled equations then reduce to[4],

$$[U-\eta]\,\Omega' + \Omega U' + \frac{s}{\eta} U\Omega = 0 \tag{2.15a}$$

$$-\frac{3}{2} U\Omega + [U-\eta]\,U'\Omega + P' = 0 \tag{2.15b}$$

$$-3P + [U-\eta]\left[P' - \gamma P \frac{\Omega'}{\Omega}\right] = 0 \tag{2.15c}$$

These equations show an independence on the scale of the physical system. A nuclear bomb exploding above the New Mexico will expand in the same manner as a star exploding in space.

As an example, consider the domain $r \in [0,2]$ of a stationary uniform density, $\rho = 1$ and pressure, $p \sim 10^{-5}$, and place an over-pressure, $p \sim 10^{2}$, in a very small region, $r \leq 10^{-2}$. Evolving these variables using Equations 2.15 (or similarly Equations 2.7), then the result is the classic Sedov blast-wave (Sedov, 1946; Taylor, 1955). At a time $t = 1$, the (scaled) values appear as in Figure 2.2.

2.3 n-Dimensional Hydrodynamics

In moving from one dimension into two or three dimensions, minor perturbations in the fluid flow can lead to unsteady growth, resulting in instabilities. Of particular importance in astrophysical fluids are the Rayleigh-Taylor, the Kelvin-Helmholtz, and Richtmyer-Meshkov instabilities. Each of these will be discussed in turn.

2.3.1 Rayleigh-Taylor Instability

The Rayleigh-Taylor instability (RTI) occurs when two fluids of differing densities are placed on top of one another under a constant gravity. In this case, the momentum conservation equation is modified to account for the gravitational force:

$$\frac{\partial \boldsymbol{\pi}}{\partial t} + \nabla \cdot (\boldsymbol{\pi} : \mathbf{u} + p\mathbf{I}) = \rho \mathbf{g} \tag{2.16}$$

where $\mathbf{g}$ is the constant gravitational acceleration.

By placing the more dense fluid atop the less dense fluid, the force of gravity, after the introduction of minor perturbations at the interface, causes “fingers” to develop as the fluids begin

---

[4] Appendix C shows the derivation from Equation 2.9 to the Equation 2.15.

to mix. As the effects of gravity and acceleration (in the opposite direction) are indistinguishable, the instability also grows when the less dense fluid accelerates into the more dense fluid. This latter condition is often satisfied in systems with extreme pressure (temperature) where the effect of gravity is effectively negligible; the classic example is a supernova remnant.

Figure 2.3 shows the results of a simulation growing a single Rayleigh-Taylor finger on a 2D plane with periodic boundary conditions in the y direction. Figure 2.4 shows the Crab Nebula, an historic supernova remnant that shows the RTI through much of its structure.

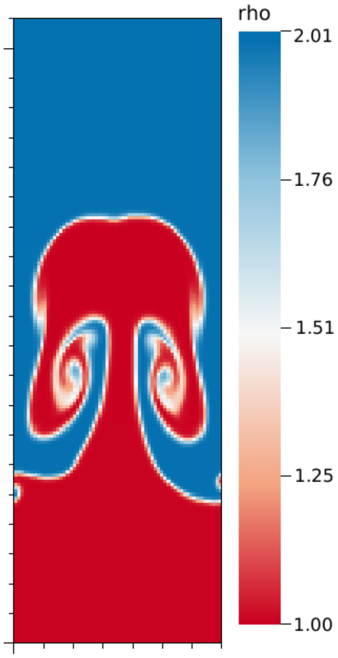

Figure 2.3: Density plot, in g/cm^{-3}, of simulation evolving the Rayleigh-Taylor instability.

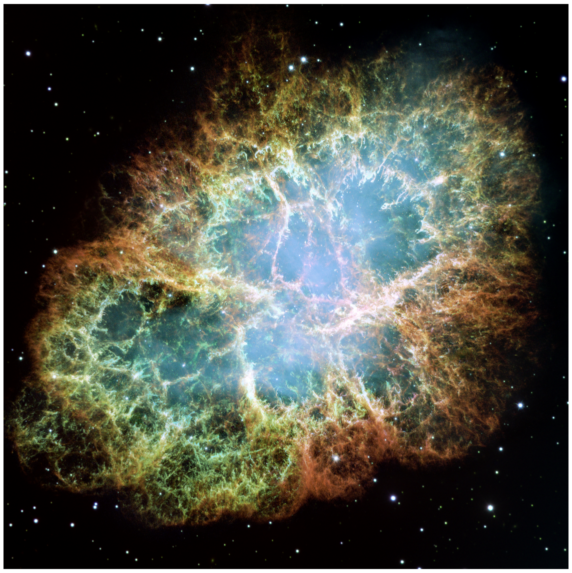

Figure 2.4: Image of the Crab Nebula, image credit: NASA, ESA, J. Hester and A. Loll (Arizona State University)

For small perturbations, linear analysis can show that the position of the interface between the two fluids rises exponentially as

$$y(x,t) = y_0(x)e^{\lambda t}$$

where $\lambda = \sqrt{\mathcal{A}\omega g}$ where $\mathcal{A} = (\rho_2 - \rho_1)/(\rho_2 + \rho_1)$ is the Atwood number (with ρ_2 the more dense of the two), g the gravitational acceleration and α the spatial wave-number. At late times, the assumption of an exponential rise fails and the Kelvin-Helmholtz instability begins to grow along the fingers.

2.3.2 Richtmyer-Meshkov Instability

The Richtmyer-Meshkov instability (RMI) is similar to the RTI, in that there are two fluids of differing densities that are being accelerated, one into the other. However, unlike RTI where the acceleration is a constant between both fluids, the acceleration in this case is due to the interface between two fluids being impulsively accelerated (i.e., a shock passes through the interface).

At late times the structure of the RMI is very similar to the RTI; this is because the instability for RMI evolves quadratically in time whereas the RTI evolves exponentially. Figure 2.5 shows the development of the RMI due to a Mach 3 shock accelerating into the interface of a low-density ($\rho = 0.14$) and high-density ($\rho = 1.4$) fluids.

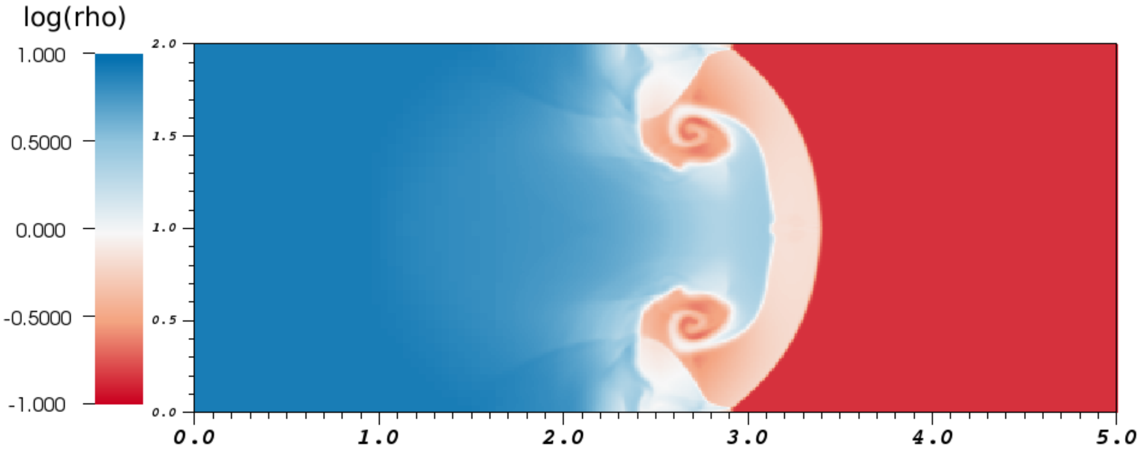

Figure 2.5: The blue region shows the progression of the heavy shock as it enters and accelerates into the lower-density region in red. The white bulge leading the RTI finger is the forward shock, noticeably absent in the RTI simulation.

This type of instability appears to develop at the interface of helium and hydrogen in the outer shell of a core collapse supernova (Kifonidis et al., 2003), and, along with the RTI, appear to be responsible for the chemical mixing in supernova ejecta.

2.3.3 Kelvin-Helmholtz Instability

The Kelvin-Helmholtz instability (KHI) is a type of shearing instability, caused by the interface of two fluids, which need not be of different densities, moving in opposite directions. This instability appears during the late stages of the RMI & RTI. As the fingers extend further into the medium, the stalk of the finger moves in an opposite direction as the ambient.

Figure 2.6 shows a density map of a simulation at $t = 0.83\,\mathrm{s}$ that was perturbed in velocity with a cosine function of amplitude of 0.01. The key signature of the KHI is the curved hooks that appear at the interface of the two fluids. This instability grows linearly in the early phases, before becoming highly turbulent in the non-linear evolution at late times.

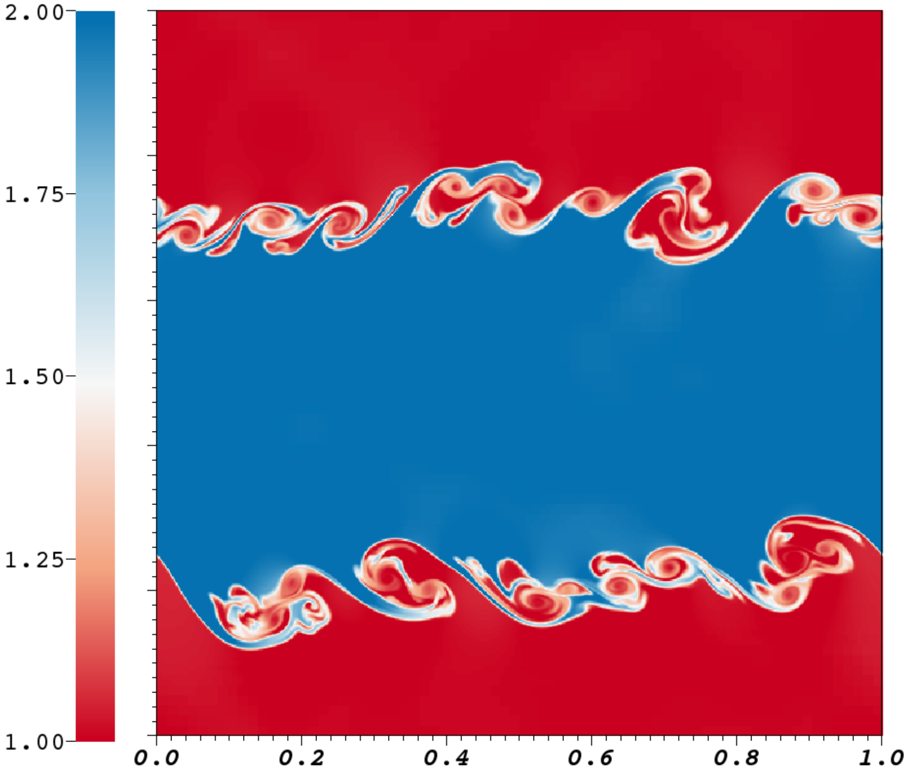

Figure 2.6: Density map of the Kelvin-Helmholtz instability. The red fluid (lower density) is moving towards the right while the blue fluid (higher density) is moving towards the left.

2.4 Magnetohydrodynamics

Plasmas are quasi-neutral, so the effects of the magnetic field generated by the moving charges can play a significant role in the evolution of the dynamics (the field started with Alfvén (1946); a more recent and thorough review can be found in Goedbloed & Poedts (2004)). In this case, Equation 2.7 becomes

$$\frac{\partial \rho}{\partial t} + \nabla \cdot \boldsymbol{\pi} = 0 \tag{2.17a}$$

$$\frac{\partial \boldsymbol{\pi}}{\partial t} + \nabla \cdot (\mathbf{u} : \boldsymbol{\pi} + p_{tot}\mathbf{I} - \mathbf{B} : \mathbf{B}) = 0 \tag{2.17b}$$

$$\frac{\partial E}{\partial t} + \nabla \cdot (\mathbf{u}E + \mathbf{u}p_{tot} + \mathbf{B}\left(\mathbf{B} \cdot \mathbf{u}\right)) = 0 \tag{2.17c}$$

where $p_{tot} = p_{gas} + p_B$ is the total pressure, with $p_B = \mathbf{B} \cdot \mathbf{B}/2$ where we choose to define the magnetic field as $\mathbf{B} = \mathbf{B}_{cgs}/\sqrt{4\pi}$ (i.e., a scaled magnetic field for convenience of notation). It is also necessary to include the dynamic evolution of the magnetic field into the system of equations:

$$\frac{\partial \mathbf{B}}{\partial t} - \nabla \cdot (\mathbf{B} : \mathbf{u} - \mathbf{u} : \mathbf{B}) = 0 \tag{2.17d}$$

with the further constraint that $\nabla \cdot \mathbf{B} = 0$. These are called the magnetohydrodynamic (MHD) equations.

2.4.1 MHD Instabilities

Due to the presence of the magnetic pressure and the divergenceless condition, the magnetic field lines restrict the fluid flows. If a fluid flow is along the z direction, then the total pressure tensor takes the form

$$\begin{array}{cc} \left(\begin{matrix} p + \frac{1}{2}B^2 & 0 & 0 \\ 0 & p + \frac{1}{2}B^2 & 0 \\ 0 & 0 & p - \frac{1}{2}B^2 \end{matrix}\right) & \begin{matrix} \perp \\ \perp \\ \parallel \end{matrix} \end{array} \tag{2.18}$$

where $\perp$ and $\parallel$ designate the direction the pressure is applied with respect to the magnetic field. The perpendicular components serve to compress the field lines while the parallel component serves to straighten the lines.

As an example, adding a magnetic field, $\mathbf{B} = \left(\frac{1}{2},\, 0,\, 0\right)$, to the KHI problem reduces the amplitudes of the instability and increase the timescale before onset. Figure 2.7 shows the KHI developing at $t \simeq 1.5$ seconds, slightly later than Figure 2.6 and noticeably less unstable due to the magnetic field constraining the flows. Similar reductions in the growth of the instabilities occur for the RMI and RTI.

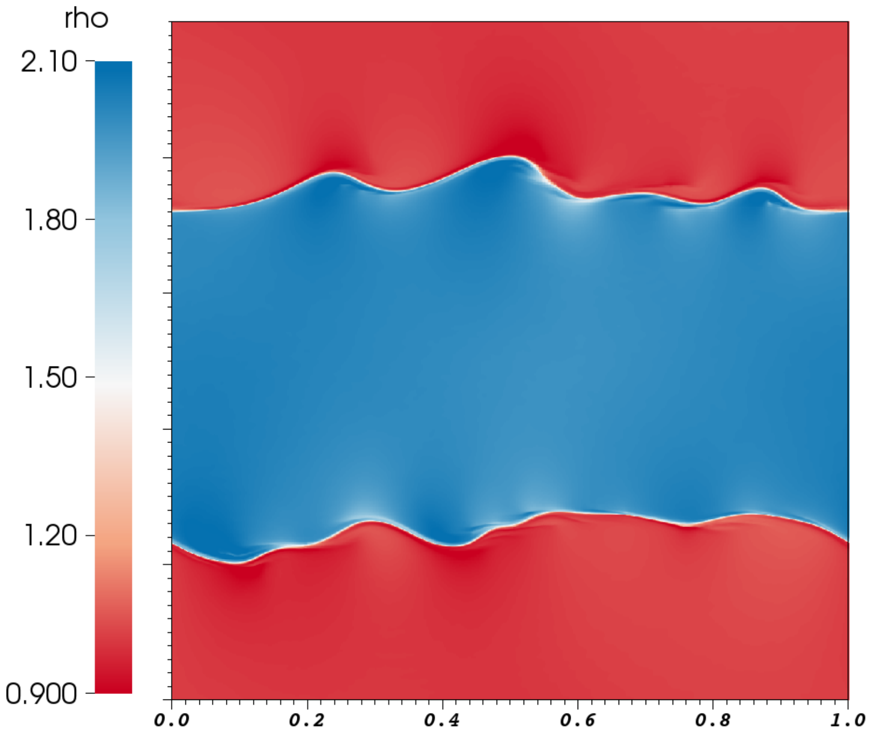

Figure 2.7: Linear density map of the magnetized Kelvin-Helmholtz instability. The magnetic field, initially acting only in the x-direction, inhibits the growth of the perturbations seen in Figure 2.6.

2.5 Cosmic Ray Modified Shocks

The presence of a population of energetic particles in the forward shock, although small in number density compared to the fluid density, introduces a feedback interaction with the dynamical evolution. As the CR particles scatter off the magnetic field in the shock during the DSA process, the energy the particles gain come from the bulk kinetic energy of the flow (Kirk, 1994). Since the flow velocity is part of the DSA equation (Equation 1.13), the extraction of energy by the CRs affects the compression/expansion of the CR fluid, creating a feedback between the shock and the CR particles. The feedback mechanism can be described by a *cosmic ray pressure*, p_{cr}, found from the phase-space distribution discussed in Section 1.2.2, via the integral

$$p_{cr}(\mathbf{x}) = \frac{4\pi mc^2}{3} \int_{\mathrm{p}_{min}}^{\mathrm{p}_{max}} \mathrm{p}^4 f \frac{d\mathrm{p}}{\sqrt{1+\mathrm{p}^2}} \tag{2.19}$$

where $\mathrm{p}_{min} \sim \alpha m c_s$ is the minimum momentum of the particle population (here $\alpha > 1$ constant, m the particle mass and c_s the speed of sound) and p_{max} the maximum cut-off momentum.

The gradient of this pressure adds a new force term to the magnetohydrodynamic equation:

$$\frac{\partial \rho}{\partial t} + \nabla \cdot \boldsymbol{\pi} = 0 \tag{2.20a}$$

$$\frac{\partial \boldsymbol{\pi}}{\partial t} + \nabla \cdot (\rho \mathbf{u} : \boldsymbol{\pi} + p_{tot}\mathbf{I} - \mathbf{B} : \mathbf{B}) = -\nabla p_{cr} \tag{2.20b}$$

$$\frac{\partial E}{\partial t} + \nabla \cdot (\mathbf{u}E + \mathbf{u}p_{tot} + \mathbf{B}\,(\mathbf{B} \cdot \mathbf{u})) = -\mathbf{u} \cdot \nabla p_{cr} \tag{2.20c}$$

$$\frac{\partial \mathbf{B}}{\partial t} + \nabla \cdot (\mathbf{B} : \mathbf{u} - \mathbf{u} : \mathbf{B}) = 0 \tag{2.20d}$$

These are then the *cosmic ray modified magnetohydrodynamic equations.*

With a shock, we can derive the Rankine-Hugoniot jump conditions (see Appendix A), which can show the compression ratio of the density, velocity, and pressures of the two interacting fluids. Under hydrodynamics or parallel-magnetohydrodynamics ($\mathbf{u} \parallel \mathbf{B}$), the compression ratio is

$$\frac{\rho_1}{\rho_2} \equiv \sigma = \frac{(\gamma+1)\,M_2^2}{(\gamma-1)\,M_2^2 + 2} \tag{2.21}$$

where the subscripts indicate the shocked (1) and unshocked (2) regions, $M_2 = u_2/c_{s,2}$ is the downstream Mach number and γ the adiabatic index. For a strong shock, this approximates to $\sigma \simeq (\gamma+1)/(\gamma-1)$ which leads to $\sigma = 4$ for $\gamma = 5/3$ of an ideal gas.

In the presence of efficient cosmic ray acceleration, the particle population can diffuse downstream, generating a precursor "foot" ahead of the shock (Jun & Jones, 1997). The foot grows due to an adiabatic compression such that $p_{gas} \propto \rho^{\gamma}$, leading to a modified structure of the shock. Under CR-modified shocks, there are four states in the flow: (1) the (far) upstream state, (2) the pre-shocked state, (3) the post-shocked state, (4) the (far) downstream state.

Due to the existence of the foot, the Rankine-Hugoniot jump conditions for a hydrodynamic flow must account for this precursor. This leads to the jump relation,

$$\sigma = (\gamma+1)M_1^2 \Big/ \left[\frac{(\gamma+1)M_1^2}{\sigma_0^{\gamma-1}} + 2\right] \sigma_0^{-\gamma} \tag{2.22}$$

where σ_0 is the compression ratio between the upstream and precursor states. In the presence of a strong shock, this above reduces to

$$\sigma \approx \frac{\gamma+1}{\gamma-1}\sigma_0 \tag{2.23}$$

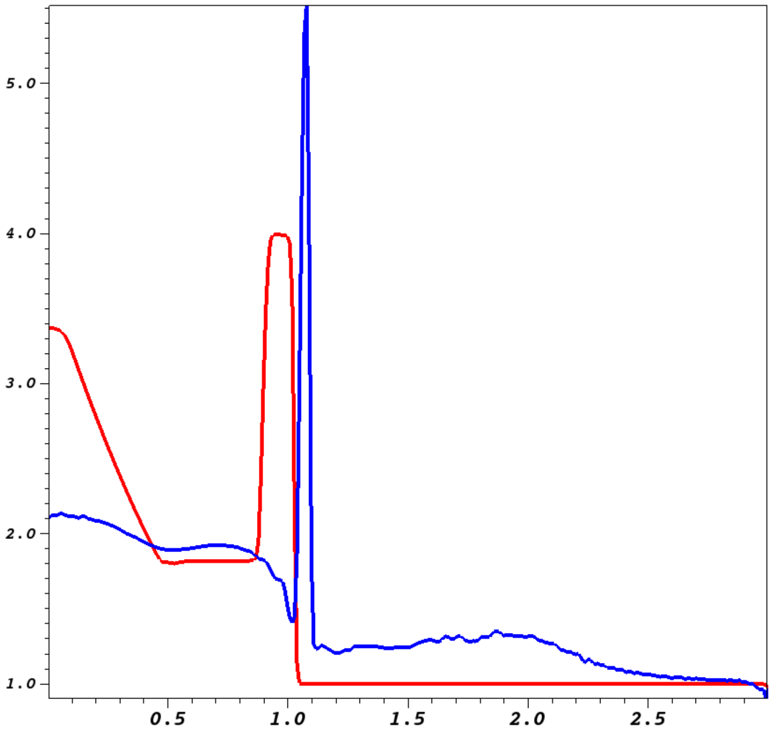

Figure 2.8: One-dimensional solution to the cosmic-ray modified shock. In red is the pure hydrodynamic shock, showing the classic $\sigma = 4$ jump. In blue is the cosmic-ray modified hydrodynamic shock, showing the foot ahead of the shock with a jump of $\sigma = 5.5$.

Figure 2.8 shows a 1D slice in a 2D simulation of the cosmic-ray modified shock alongside a pure hydrodynamic shock with the same initial conditions of a Mach 4 shock interacting with a low-density medium: $\mathbf{U}_l = \left(4, -9.65 \times 10^{-5}, 0.75\right); \mathbf{U}_r = \left(1.0, -3.86 \times 10^{-4}, 6.67 \times 10^{-5}\right)$ where $\mathbf{U} = (\rho,\, u,\, p)$; the cosmic ray pressure was initialized to the same value as the gas pressure. The measured jump is about 5.5, while using the strong-shock approximation gives 5.2, an agreement to $\simeq 5\%$.

2.6 High Energy Emissions

Observations of supernova remnants come in a variety of wavelengths, from radio and optical (Weiler & Sramek, 1988), to X-ray and γ-ray (Reynolds, 2008; Helder et al., 2012; Vink, 2012). Each wavelength can provide different information regarding the state of the plasma. The radio observations can provide information on the magnetic field configuration (Reynoso et al., 2013) while the X-ray plasma can provide details of, among other things, the the temperature of the plasma and ionization stage of a particular element. The types of emissions can be broadly attributed to either a thermal (Maxwellian) population of (charged) particles or a nonthermal (typically power-law) population of particles; each population will be briefly discussed.

2.6.1 Thermal Emissions

For sufficiently large temperatures, the X-ray emissions of SNRs predominately feature spectral lines of metals such as Si, S and Fe, see Figure 2.9. When an electron in an atom makes the transition $E_i \to E_j$ (with $i > j$), the emitted X-ray photon has an energy of the difference $E_X = E_i - E_j$; since each element has a unique set of energy levels, the emitted X-rays are also unique and can be used tracers of the local state. However, at temperatures greater than 10^8 kelvin (10 keV), these features are lost as the dominant process is electron bremsstrahlung (Kaastra et al., 2008; Vink, 2012).

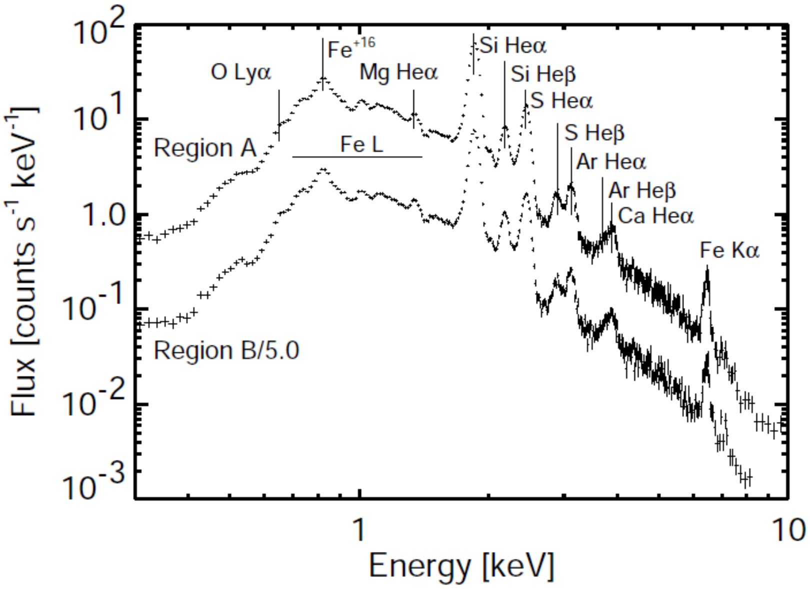

Figure 2.9: X-ray spectrum of Tycho's remnant (SN 1572). Region A and Region B are on the north-eastern and south-eastern side of the remnant, respectively. Image from Badenes et al. (2006).

The line emissions lie on top of continuum emissions, which come from a few different sources, including the bremsstrahlung (also called free-free emission) and recombination (free-bound emission)[5]. For a Maxwellian population of particles, the bremsstrahlung emissivity is given by

$$\varepsilon_{ff} = \eta\, g_{ff}(T_e)\, T_e^{1/2} \exp\left[-\frac{h\nu}{k_B T_e}\right] n_e \sum_i n_i Z_i^2 \,\mathrm{erg/s/cm^3/Hz} \tag{2.24}$$

where $\eta \sim 10^{-27}$ is a constant, $g_{ff}(T_e) \approx 1$ is the gaunt-factor and i denotes the various ion species (Rybicki & Lightman, 1984). For solar compositions, this emissivity is dominated by electron-proton collisions, so often the substitution $n_e \sum n_i Z_i^2 \approx n_e n_H$ is used.

The free-bound emission occurs when an electron is captured into an atomic shell. The energy of the emitted photon is the

$$h\nu_n = E_e + \chi_n \tag{2.25}$$

where n is the quantum number, E_e the energy of the electron and χ_n the ionization potential. Due to the higher statistical weights for the atomic shells, the electron is more likely to be captured into a high-n shell where the energy differences between levels are small. Due to this, the free-bound emission can show sharp edges near the series limits. For a given energy level, the emissivity is given by

$$\varepsilon_{fb} = \xi n_e n_{z+1} \frac{g_i}{g_{i+1}} \sigma(h\nu) \nu \chi_n^2 T^{-3/2} \exp\left[-\frac{E_e}{kT_e}\right] \mathrm{erg/s/cm^3/Hz} \tag{2.26}$$

where $\xi \sim 10^6$ is a constant, g_i are the statistical weights of the ion (before and after recombination) and $\sigma(h\nu) \propto \nu^{-3}$ is the photo-ionization cross-section. The decreasing flux counts at the higher energies (see Figure 2.9) is a feature of the continuum emissions.

2.6.2 Nonthermal Emissions

Radio observations of SNRs showed synchrotron emission (Weiler & Sramek, 1988), due to electrons spiraling around a magnetic field. The fluxes observed could only be explained by a population of electrons obeying a power-law distribution, $N(E) = kE^{-s}$, rather than following a Maxwell-Boltzmann distribution of particles The emissivity due to the nonthermal synchrotron radiation is given by (Reynolds, 2008)

$$\frac{dn_{sy,\gamma}}{dE_\gamma\, dt\, dV} \simeq k 10^{-23} \left(8.31 \times 10^{-8}\right)^{(s-1)/2} B_\perp^{(s+1)/2} E_\gamma^{-(1+s)/2} \frac{\gamma}{\mathrm{erg\,cm^3\,s}} \tag{2.27}$$

---

[5] The Review paper by Kaastra et al. (2008) contains details on all the different types of thermal emissions, we cover these two for brevity.

where $B_\perp$ is the direction of the magnetic field projected onto the plane of the sky. For $s = 2$ expected of cosmic rays, this becomes

$$\frac{dn_{sy,\gamma}}{dE_\gamma\, dt\, dV} \simeq k\, 4 \times 10^{-27} \left(\frac{B_\perp}{E_\gamma}\right)^{3/2} \frac{\gamma}{\mathrm{erg\, cm^3\, s}}$$

The same population of cosmic ray electrons would also be responsible for two other non-thermal emissions: bremsstrahlung and inverse Compton (Gaisser et al., 1998; Schlickeiser, 2002), both of which emit in the γ-ray regime. For the bremsstrahlung emission, the electrons pass near a massive partner (typically assumed a proton), the interaction between the two deflects the electron from its path, causing the emission of a photon. The bremsstrahlung emissivity is,

$$\frac{dn_{br,\gamma}}{dE_\gamma\, dt\, dV} \simeq k\, 7 \times 10^{-16} n_H E_\gamma^{-s} \frac{\gamma}{\mathrm{erg\, cm^3\, s}} \tag{2.28}$$

For inverse Compton, the electrons require an ambient photon field to upscatter. For a single electron of energy $E_e = \gamma m_e c^2$ in an isotropic photon field dn_γ/dV ($\gamma/\mathrm{cm}^3/\mathrm{erg}$), the emissivity of the upscattered photon population is given by (Houck & Allen, 2006; Reynolds, 2008),

$$\frac{dn_{ic,\gamma}}{dE_\gamma\, dt\, dV} \simeq k \int E^{-s} dE \int \sigma_{KN}\left(E_\gamma, \epsilon, \Gamma\right) \frac{dn_\gamma}{dV} d\epsilon \frac{\gamma}{\mathrm{erg\, cm^3\, s}} \tag{2.29}$$

where ϵ is the initial photon energy, E_γ is the photon energy after upscattering, Γ is the Lorentz factor and σ_{KN} is the angle-integrated Klein-Nishina cross-section:

$$\begin{gathered} \sigma_{KN}\left(E_\gamma, \epsilon, \Gamma\right) = \frac{3\sigma_T}{4\epsilon\gamma^2}\left[2q \ln q + (1+2q)(1-q) + \frac{(\Gamma q)^2 (1-q)}{2(1+\Gamma q)}\right] \\ \Gamma = 4\epsilon\gamma/mc^2; \qquad q \equiv \frac{E_\gamma}{\Gamma\left(\gamma m_e c^2 - E_\gamma\right)} \end{gathered} \tag{2.30}$$

with $\sigma_T \sim 6.65 \times 10^{-25}\,\mathrm{cm}^2$ the Thomson cross-section.

Assuming a $B = 1\,\mu\mathrm{G}$ background magnetic field in a medium with $n_H = 0.11\,\mathrm{cm}^{-3}$, a Maxwellian population of ambient photons of temperature $T \approx 2.7\,\mathrm{K}$, and purely leptonic cosmic rays following a distribution of the form,

$$N(E)\, dE \simeq k \left(\frac{E}{E_0}\right)^{-2} \exp\left[\frac{E_0 - E}{E_1}\right] dE \tag{2.31}$$

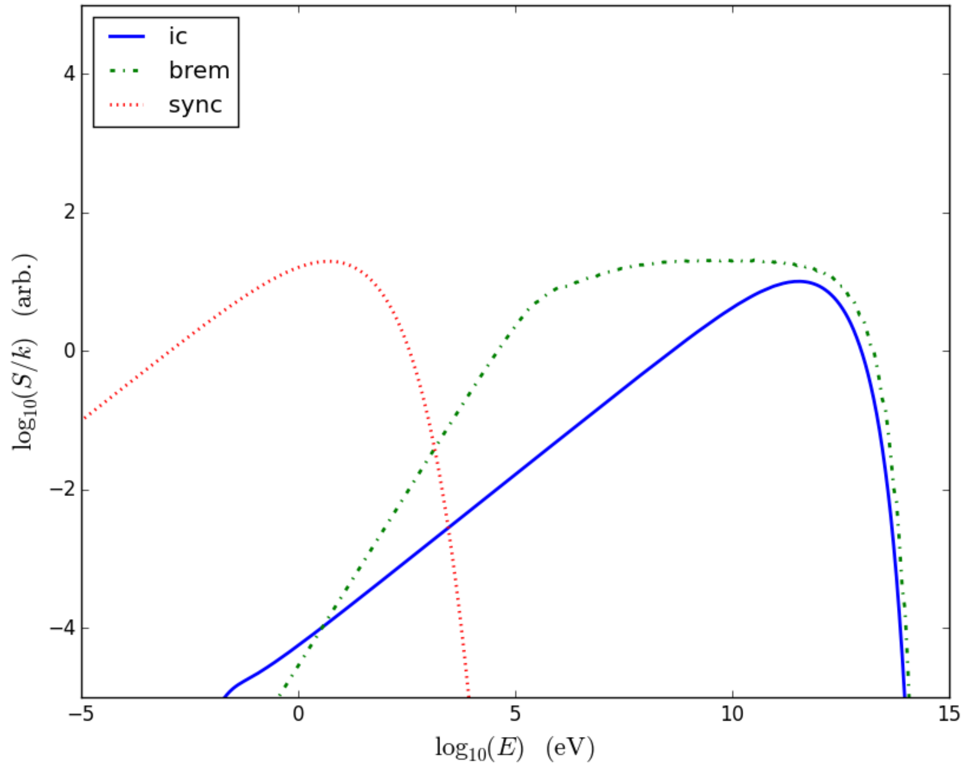

Figure 2.10: Synthetic spectrum of a population of nonthermal electrons in an isotropic medium. S is the source functions, Equations 2.27 through 2.29, divided by the proportionality constant k.

where $E_0 = 10^9$ eV and $E_1 = 10^{13}$ eV limit the distribution, the emissivity of the leptonic emission processes is given above in Figure 2.10. For this particle distribution, the fluxes of the inverse-Compton (blue solid curve) and bremsstrahlung (green dash-dot curve) rise as

$$S_{ic}/k \propto E^{1/2} \tag{2.32}$$

$$S_{br}/k \propto E \tag{2.33}$$

and fall at the high-energy end with the exponential cut-off of the distribution $N(E)$.

As mentioned in Section 1.1.2, the emissions attributed to the accelerated protons is the pion emission. The emissivity of the pion emission is given by (Dermer, 1986; Kelner et al., 2006),

$$\frac{dn_{pp,\gamma}}{dE_\gamma\, dt\, dV} = 8\pi n_H \int_{E_{\pi,min}}^{\infty} \frac{dE_\pi}{(E_\pi^2 - m_\pi^2)^{-1/2}} \int_{E_{p,min}}^{\infty} dE_p N(E_p) \frac{d\sigma(E_p, E_\pi)}{dE_\pi} \tag{2.34}$$

with n_H the ambient density, $E_{\pi,min} = E_\gamma + (m_\pi^2/4E_\gamma)$ the threshold energy for generating the photon from the pion, $E_{p,min} = 2\left(p_{\pi}^2 + m_{\pi}^2\right)^{1/2} + m_{\pi}^2/2m_p \approx 1.2\,\mathrm{GeV}$ the minimum energy required for the relativistic proton to generate a pion, with momentum p_{π}, in the collision with an ambient proton (Stecker, 1971), and $d\sigma/dE_{\pi}$ the cross-section of the $pp \rightarrow \pi^0 +$ anything reaction.

For a power law following $N(E) = kE^{-2}$, the photopion spectrum is symmetric about $E_{\gamma} \approx 70\,\mathrm{MeV}$, leading to the same power-law index for the very large and very small γ-ray energies:

$$\frac{dn_{pp,\gamma}}{dE_{\gamma}\,dt\,dV} \propto \left(\frac{E_{\gamma}}{m_{\pi}}\right)^{\pm s_{\pi}} \tag{2.35}$$

where the positive power is taken for $E_{\gamma} \ll m_{\pi}$ and the negative for the other extreme, $E_{\gamma} \gg m_{\pi}$; in both cases, $s_{\pi} = 4s/3 - 1.04$ is the power-law index of the pion spectrum and s the power-law index of the cosmic ray protons (Schlickeiser, 2002). Thus, the rise of the pion emission for this population of cosmic ray protons follows

$$S_{pp}/k \propto E^{1.63} \tag{2.36}$$

which is significantly steeper than the bremsstrahlung and inverse Compton mechanisms, hence the low-energy regime being the signature of hadronic acceleration[6].

Using Equation 2.31 as the distribution function for CR protons[7] in the same environment as the electrons ($n_H = 0.11\,\mathrm{cm}^{-3}$, etc), the γ-ray emissions due to the decay of neutral pions can be seen in Figure 2.11 below. The sharp kink near $\log(E) \simeq 8$ is due to the approximation of the cross-section (Kamae et al., 2006).

2.6.3 High Energy Observations

For an on-axis photon, the *Fermi-LAT* resolution (Ackermann et al., 2012), as a function of energy, takes the form as seen in Figure 2.12 below. From Figure 2.11, we require observations in the $E_{\gamma} \sim 100\,\mathrm{MeV}$ range to determine the difference between the pion spectrum and the bremsstrahlung/inverse Compton spectrum (via comparing the rise of the flux). In this range, the energy resolution is $\Delta E/E \sim 0.2$ for an on-axis event; this decreases quickly for off-axis events.

However, the larger issue with observing the naked SNRs is not the resolution at these lower

---

[6] Note that for $s \neq 2$, the γ-ray spectrum becomes asymmetric with the larger index having a rapid decline above $E > 1\,\mathrm{GeV}$ and a smaller index having a shallower rise above $E > 1\,\mathrm{GeV}$. For any index, the spectrum is very hard for $E < 300\,\mathrm{MeV}$.

[7] The normalization constant k is different for the electron & proton spectra, requiring an extra multiplicative factor of ~ 90, as shown by Houck & Allen (2006).

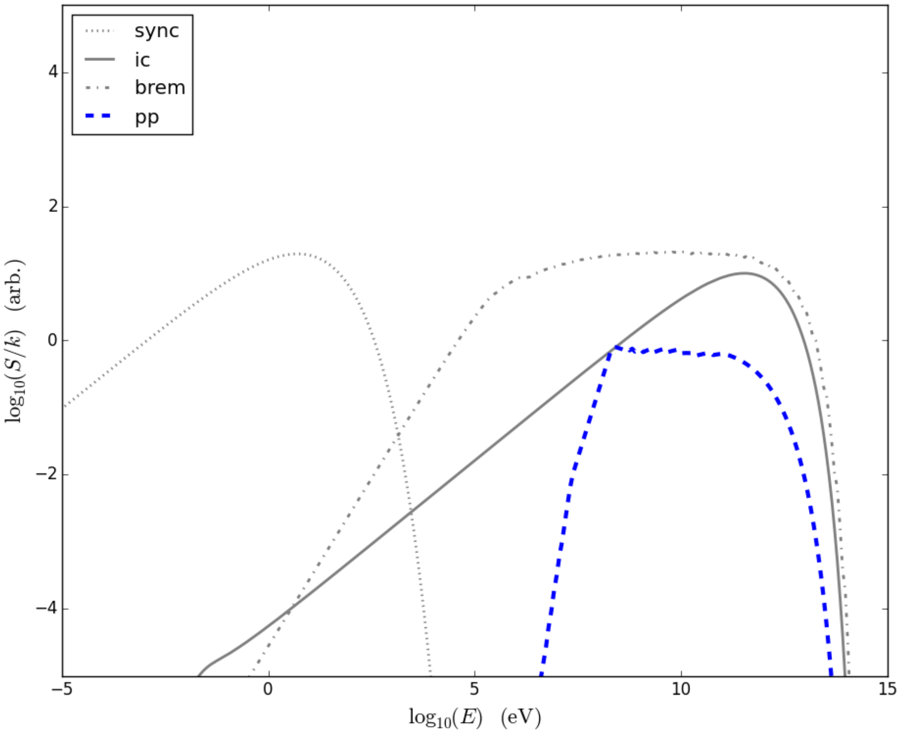

Figure 2.11: The emissivity due to $\pi^0 \rightarrow 2\gamma$ mechanism (blue dashed curve) with the γ-ray spectrum from the leptonic processes in gray (symbols remain the same).

energies, but the differential sensitivity. In Figure 2.13, we see a plot of the differential spectrum for *Fermi-LAT*, assuming a point-source with a power-law spectrum of index 2. At the lower energies, we require a flux greater than a few 10^{-11} erg/cm^2/s in order to observe the γ-ray emissions.

For the SNRs interacting with molecular clouds, the sensitivity of *Fermi-LAT* is sufficient to observe the γ-ray emission (see Section 2.6.3). For example, SNR W44, has been observed with *Fermi* (Abdo et al., 2010; Ackermann et al., 2013; Yoshiike et al., 2013). Due to the interaction of the SNR shock with a nearby molecular cloud, the integrated flux of the remnant is significantly above the needed 10^{-11} level. For this particular remnant, the proton spectrum necessary to generate this spectrum follows a smoothly broken power-law[8],

$$\frac{dN}{dp} \propto p^{-2.36} \left[1 + \left(\frac{p}{p_{br}}\right)^{1.14/\beta}\right]^{-\beta} \tag{2.37}$$

---

[8] The values of the power law indices displayed are the nominal values, Ackermann et al. (2013) gives values with the statistical errors.

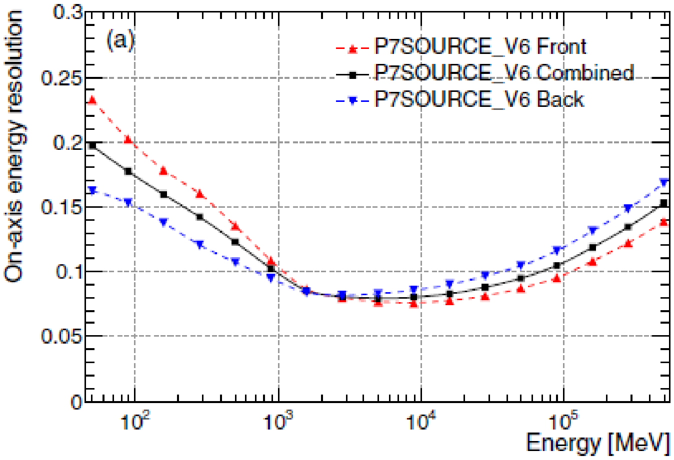

Figure 2.12: Energy resolution as a function of energy for on-axis events, via the updated `pass7` analysis, discussed in Ackermann et al. (2012), that allows for better resolution for $E < 300\,\mathrm{MeV}$.

where $p_{br} = 22 \pm 8\,\mathrm{GeV}/c$ where $\beta \approx 1$[9].

The pion spectrum, given by Equation 2.34, depends linearly on the ambient density, n_H. In the case of W44, the assumption was for $n_H = 100\,\mathrm{cm}^{-3}$. If W44 were a naked remnant, the ambient density would be on the order of $n_H \simeq 0.1\,\mathrm{cm}^{-3}$. This would put the integrated spectrum about 3 orders of magnitude below the differential spectrum thresholds for *Fermi-LAT*. Thus, if we are to be able to observe a naked SNR, either the emissions must very strong or the observational tool be very sensitive.

---

[9] The parameter β is not defined in Ackermann et al. (2013), this value is currently unknown; the author of the paper believes it to be 1 but is not sure, however using the `cosmicp` code suggests $\beta \approx 0.5$ is a better fit.

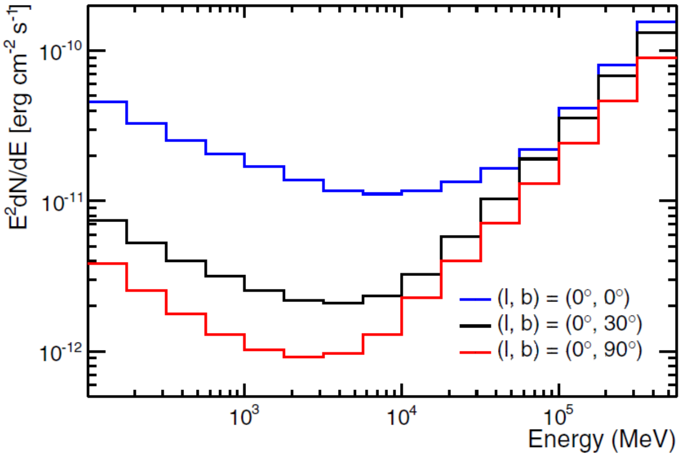

Figure 2.13: Differential sensitivity of the detector as a function of energy for on-axis events, via the updated `pass7` analysis; adapted from Ackermann et al. (2012).

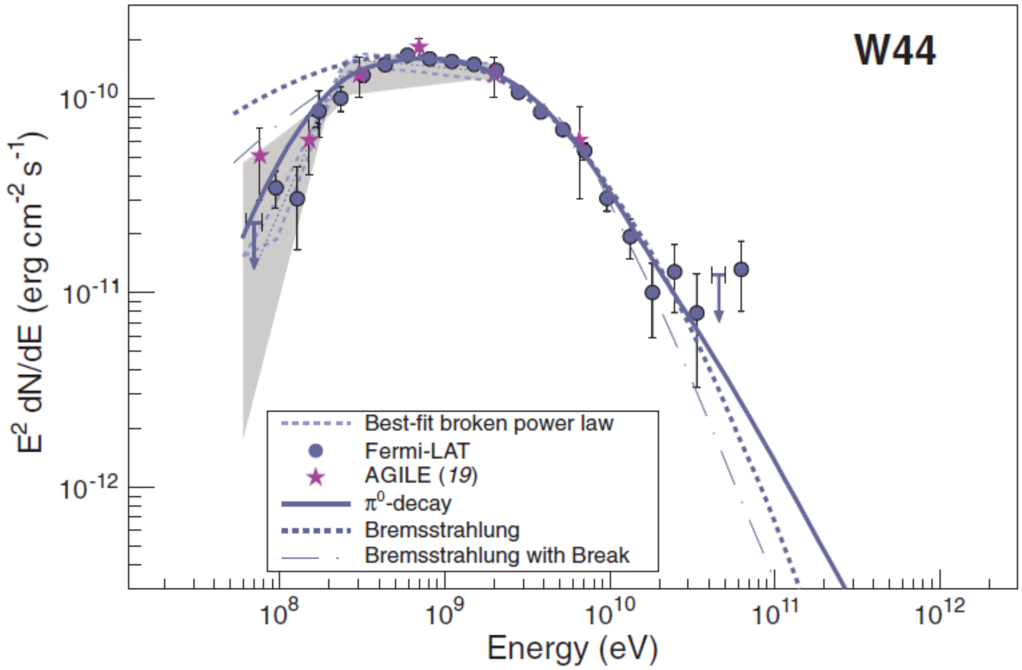

Figure 2.14: γ-ray emission from SNR W44, adapted from Ackermann et al. (2013). The observed flux (filled circles) as measured by *Fermi-LAT* follow the pion decay path (solid line), rather than a bremsstrahlung spectrum (dashed line).

Chapter 3

Numerical Methods

In this Chapter we briefly describe the method of numerical hydrodynamics in Section 3.1, including the numerical model of the SNR profile (Section 3.1.1). Section 3.2 discusses the algorithm for modeling the diffusive shock acceleration (DSA) mechanism for accelerating cosmic ray protons.

3.1 Numerical Hydrodynamics

As described in Section 2.5, the dynamic evolution of a SNR when incorporating the CR feedback can be modeled by the cosmic-ray modified magnetohydrodynamic equations:

$$\frac{\partial \rho}{\partial t} + \nabla \cdot \boldsymbol{\pi} = 0 \tag{3.1a}$$

$$\frac{\partial \boldsymbol{\pi}}{\partial t} + \nabla \cdot (\mathbf{u} : \boldsymbol{\pi} + p_{tot}\mathbf{I} - \mathbf{B} : \mathbf{B}) = -\nabla p_{cr} \tag{3.1b}$$

$$\frac{\partial E}{\partial t} + \nabla \cdot (\mathbf{u}E + \mathbf{u}p_{tot} + \mathbf{B}\,(\mathbf{B} \cdot \mathbf{u})) = -\mathbf{u} \cdot \nabla p_{cr} \tag{3.1c}$$

$$\frac{\partial \mathbf{B}}{\partial t} - \nabla \cdot (\mathbf{B} : \mathbf{u} - \mathbf{u} : \mathbf{B}) = 0 \tag{3.1d}$$

where the variables are the same as those defined earlier. Passive scalars, denoted by ψ_j, that mark interesting regions of the fluid flow follow the Lagrangian advection,

$$D_t \psi = \frac{\partial \psi_j}{\partial t} + \mathbf{u} \cdot \nabla \psi_j = 0 \tag{3.1e}$$

For the CR distribution function, $f(\mathbf{x},\, \mathtt{p},\, t)$, these passive scalars are used to track the dynamic evolution.

The Euler equations are modeled numerically; as computers are discrete counting machines, we must first discretize Equation 3.1. This requires defining a domain of positions and associated averaged values for elements of $\mathbf{U} = (\rho,\, \boldsymbol{\pi},\, E,\, \mathbf{B},\, \psi_j)^T$, see Figure 3.1. The center of each domain is indexed by i, j, k for the x, y, and z directions respectively, while cell interfaces, used for the fluxes, are defined along the mid-point between cells, e.g., $i \pm 1/2$.

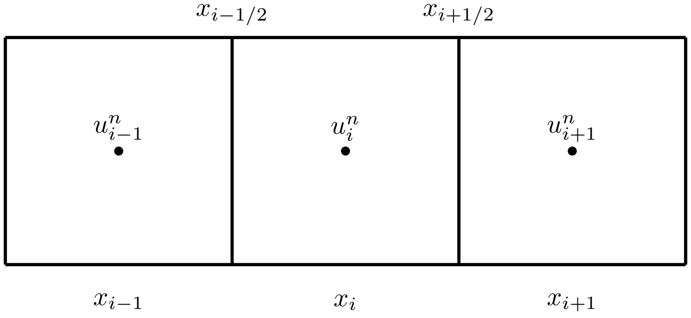

Figure 3.1: Discretized grid in x with $x_i - x_{i-1} = \Delta x$. u^n_i are elements of $\mathbf{U}$ at position x_i and time t_n: $u_i = U\,(x_i,\, t_n)$.

There are many hydrodynamic codes publicly available that can be used, we chose to use AstroBEAR, an acronym for *Astronomical Boundary Embedded Adaptive Refinement.* This code solves the hydrodynamic equations on a Cartesian domain with block-structured adaptive mesh refinement (AMR), which adaptively increases the resolution[1] at interesting regions by adding new domains with a cell-width and time step of

$$\begin{aligned} dx^{\ell+1} &= \frac{1}{2} dx^{\ell} \\ dt^{\ell+1} &= \frac{1}{2} dt^{\ell} \end{aligned} \tag{3.2}$$

such that dt^{ℓ}/dx^{ℓ} is constant for all levels ℓ (Berger & Oliger, 1984; Berger & Colella, 1989).

AstroBEAR is also highly parallelized, scaling well into the ten-thousand processor range. The details of the general method of numerical hydrodynamics, including interpolation schemed, can be found in Cunningham et al. (2009)[2] while Carroll-Nellenback et al. (2013) discusses the AMR engine and parallelization techniques used.

---

[1] As will be discussed in Section 3.2, this aspect of AstroBEAR will not be employed for the cosmic ray simulations.

[2] This discusses v1.0; the current release is v3.0 which has improved many aspects of v1.0.

The source terms required for cooling and cosmic ray production are handled separately from the hydrodynamics solver. The latter will be discussed in the next chapter while the former is discussed next.

3.1.1 Supernova Remnant Profile

An accurate self-similar solution to the interaction of the SNR and ISM material can be found in Chevalier (1982), see Figure 3.2. The density follows a power-law function,

$$\rho(r,t) = \begin{cases} t^{n-3}\left(\frac{r}{g}\right)^{-n} & r < R_c \\ qr^{-s} & r > R_c \end{cases} \tag{3.3}$$

where R_c is the location of the contact discontinuity, where the shocked ejecta and shocked ambient are distinguished. The velocity is assumed to be linear while the pressure is determined in a self-consistent treatment. From physical arguments relating to the accelerations and velocities of the ejecta and ambient gas, it is required that $s < 3$ and $n > 5$.

However, the interaction region of the self-similar profile is extremely small compared to the final size of the remnant, requiring a large number of grids to accurately resolve it.

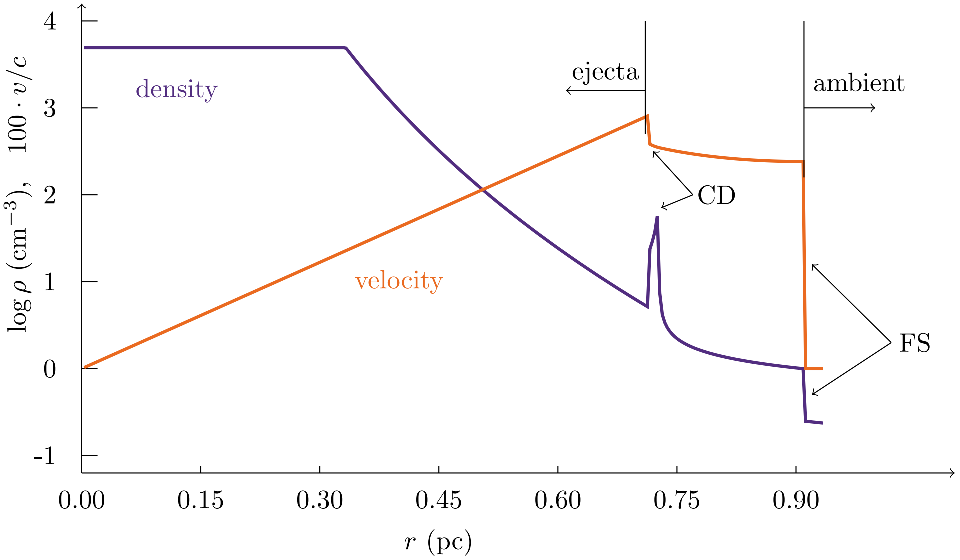

Figure 3.2: Radial density and velocity profiles of a 15 $M_\odot$ Type II SNR with parameters $E_0 = 10^{51}$ erg, $t = 8$ years, $q = 1.0$, $s = 2$, and $n = 9$. The velocity is scaled by 100 so as to be visible alongside the density.

The width of the contact discontinuity is roughly 0.015 pc. In evolving the remnant to $t_{age} \sim 10^3$ years, the radius at the forward shock is approximately 12 pc. In order to resolve the CD, the grid spacing must be less than that, which would require roughly 15,000 grid cells. This is feasible with pure MHD simulations, particularly with the AMR, but, as will be discussed in the next section, the resolution is too great for the diffusive component of the DSA solver.

As an alternative, one can assume that a total ejecta mass, M_{ej}, is uniformly distributed within a small radius, $R_{ej} \leq 1\,\mathrm{pc}$ and inject the total energy, $E_{tot} \sim 10^{51}\,\mathrm{erg}$, into the region as thermal and kinetic components, $E_t = (1-\alpha)E_{tot}$ and $E_k = \alpha E_{tot}$ for $\alpha \in (0,1)$ (Truelove & McKee, 1999; Rodríguez-González et al., 2011; Toledo-Roy et al., 2014). The resulting long-time evolution is similar to that found by the self-similar solution.

3.2 Diffusive Shock Acceleration

3.2.1 Multidimensional DSA

In vector form, the diffusive shock acceleration equation takes the form (O'C Drury, 1983; Kirk, 1994; Malkov & O'C Drury, 2001)

$$\frac{\partial f}{\partial t} + \mathbf{u} \cdot \nabla f = \nabla \cdot \left(D(\mathtt{p})\, \nabla f \right) + \frac{\mathtt{p}}{3} \left(\nabla \cdot \mathbf{u} \right) \frac{\partial f}{\partial \mathtt{p}} + \mathcal{Q} \tag{3.4}$$

with all variables as defined in Section 1.2. In order to numerically solve this equation with the necessary resolution, one would need to have $\Delta \ln \mathtt{p} < 0.1$. Solving Equation 3.4 in one dimension with such resolution can be done, but the code would spend much of its run-time updating the distribution $f(x, \mathtt{p}, t)$ due to the stability restriction, $\Delta t \propto \Delta x^2$ for the diffusion term, as compared to the advection time-step restriction of $\Delta t \propto \Delta x$. Using this method for long-term studies in multiple dimensions is not feasible, even with efficient parallelization to 10,000 processing cores.

For that reason, we employ the *coarse-grained momentum volume* (CGMV) method (Jones & Kang, 2005; Edmon, 2010). This method uses the fact that the well-studied distribution $f(\mathtt{p})$ has a piece-wise power-law form in momentum space: $f \propto \mathtt{p}^{-q(\mathtt{p})}$, where $q(\mathtt{p}) = -d \ln f / d \ln \mathtt{p} \approx 4$. In this method, Equation 3.4 is recast into two equations, one each for the following moments of

$f(x, \mathtt{p})$:

$$n_{i,\ell} = \int_{\mathtt{p}_\ell}^{\mathtt{p}_{\ell+1}} \mathtt{p}^2 f_i\left(\mathtt{p}\right)\, d\mathtt{p} \tag{3.5a}$$

which is related to the spatial number density of accelerated particles in the range $\Delta\mathtt{p}_\ell = [\mathtt{p}_\ell,\, \mathtt{p}_{\ell+1}]$ and

$$g_{i,\ell} = \int_{\mathtt{p}_\ell}^{\mathtt{p}_{\ell+1}} \mathtt{p}^3 f_i\left(\mathtt{p}\right)\, d\mathtt{p} \tag{3.5b}$$

which is related to the total energy density of the particles in the momentum bin. In both cases, i and ℓ represent the spatial and momentum index, respectively. The combination of $n_{i,\ell}$ and $g_{i,\ell}$ can be used to determine the full distribution, $f_{i,\ell}$, and particle pressure, p_{CR}, via simple iteration.

A direct substitution of Equation 3.5a into Equation 3.4 results, in one dimension, in

$$\frac{\partial n_\ell}{\partial t} + u\frac{\partial n_\ell}{\partial x} = F_{n_\ell} - F_{n_{\ell+1}} - n_\ell\frac{\partial u}{\partial x} + \frac{\partial}{\partial x}\left(D_{n_\ell}\frac{\partial n_\ell}{\partial x}\right) + \mathcal{Q}_{n_\ell} \tag{3.6}$$

where F_{n_ℓ} is the momentum-space flux between adjacent cells:

$$F_{n_\ell} = \left[\frac{q(\mathtt{p}_\ell)D_{n_\ell}}{\mathtt{p}_\ell} - \frac{1}{3}\mathtt{p}_\ell\frac{\partial u}{\partial x}\right]\mathtt{p}_\ell^2 f(\mathtt{p}_\ell). \tag{3.7}$$

We also define D_{n_ℓ} and $\mathcal{Q}(n_\ell)$ as the moment-integrated diffusion coefficient and source term, respectively:

$$D_{n_\ell} = \frac{1}{n_\ell}\int_{\mathtt{p}_\ell}^{\mathtt{p}_{\ell+1}} D(\mathtt{p})\mathtt{p}^2 f(\mathtt{p})\, d\mathtt{p} \tag{3.8}$$

$$\mathcal{Q}_{n_\ell} = \int_{\mathtt{p}_\ell}^{\mathtt{p}_{\ell+1}} \mathtt{p}^2 S\left(\mathtt{p}\right)\, d\mathtt{p} \tag{3.9}$$

A similar set of equations can be derived for g_ℓ.

There are two advantages of using n_ℓ and g_ℓ. The first is that, due to the taking of the moments, the required number of cells is an order of magnitude less, $\mathcal{O}(10)$ for each n and g compared to $\mathcal{O}(100)$ for f alone. This alone allows for a faster total solution of the diffusion component, as there are significantly less number of cells. The other advantage is that time-step is not limited by

$\Delta t \propto \Delta x^2$ as is the case of the finite-difference method. Here, the limiting time-step is

$$\Delta t \sim 2 \left(\frac{\Delta x}{u_s} \right) \Delta \ln \mathtt{p}. \tag{3.10}$$

The investigation of Jones & Kang (2005) show that when $\Delta \ln \mathtt{p} > 2.3$, the cosmic ray pressure induces an over-pressure in the region of the shock and that for $1 \lesssim \Delta \ln \mathtt{p} \lesssim 1.5$, the resulting spectrum is approximately equal to the $\Delta \ln \mathtt{p} < 0.1$ case of the finite-difference method.

The particle acceleration solver utilizes the operator splitting technique (Yanenko, 1971; Marchuk, 1990; Khan & Liu, 1998) along one-dimensional slices of the two-dimensional domain. This requires Equation 3.6 to be split up as

$$\frac{dn_\ell}{dt} = -u \frac{\partial n_\ell}{\partial x} \tag{3.11a}$$

$$\frac{dn_\ell}{dt} = F_{n_\ell} - F_{n_{\ell+1}} - n_\ell \frac{\partial u}{\partial x} + \frac{\partial}{\partial x} \left(D_{n_\ell} \frac{\partial n_\ell}{\partial x} \right) + \mathcal{Q}_{n_\ell} \tag{3.11b}$$

The first step of the splitting, Equation 3.11a is the advection of the particle population, this is taken care of by Equation 3.1e in AstroBEAR. The second step is handled by the particle acceleration subroutine added to AstroBEAR.

3.2.2 Cosmic Ray Injection

The addition of new particles into the acceleration mechanism is called injection. There are two methods commonly used to describe the injection (Caprioli et al., 2010b; Jones & Kang, 2005). The first is called the *flux-fraction* model in which a small, fixed fraction of the thermal particle flux through the shock, η_{inj}, is injected at momentum $\mathtt{p}_{inj} \sim mc_s$ where c_s is the speed of sound in the fluid in the region downstream of the shock. In this case, the source term takes the form

$$S\left(\mathtt{p},\, \mathbf{x},\, t\right) = \eta_{inj} \frac{\rho_1 u_s}{4\pi m \mathtt{p}_{inj}^2} \delta\left(\mathtt{p} - \mathtt{p}_{inj}\right) w\left(\mathbf{x} - \mathbf{x}_s\right) \tag{3.12}$$

where ρ_1 the upstream mass density, u_s the shock velocity relative to the upstream velocity, $\mathbf{x}_s$ the shock location and $w(a) \sim \exp\left(-a^2\right)$ is a (normalized) weighting function that smooths the injection over the shock region.

The other injection method is called the *thermal leakage* model in which particles with momenta in the tail of the Maxwellian distribution can leak upstream across the shock (the particle velocities must be large enough to be able to move across the plasma without being scattered by the MHD waves). In this model, a leakage function is approximated by (Kang et al., 2002)

$$\tau_{inj}\left(\epsilon,\, \frac{v}{u_d}\right) = H\left[\tilde{v} - (1+\epsilon)\right]\left(1 - \frac{u_d}{v}\right)^{-1}\left(1 - \frac{1}{\tilde{v}}\right)\exp\left[-\left(\tilde{v} - (1+\epsilon)\right)^{-2}\right] \tag{3.13}$$

where v is the particle velocity, $\epsilon = B_0/B_\perp \sim 0.25$ is the measure of the magnetic turbulence, $u_d = u_s/r$ is the ratio of the shock velocity (u_s) and compression ratio (r), $\tilde{v} = \epsilon v/u_d$ is the normalized particle velocity, and $H[x]$ the Heaviside step function.

It has been shown elsewhere that both models produce the same particle spectrum (Jones & Kang, 2005; Caprioli et al., 2010b); due to its simplicity, we adopt the fixed fraction method for injecting particles.

3.2.3 Cosmic Ray Diffusion

The momentum flux values computed in the CGMV algorithm and the injection are combined into a single source value,

$$S = \Delta F_{n_\ell} - n_\ell \frac{\partial u}{\partial x} + \mathcal{Q}(n_\ell) \tag{3.14}$$

These are then added to the distribution while solving the diffusion of the population, making the diffusion component of the algorithm effectively a diffusion equation with a source term. This takes the form (cf. Equation 3.11b),

$$\frac{\partial f}{\partial t} = \frac{\partial^2 f}{\partial x^2} + S \tag{3.15}$$

This is solved in a semi-implicit method, meaning that the left- and right-hand sides depend on both the n and the $n+1$ states (Crank & Nicolson, 1947), resulting in

$$\frac{f^{n+1} - f^n}{\Delta t} = \frac{1}{2}\left[\mathcal{F}\left(f^{n+1}\right) + \mathcal{F}\left(f^n\right)\right] + S_i \tag{3.16}$$

where $\mathcal{F}$ is the numerical flux operator. This can be then molded into the operator formalism,

$$A_+ f_{i+1}^{n+1} + A_0 f_i^{n+1} + A_- f_{i-1}^{n+1} = H\left(f^n,\, S\right) \tag{3.17}$$

where $H\left(f^n,\, S\right)$ contains all the f^n values and the source term, and $A_{\pm} = -\Delta t/2\Delta x^2$. As i ranges in values from 1 to I, this is a matrix equation:

$$\begin{pmatrix} A_0 & A_+ & 0 & \cdots & 0 \\ A_- & A_0 & A_+ & \cdots & 0 \\ 0 & \ddots & A_0 & \ddots & \vdots \\ \vdots & 0 & A_- & A_0 & A_+ \\ 0 & \cdots & 0 & A_- & A_0 \end{pmatrix} \begin{pmatrix} f_1 \\ f_2 \\ f_3 \\ \vdots \\ f_I \end{pmatrix} = \begin{pmatrix} H_1 \\ H_2 \\ H_3 \\ \vdots \\ H_I \end{pmatrix} \tag{3.18}$$

And since the elements of the matrix are along the main diagonal and the adjacent diagonals above (below) the main diagonal, this particular matrix is called a *tridiagonal* matrix. Due to its symmetry, this has an analytic solution that can be computed in $\mathcal{O}\left(I\right)$ time as compared to a Gaussian elimination scheme that requires $\mathcal{O}\left(I^3\right)$ time.

3.2.4 Numerical Issues

Implicit and semi-implicit methods are sensitive to boundary conditions due to the discretization error of the method. Poorly defined boundary conditions can introduce oscillatory data into the domain that can reduce the accuracy from second-order to first-order in space, see Figure 3.3. This is also true for parallelized simulations, when passing information from one processor to another[3]. In the case of the particle distributions, $n(x, \mathtt{p})$ and $g(x, \mathtt{p})$, the oscillatory behavior generally arises due to the diffusion of the particle population off the domain (i.e., the particles are advected out of the grid on processor 1 and onto the grid of processor 2).

In order to remedy this, Edmon (2010) developed an algorithm called *Multidimensional Adaptive Sub-cycling Tridiagonal* (MAST) that eliminates the oscillations by first allowing the ghost cells between the furthest cell (the left-most point in Figure 3.3) and the computational domain (the solid line) to be free-floating, such that the sub-cycles of the diffusion solver can smoothly transition to the ideal, smooth solution. When solutions vary too much, the tridiagonal solver is restarted with a larger number of iterations and smaller dx until either the oscillations are no longer present or the maximum number of sub-cycling iterations, $n_{iter}^{max} \sim D_{max}\, dt/dx^2$, is reached, at which point the solution prints a warning and takes the average of the three cells $(i-1,\, i,\, i+1)$.

---

[3] In this case, the boundary is not a physical boundary of the simulation, but a computational one (an interior boundary).

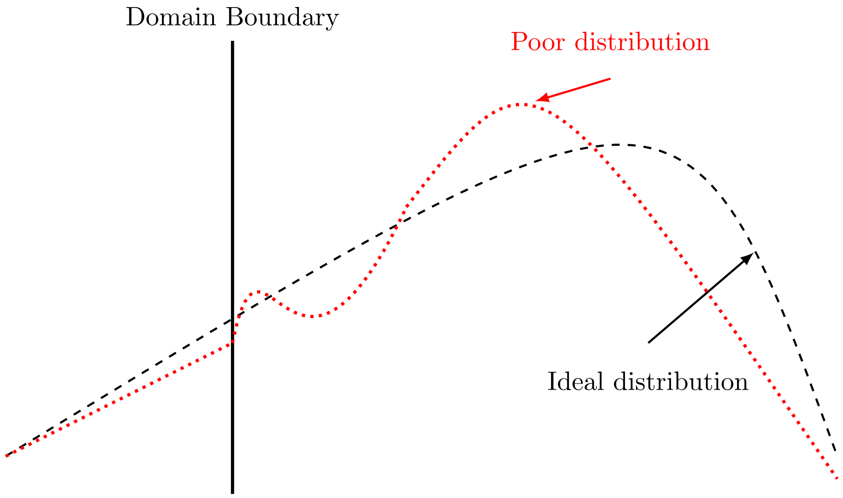

Figure 3.3: Example of oscillatory behavior due to boundary conditions. The red curve is an example of the result of non-smooth boundaries between adjacent domains.

Testing has also shown that the system can be over-resolved, leading to the production of a vacuum in the distributions ($n, g \leq 0$). When the resolution is too great, the particles can diffuse out of the cell, possibly cross several cell boundaries. Aside from the negative CR densities, the vacuum solutions also lead to an unphysical negative pressure associated with the CRs. The underlying issue is that the diffusion length of the interior boundaries is limited by the computational domain,

$$l_d = k_{max} \frac{\Delta t}{\Delta x} \tag{3.19}$$

By increasing resolution (decreasing Δx), the diffusion length also increases proportionately. As the interior boundaries are set by AstroBEAR at execution, the increase in resolution must be matched by a decrease in the number of processors, leading to a nonlinear increase in execution time.

3.2.5 Synthetic Pion Spectrum

We utilize an updated version of the cosmicp code[4] to create the synthetic emission map for the photopions and, by assuming that the distribution for leptons follows the same power-law distribution as the electrons (scaled appropriately), we also generate a synthetic spectra of the leptonic emissions for comparison. Given an input spectrum, $N(E)$, over a set range of energies, a background photon field, and the local ambient densities, the cosmicp code can return the expected

---

[4] Private communication, see Edmon et al (2011) for details of cosmicp

nonthermal γ-ray emissions via Equations 2.27, 2.28, 2.29 and 2.34, following the parametrizations of Kelner et al. (2006) and Kamae et al. (2006). Figures 2.10 and 2.11 were generated using this code.

3.3 Simulation Parameters

For the DSA simulations, we deposit $M_\star = 4\,M_\odot$ into a small volume, $R_\star = 1.0\,\mathrm{pc}$, with an initial energy, $E_i = 10^{51}\,\mathrm{erg}$, that is split between thermal ($E_t = (1-\alpha)E_i$) and kinetic ($E_k = \alpha E_i$) energies at a 40:60 ratio (i.e., $\alpha = 0.6$). The maximum velocity at $R_\star$ is then computed via (Truelove & McKee, 1999),

$$v_{max}(R_\star) = \sqrt{\frac{10}{3}\frac{E_k}{M_\star}} \tag{3.20}$$

and the internal pressure,

$$p_{gas} = \begin{cases} (\gamma - 1)\,E_t/V & r \leq R_\star \\ \delta\rho_{amb}T & r > R_\star \end{cases} \tag{3.21}$$

where $V = 4\pi R_\star^3/3$ is the volume of the SNR, δ contains the appropriate scaling factors and $T = 10^3\,\mathrm{K}$ is the temperature of the ambient region. These conditions are the same for the comparison test-cases as well: one in which the adiabatic index takes the standard value of 5/3 and one in which it is 1.1, representing the effects of the presence of CRs (Blondin & Ellison, 2001; Schure et al., 2009b). The magnetic field is uniform with magnitude $|\mathbf{B}| = 10^{-6}\,\mu\mathrm{G}$ and pointing in the NW direction; the B_z component is required to be zero for numerical MHD in two dimensions.

The physical grid is $[-20\,,\,20]$ pc along each side of the two dimensional, Cartesian domain and the simulation runs from $t = 0$ to $t = 1500\,\mathrm{yrs}$. Due to the constraints put forth in Section 3.2.4, we restrict the MHD+CR simulation to a resolution of 1500^2 cells ($dx \approx 8.2 \times 10^{16}\,\mathrm{cm}$); the comparison cases contain one level of AMR ($dx_{eff} \approx 4.1 \times 10^{16}\,\mathrm{cm}$).

As the cosmic ray energy density is $w_{cr} \approx 1\,\mathrm{eV/cm^{-3}}$ (see Section 1.1.1), we initialize a uniform background pressure due to cosmic rays equal to this value, spread across the whole grid. Using Equation 2.19 and the expectation that $f(\mathtt{p}) \propto \mathtt{p}^{-4}$, we can generate the moments n and g from this background pressure. Though there is this background particle population, it does not contribute to the injection of fresh particles in the injection algorithm described in Section 3.2.2, as the density, ρ_1, is the upstream mass density of the plasma and does not account for the existing CR particles. However, the dynamic evolution of the remnant will affect the injection of fresh particles as the values of ρ_1, u_s and $\mathtt{p}_{inj}$ will vary across different shocks in the remnant.

The diffusion coefficient chosen satisfies the conditions presented by Malkov & O'C Drury (2001) (see also Section 1.2.3), taking the form

$$D(\mathbf{x}, \mathtt{p}) = D_0 \left(\frac{B_0}{B(\mathbf{x})} \right) \mathtt{p}^{0.51} \tag{3.22}$$

where $D_0 = 3 \times 10^{24}\,\mathrm{cm}^2/\mathrm{s}$ and $B(\mathbf{x})$ the magnitude of the magnetic field and $B_0 = 10^{-6}\,\mu\mathrm{G}$. The choice of D_0 stems from the assumption of a Bohmian diffusion; the value arising as the maximum after the remnant is evolved for 1500 years.

In addition to this form of the diffusion coefficient, we allow for cross-field diffusion by multiplying the result of Equation 3.8 with the a parameter that accounts for the direction of the magnetic field,

$$D_{n_\ell} \rightarrow D_{n_\ell} \left(\frac{B_n}{|\mathbf{B}|} + \kappa \, \frac{1 - B_n}{|\mathbf{B}|} \right) \tag{3.23}$$

where B_n is the magnetic field in the direction of the solver, $|\mathbf{B}|$ the magnitude of the magnetic field in the computational cell and κ a constant that represents the fraction of the tangential magnetic field leaked into the normal direction; we take $\kappa = 0.16$, consistent with the requirement that $0.1 \leq \kappa \leq 0.2$ (Scalo & Elmegreen, 2004).

Chapter 4

Results

In this chapter, we present the analysis of the simulations. Section 4.1 compares the results of the SNR evolution between the differing models, focusing the the dynamical effects of the cosmic ray feedback. We then discuss the production of cosmic rays in Section 4.2, followed by the discussion on the synthetic spectra of the SNRs in Section 4.3.

4.1 SNR Evolution Models

The production and presence of the cosmic rays feeding back into the hydrodynamics is known to cause a difference in the shock structure (see Section 2.5). In the evolution of the SNR models tested, the effects on the modified equation of state (i.e., $\gamma = 1.1$ versus $\gamma = 5/3$) also introduces a change in the shock structure. In this latter case, the Rankine-Hugoniot jump conditions should lead to a steeper jump between the upstream and downstream regions for the strong, planar shock,

$$\sigma_{\gamma=1.1} = 21 \tag{4.1}$$

as compared to the $\sigma_{\gamma=5/3} = 4$ case. In the case of the SNR, the remnant shocks the ambient gas, causing a change in the shock structure (though this is not observed in the $\gamma = 1.1$ case, see Figure 4.1). The measured jumps of the forward shock (between the shocked and unshocked ambient gas) and the reverse shock (between the shocked and unshocked ejecta) are

$$\sigma = \begin{cases} 17, & — \quad \gamma = 1.1 \\ 3.6, & 2.3 \quad \gamma = 5/3 \\ 3.1, & 4.0 \quad \mathrm{MHD} + \mathrm{CR} \end{cases} \tag{4.2}$$

where the null value for $\gamma = 1.1$ is due to the lack of the shocked ambient gas. The net jump (unshocked ambient to unshocked ejecta) for the latter two models is 8.5 and 12.0, respectively.

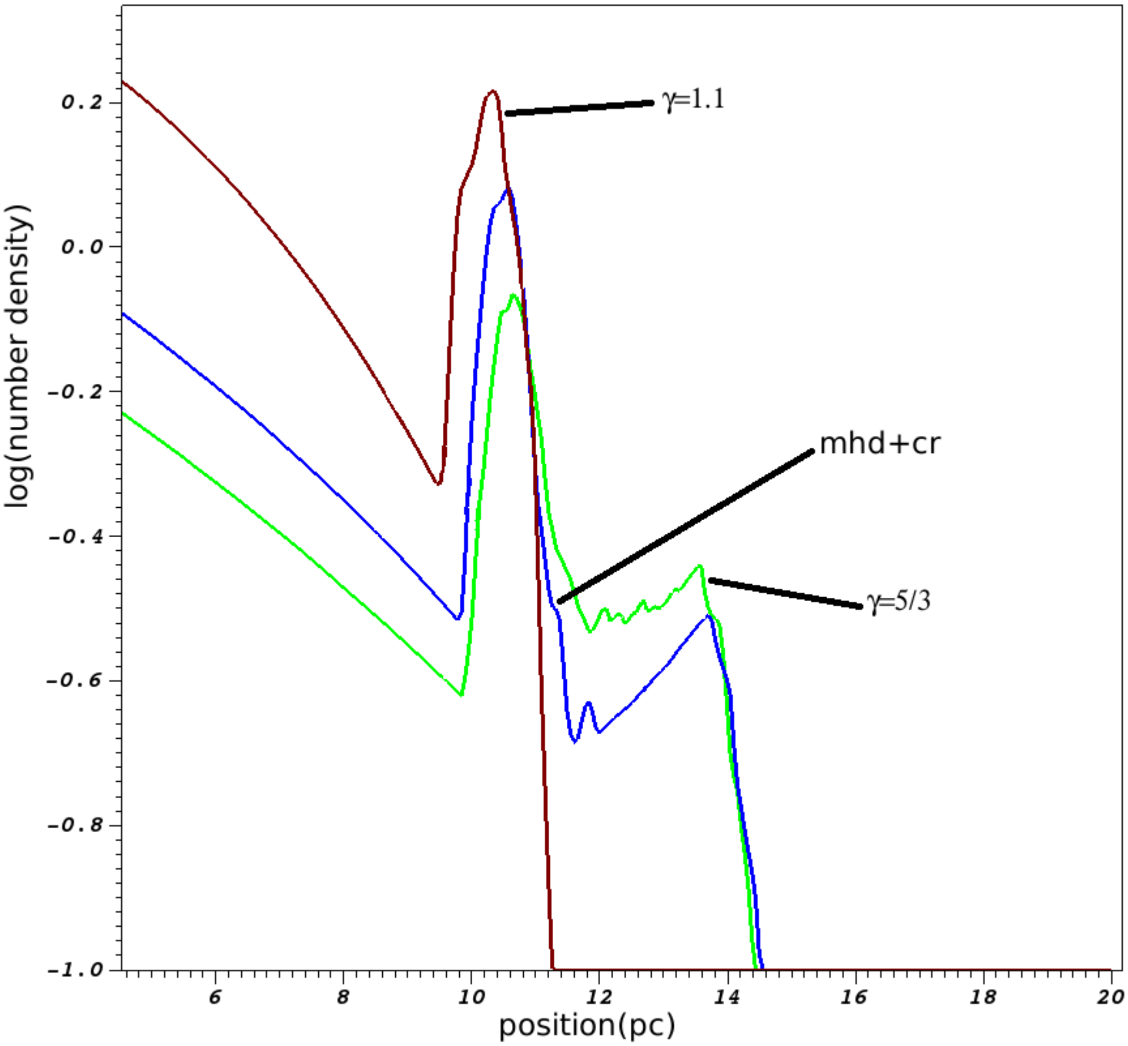

Figure 4.1: Azimuthally-averaged logarithmic density profiles for the three models (labeled).

The width of the interaction region between the ambient and the ejecta is inversely related to the compression ratio, σ. For the $\gamma = 1.1$ model, the region is $\sim 1\,\mathrm{pc}$, whereas the MHD+CR and $\gamma = 5/3$ model have an interaction region that is several parsecs wide, due to the shocked ambient gas. This thinner region allows for the Rayleigh-Taylor fingers of the $\gamma = 1.1$ model to penetrate the forward shock (see Figure 4.2), while the fingers in the $\gamma = 5/3$ and MHD+CR models are still far from forward shock.

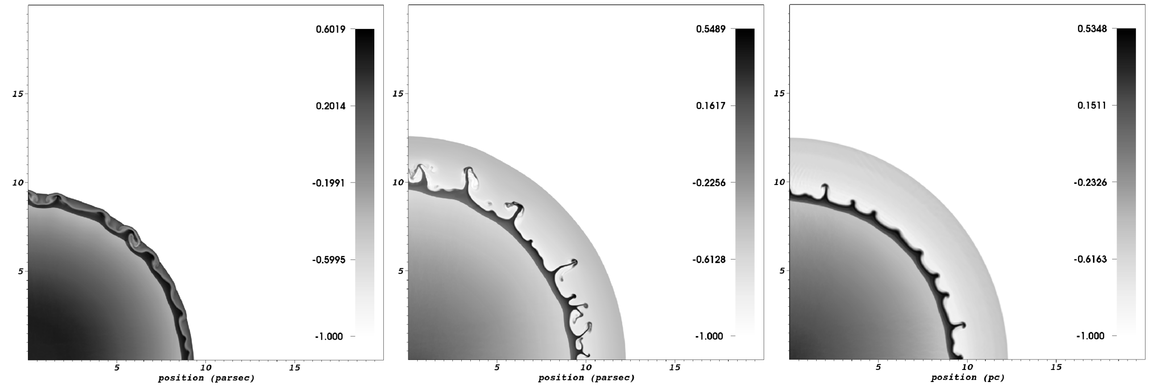

Figure 4.2: Logarithmic density plot of the three models, $\gamma = 1.1$, $\gamma = 5/3$ and MHD+CR respectively. Each image is from the same $t \simeq 1.3\,\mathrm{kyr}$ with $n_{low} = -1.0$

The growth of the RTI is also incredibly damped in the MHD+CR model. The studies by Ferrand et al. (2010) and Fraschetti et al. (2010), in which the CR were modeled by a spatially-dependent adiabatic index, $\gamma(\mathbf{x})$, show no such damping of the RTI. Fraschetti et al. (2010) suggest that if the density behind the reverse shock is lower as compared to the density behind the forward shock, it might “hinder the development of the RT fingers.” We find the opposite to be true: when the density is relatively higher behind the reverse shock, the development of the RT fingers is hindered[1] (compare the blue and green curves in Figure 4.1).

A more detailed comparison of these two figures can be seen in Figure 4.3. Here, in order to emphasize the difference in the RT fingers, we plot the square of the number density and fix the scales to be in the range 0.001 and 12; doing so, however, also obscures the location of the forward shock from view. The longest of RT fingers in the MHD+CR model are roughly the same size as those found in the $\gamma = 5/3$ model, however the majority of the RT fingers in the MHD+CR model are less than half that.

---

[1] Other test cases, which failed due to the numerical issues mentioned in Section 3.2.4, showed similar structure as the model presented here, prior to their failing.

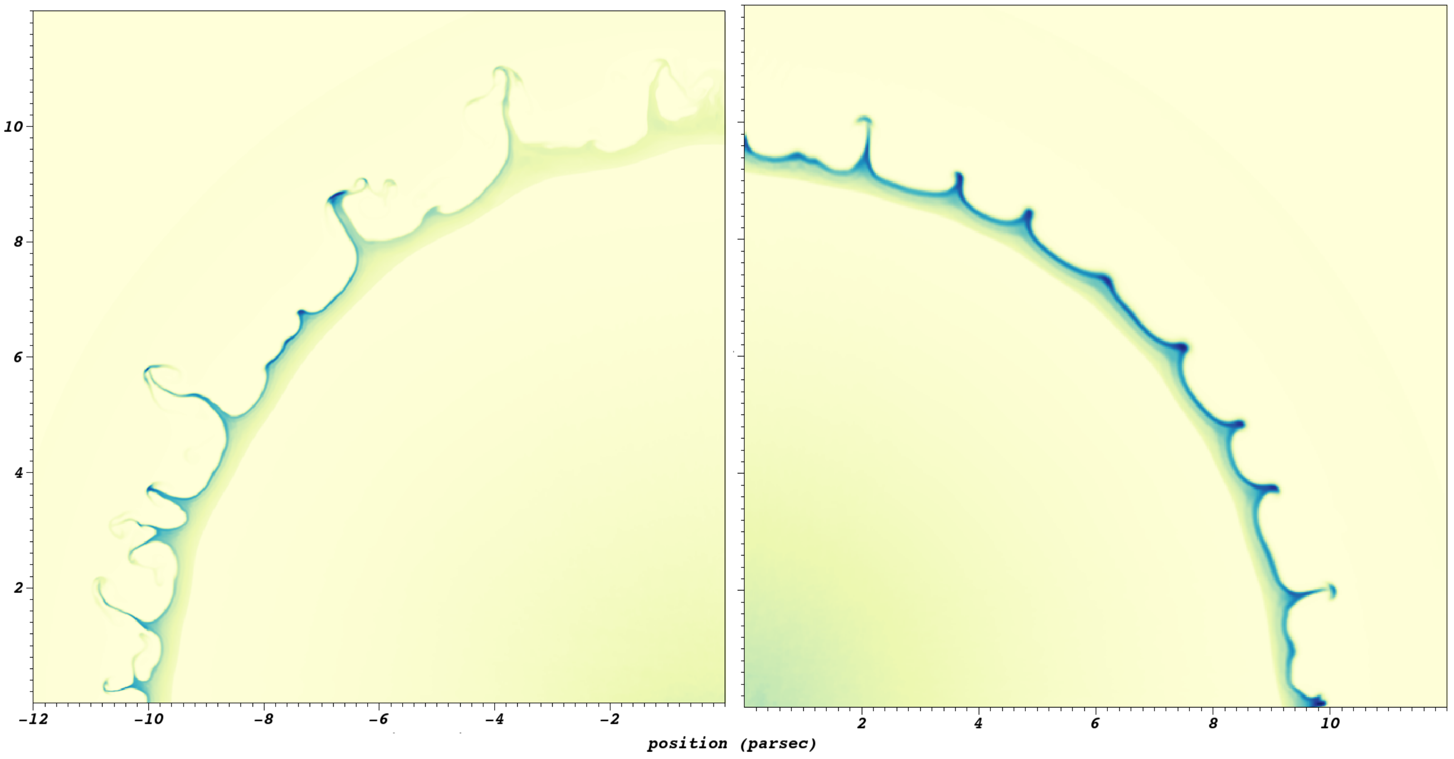

Figure 4.3: Linear number density-squared plot of the $\gamma = 5/3$ and MHD+CR models with fixed min/max values as described in the text, both having ages of $t = 1.3\,\mathrm{kyr}$; the actual maxima are 12.64 and 11.52 cm^{-6}, respectively.

The location of the shocks as a function of time presents little difference between the two models. Figure 4.4 shows the azimuthal-averaged location of the forward shock of the MHD+CR and $\gamma = 5/3$ models. For much of the early life of the remnant, $t < 600\,\mathrm{yrs}$, the locations of the forward shock do differ. However, at later times the difference disappears, indicating an acceleration of the forward shock in the MHD+CR model.

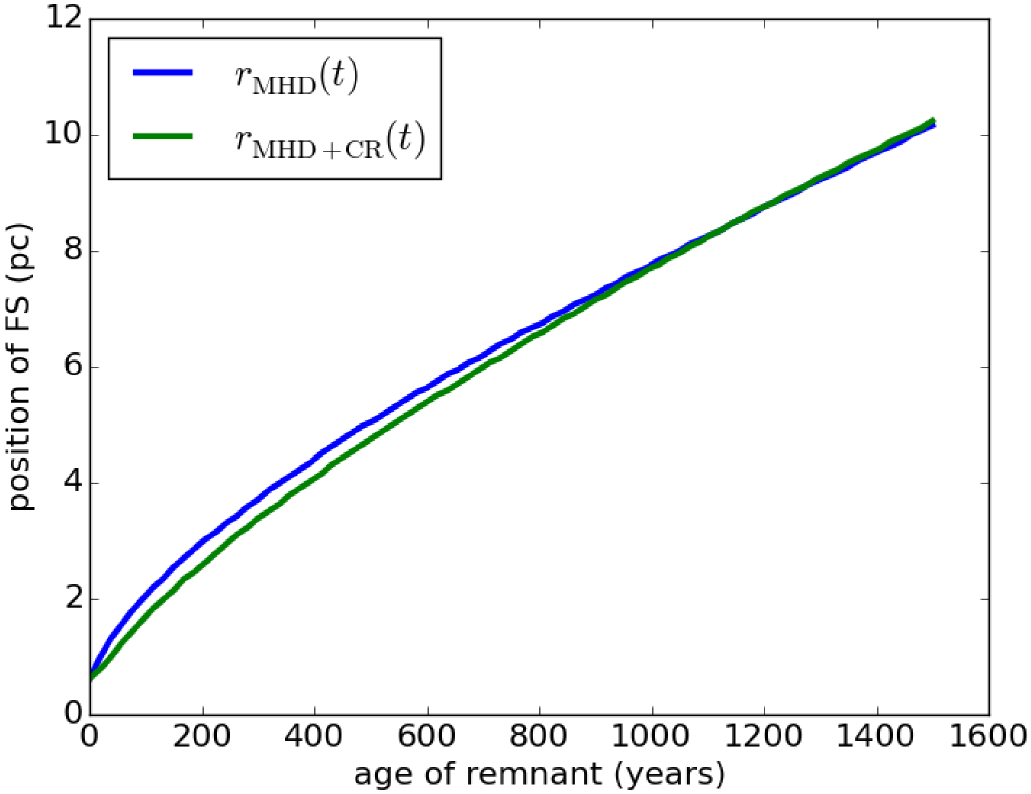

Figure 4.4: Location of the forward shock as a function of time for the two SNR models; in blue is the pure MHD simulation and in green the MHD+CR model.

At $t \approx 1\,\mathrm{kyr}$, the location of the forward shock for the MHD+CR model overtakes the pure magnetohydrodynamic model. This is likely due to slight asymmetries caused by the alignment of the background magnetic field and the method of mapping the hydrodynamic variables from the 2D Cartesian grid it is evolved on to the 1D radial profile. This may be more evident when observing the location of the reverse shock over the whole range, as the two models cross paths a few times. In this early phase of the SNR evolution, the production of cosmic rays has not subtracted a substantial amount of energy, Figure 4.5, to reduce the locations of the shock with respect to the pure MHD comparison case.

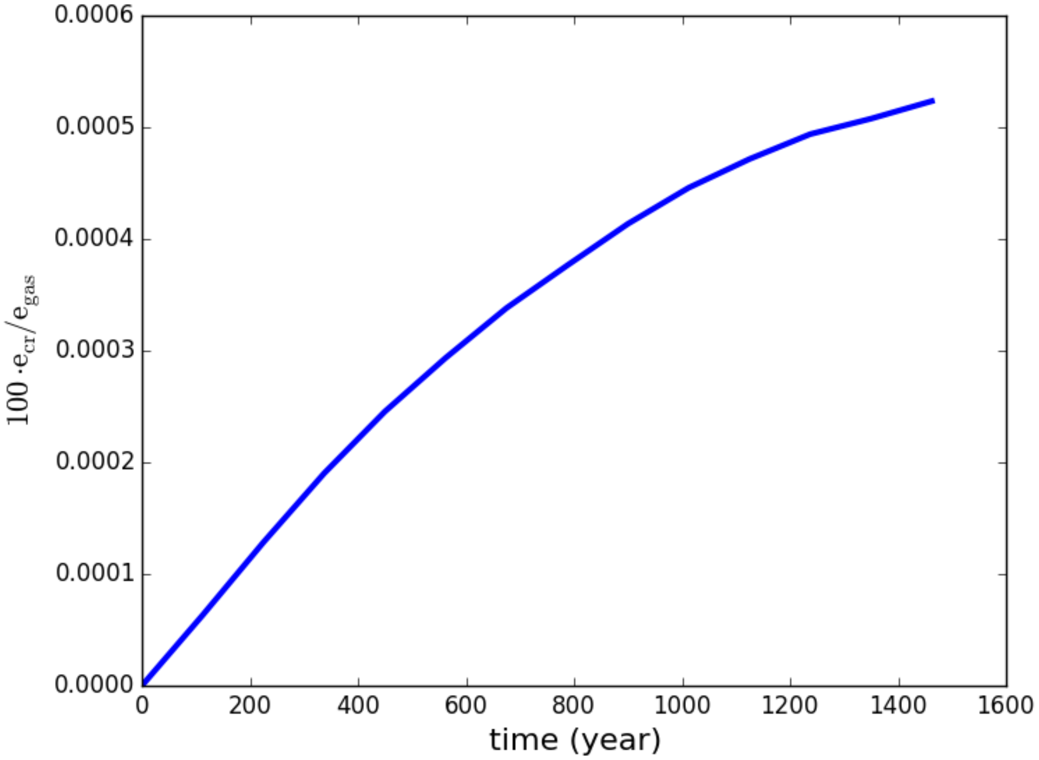

Figure 4.5: Ratio of cosmic ray energy to gas energy as a function of time.

4.2 Cosmic Ray Production

4.2.1 Cosmic Ray Population

Due to the scale of the remnant, the particle population is rather well-contained within the shocked region of the plasma. The diffusion length for the $\mathtt{p} = 2\,\mathrm{GeV}/c$ population is $l_d \approx 3\times10^{12}$ cm, well within a single computational cell. An extension of the model to a larger diffusion coefficient, $D_0 \sim 10^{26}\,\mathrm{cm}^2/\mathrm{s}$, introduced a vacuum solution in the particle population moments, as mentioned in Section 3.2.4[2]. Figure 4.6 shows the color map of the $n_{\ell=9}$ moment, as it the n moment that is associated with number density of CR particles and the 9th moment is the bin covering the $\mathtt{p} = 2\,\mathrm{GeV}/c$ momentum.

The ripples in the moment are due to the injection of new particles and the high advection to diffusion length scales. In this case, the advection length is $l_{adv} = u\,dt \approx 6 \times 10^{15}$ cm, about three orders of magnitude larger than the diffusion length scale. As a result of this, the injection

---

[2] With that diffusivity, the largest momentum bin, $\mathtt{p} \sim 13\,\mathrm{TeV}/c$, would have a diffusion length of 3.6×10^{16} cm, which is larger than the computational cell.

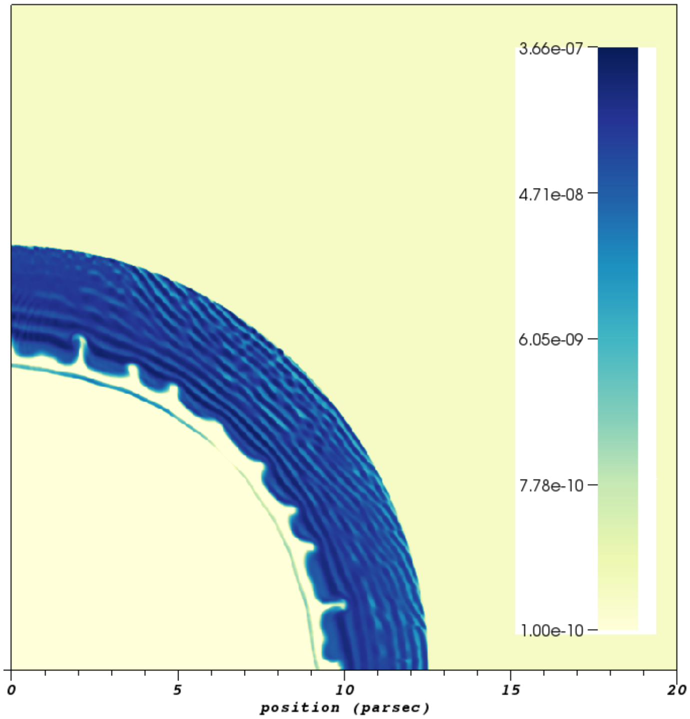

Figure 4.6: $n(\mathtt{p} = 2\,\mathrm{GeV}/c)$ for the SNR model at $t \approx 1.3\,\mathrm{kyr}$, logarithmically scaled between $10^{-10}\,\mathrm{erg/cm^3}$ and $10^{-7}\,\mathrm{erg/cm^3}$. The existence and cause of the ripples are discussed in the text.

occurring at the forward shock builds up a population faster than the existing population can diffuse out, which would smooth the distribution. Figure 4.7 shows $\log_{10} n(\mathtt{p} = 2\,\mathrm{GeV}/c)$ at $t \approx 400\,\mathrm{yr}$ for the preliminary test case in which $D_0 = 3 \times 10^{26}\,\mathrm{cm^2/s}$, such that the $l_{adv}/l_{dif} \approx 10$. In this case here, the diffusion of the population smooths out ripples.

4.2.2 Cosmic Ray Injection

From Section 3.2.2, the injection source term, Equation 3.12, spreads the new CR particles across the shock interface via the weighting function $w(a) \sim \exp(-a^2)$. Figure 4.8 shows a linear colormap of the injection sites, computed by

$$S_{i,j} = \sum_{l=i-n_{nsh}}^{i+n_{nsh}} \sum_{m=j-n_{nsh}}^{j+n_{nsh}} \mathbb{1}\left(M_{i,j}^{max} > M_s\right) \tag{4.3}$$

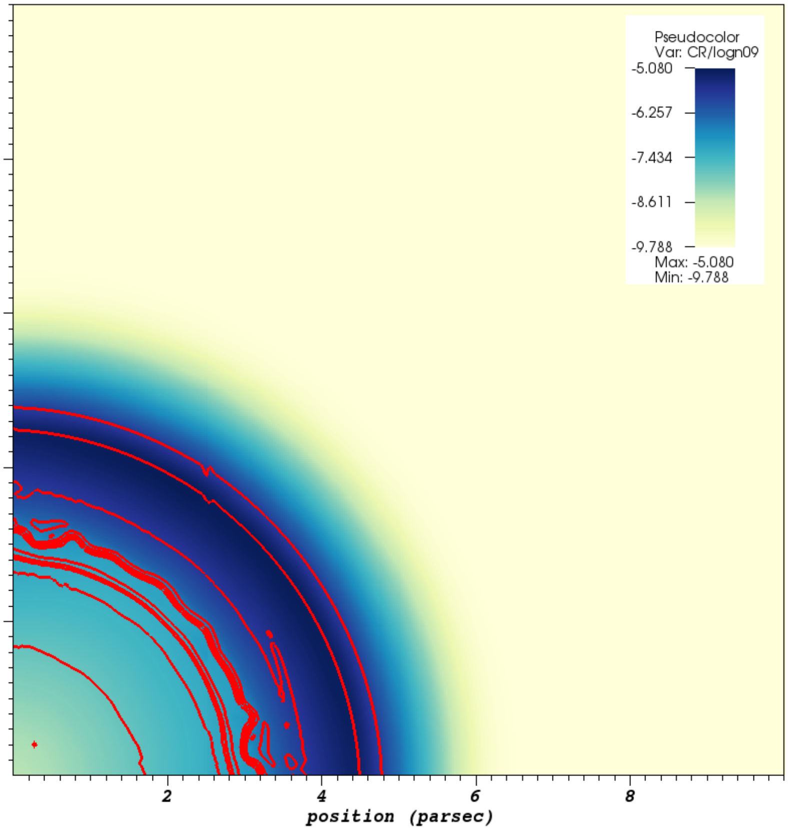

Figure 4.7: Color map of $\log_{10}(n_9)$ at an early phase of a preliminary test case with a high diffusion coefficient, $D_0 = 3 \times 10^{26}\,\mathrm{cm}^2/\mathrm{s}$. Overlaid is the logarithmic density contours, showing that the distribution is diffusing far downstream.

where n_{sh} is the width of the shock, $M_{i,j}^{max}$ is the maximum Mach number across the shock (bounded by $[i - n_{sh},\, i + n_{sh}] \times [j - n_{sh},\, j + n_{sh}]$) and $\mathbb{1}$ is the indicator function,

$$\mathbb{1}\,(a > b) = \begin{cases} 1 & a > b \\ 0 & \text{otherwise} \end{cases} \tag{4.4}$$

Here we choose $M_s = 2$ to be the threshold Mach number for injection.

As expected, the injection sites occur mostly at the forward shock with an alignment of the extended injection sites and the external magnetic field. The cause of the East-West alignment behind the reverse shock is unknown; the Mach number at the shocks in the four cardinal directions are all $\sim$ 15, which is sufficient for injection. While the magnetic field behind the reverse shock along the N,S directions is tangled (North) and aligned quasi-perpendicular (South, not shown) to

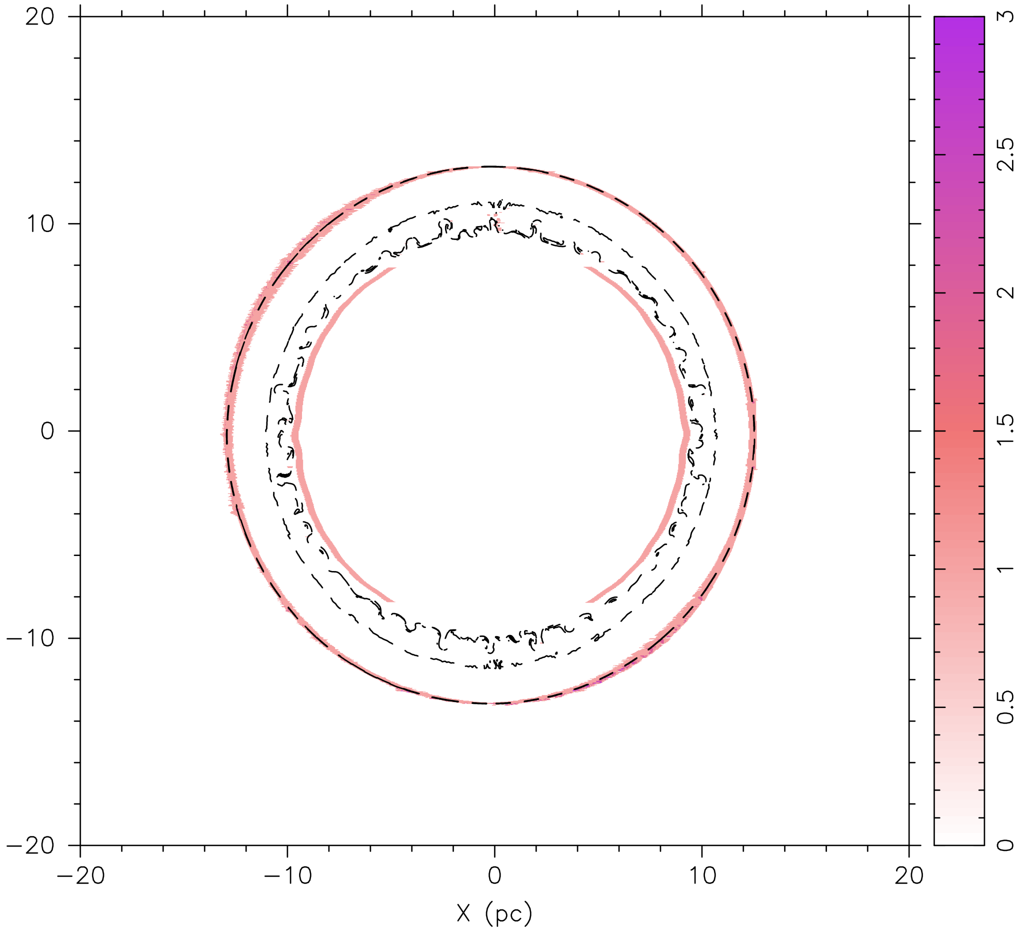

Figure 4.8: Linear colormap of injection sites for the model remnant at $t = 1.3\,\mathrm{kyr}$. Overlaid is the logarithmic density contours, showing that the particles being injected are located near the forward and reverse shocks.

the shock flow, see Figure 4.9, the injection routine does not account for the magnetic field, only the shock strength, so the alignment of the two fields is not sufficient to explain the N-S gap in the injection.

The preliminary simulation, in which the diffusion coefficient was a factor of 100 larger than the work presented, also had an ambient density of $1\,\mathrm{cm}^{-3}$ (10 times larger than the work presented); in this simulation, the same interior asymmetry appears. However, due to the incorrect CR populations leading directly to the failure of the simulation, the comparison of these two models remain unconvincing.

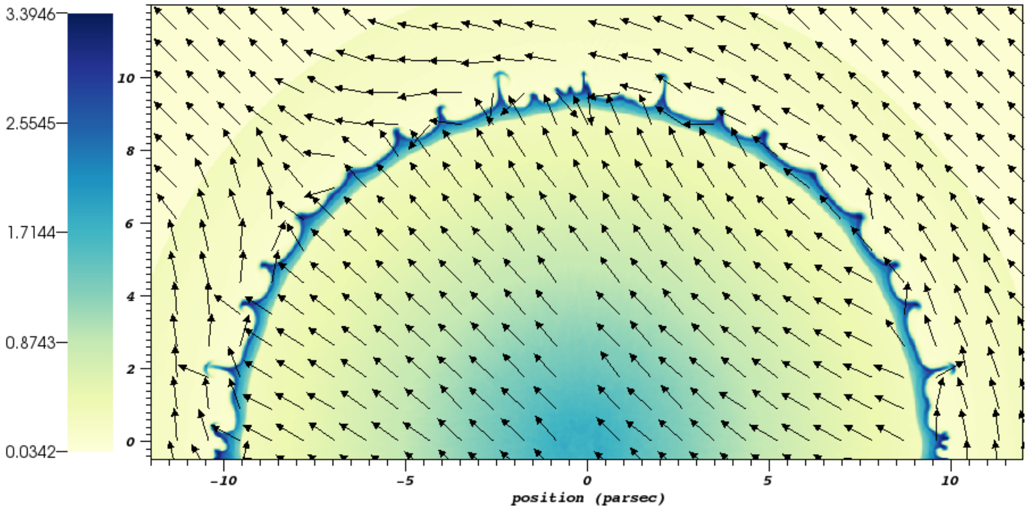

Figure 4.9: Linear colormap of number density for the model remnant at $t = 1.3\,\mathrm{kyr}$ with the arrows representing the magnetic field vectors.

4.2.3 Cosmic Ray Pressure

One of the key aspects to the presence of the highly energetic particle population is the existence of the feedback pressure term, p_{cr}, in Equations 2.20. Figure 4.10 shows the pseudocolor plot of the cosmic ray pressure, with the lower and upper limits set in order to capture the location of the pressure. The interior of the remnant has been evacuated of the pressure term, reducing it to the $p_{cr} \sim 10^{-15}\,\mathrm{erg/cm^3}$ level at the core whereas the ambient is around $p_{cr} \sim 10^{-11}\,\mathrm{erg/cm^3}$.

The injection algorithm described in Section 3.2.2 is agnostic to the location of the shock. So long as the shock exists with sufficient strength, the injection algorithm will deposit fresh particles into the appropriate momentum bin. Particles at the reverse shock can also be drawn into the acceleration mechanism, hence the thin strip of p_{cr} behind the reverse shock in the upper portion of the remnant (see Figure 4.10 above); however it is also unlikely that this population will escape through the shocked material to generate any observable photon.

Two equally important aspects to the cosmic ray pressure are, first, its relation to the gas pressure and, second, the strength of the gradient of the cosmic ray pressure. With regards to the first, Figure 4.11 shows a diverging color map of the gas pressure to cosmic ray pressure ratio. The regions in which the cosmic ray pressure is dominant are colored in red while the regions in which the gas pressure is the dominant pressure is in blue; the white region, which constitutes the shocked gas, the pressures are equivalent.

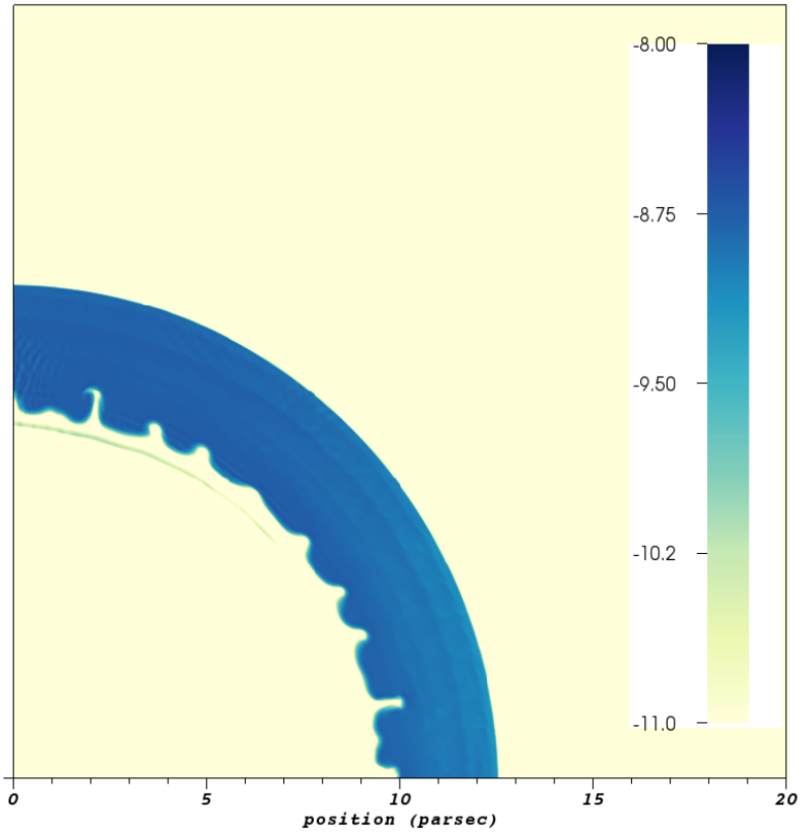

Figure 4.10: Logarithmic color plot of the cosmic ray pressure, p_{cr}, in the upper quarter plane. The bulk of the pressure exists within the shocked region, with a small amount generated near the reverse shock.

As mentioned above, the pressure due cosmic rays in the interior of the remnant is on the order of $10^{-15}\,\mathrm{erg/cm^3}$ while the gas pressure is on the order of $10^{-10}\,\mathrm{erg/cm^3}$, which is on the same scale as the ambient pressure in the interstellar medium for the model. The magnetic pressure, $p_b = \frac{1}{2}b^2$ (not shown), is featured predominantly along the outer edge of the reverse shock along the off-axes (i.e., SW and NE rims); along the direction of the magnetic field, it is slightly smaller in magnitude than the cosmic ray pressure.

With regards to the second point, the magnitude of the pressure gradients, $|\nabla p_{g,cr}|$, can be seen in Figure 4.12, with that of the gas pressure on the left and that of the cosmic ray pressure on the right; both images are of the same time, $t = 1.3\,\mathrm{kyr}$. The magnitude of the cosmic ray pressure[3] scales linearly from 0 to 0.17 (at the forward shock) while the gas pressure scales linearly from 0 to 0.32 (at the forward shock).

---

[3] These are code units, multiply by 3.1×10^{-22} to get it into physical units of $\mathrm{erg/cm^4}$.

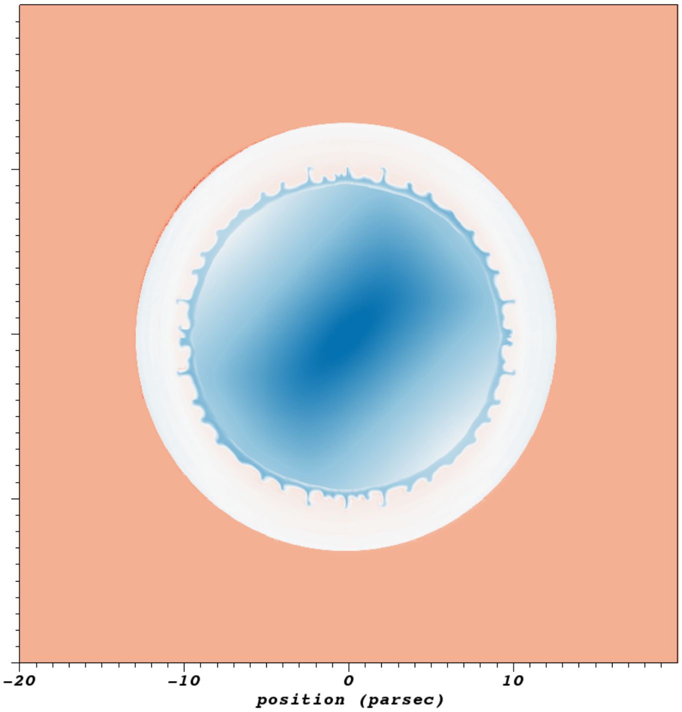

Figure 4.11: Diverging color map of the gas pressure to cosmic ray pressure ratio; red is where p_{cr} dominates over p_{gas}, blue the inverse and the white where the two are equivalent.

It is also interesting to note that the gas pressure features a gradient ahead of and behind the reverse shock (of roughly equal strengths, 0.11 versus 0.14 respectively), the cosmic ray pressure features only a single gradient ahead of the reverse shock. The gradient behind the shock also exists for the $\gamma = 5/3$ model, however the pressure gradient ahead of the reverse shock is significantly weaker, at a value $|\nabla p_{gas}| \sim 0.02$; the gradient at the forward shock is also about 3 times the MHD+CR p_{gas} gradient, with a value of 1.03.

The lack of the third pressure gradient can be attributed to the initially constant cosmic ray pressure and the large velocity of the SNR ejecta. As the SNR kicks out material from the core, the interior is evacuated of the cosmic ray particles; this leads to the vacuum and a lack of the pressure building up behind the reverse shock. Whereas the gas pressure is initialized with a large value in the interior and a lower value in the ambient. As the remnant evolves, the pressure slowly decreases from $p_g \sim 10^{-5}$ to $p_g \sim 10^{-10}$ in the interior, but is still driving the reverse shock, hence the appearance of the third gradient.

The gas pressure in the SNR also changes with the presence of the cosmic rays. Figure 4.13

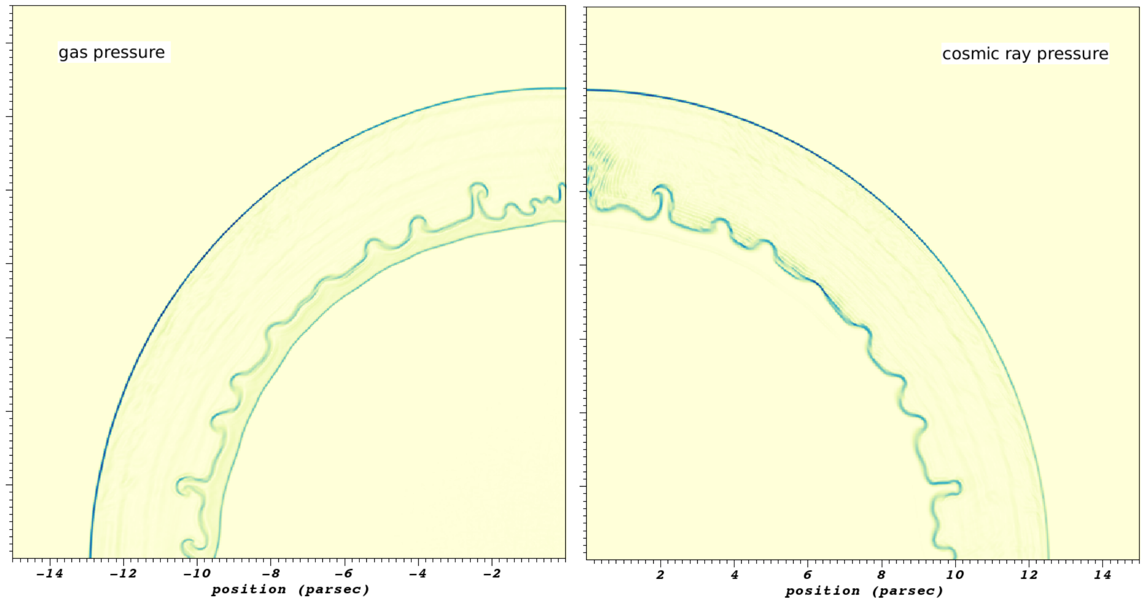

Figure 4.12: Magnitudes of the gradients of the gas pressure (left) and cosmic ray pressure (right). The gas pressure features a gradient behind the reverse shock that the cosmic ray pressure does not.

shows the azimuthal averages of the gas pressures at $t \approx 800\,\mathrm{yrs}$ for the $\gamma = 5/3$ (red) and MHD+CR (blue) models. The V-structure to the pressure profile is a result of the CR pressure building up at the reverse shock. The gas pressure for the MHD+CR is reduced by ~50% as compared to the $\gamma = 5/3$ case; using the net pressure, $p_{gas} + p_{cr}$, the production of cosmic rays reduces the pressure by 26%.

4.3 Synthetic Spectra

4.3.1 Synthetic X-ray Emissions

In the low-density regime, the X-ray emission coefficient can be approximated as,

$$j_\nu(n, T) \approx n_e^2 \xi(T) \tag{4.5}$$

where n_e is the number density of electrons (with the additional assumption $n_e \approx n_H$), T the temperature of the computational cell and $\xi(T)$ a smoothly varying function of temperature (Toledo-Roy et al., 2014). Figure 4.14 shows the emission map of the soft X-ray (0.2 to 2.0 keV) over the whole remnant. Due to the two dimensional nature of the simulation, this emission map effectively

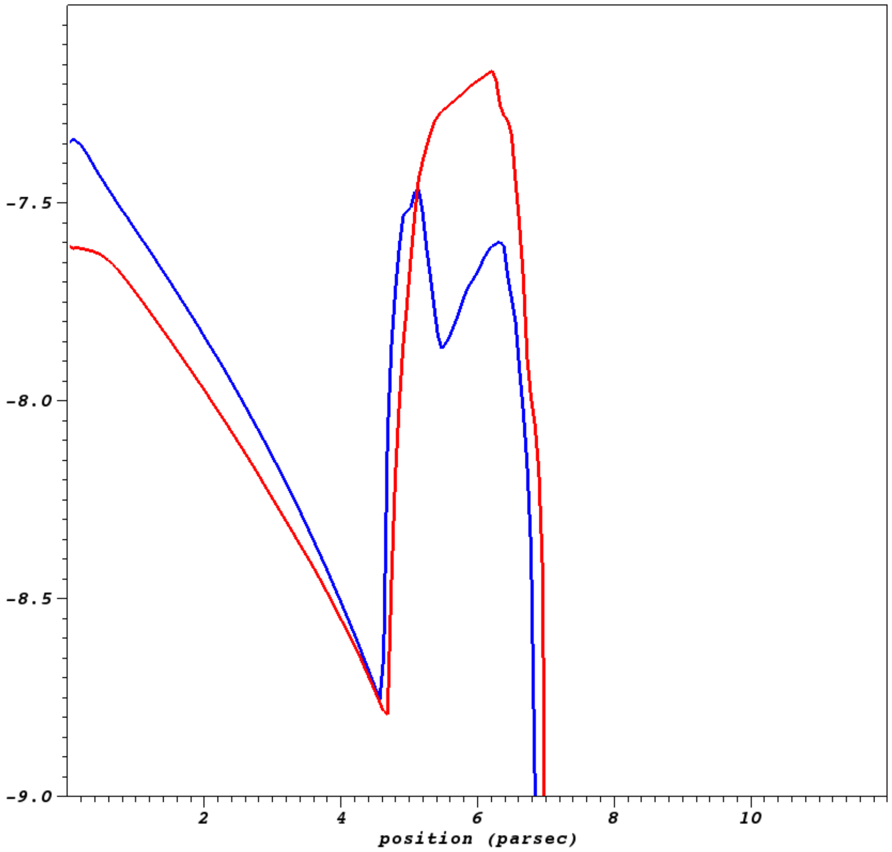

Figure 4.13: Plot of the logarithm of the gas pressure (in erg/cm^3) for the MHD+CR (blue) and $\gamma = 5/3$ (red) simulations. Though not shown, the CR pressure fills the gap in the V-structure.

traces the square of the density (Figure 4.3); a three dimensional simulation would allow for line-of-sight integrations along rotations that are not possible with 2D (see, for instance, Toledo-Roy et al. (2014)).

Still, this can be compared to images of a galactic SNR, such as Cassiopeia A in Figure 4.15 below. The brightest portion of the remnant is the interaction region of the shocked ejecta, where the temperatures reach ~ 50 million Kelvin and densities of the order of $4\,\mathrm{cm}^{-3}$. For our remnant, at $t \sim 320\,\mathrm{yr}$, the temperatures of the shocked ejecta reach into the 80 million Kelvin range with densities around 1-2 cm^{-3}.

While the goal was not to model Cas A, it is worth pointing out that some of the differences can be attributed to the smaller circumstellar environment in our model. Typical main sequence stellar winds result in densities around $10\,\mathrm{cm}^{-3}$, rather than the $0.1\,\mathrm{cm}^{-3}$ chosen for this model. One

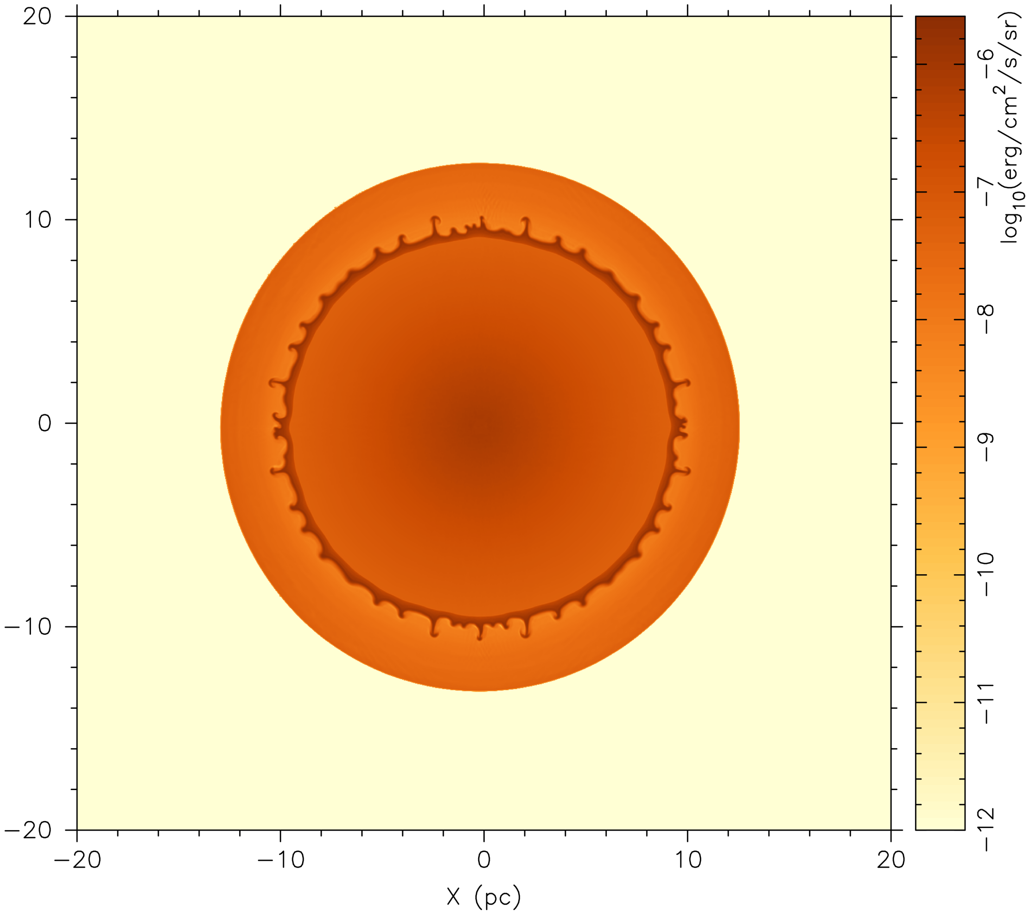

Figure 4.14: Synthetic emission map of 0.2-2 keV X-rays, color map is logarithmic in intensity; the line-of-sight column density is assumed to be 10^{21} cm.

of the preliminary test models used an ambient density of $1\,\mathrm{cm}^{-3}$, however, the simulation failed to evolve the remnant in an accurate manner due to numerical issues discussed in Section 3.2.4. The test managed to evolve the simulation to $t \approx 300\,\mathrm{yr}$ before failure; Figure 4.7 shows the density contours (all in red) at this point, with the peak at about 3.2 pc, with $n_{peak} \sim 16\,\mathrm{cm}^{-3}$.

For the high-frequency case ($\nu > \nu_c$), we can approximate the thermal synchrotron emission of the remnant using the relation,

$$L_\nu \simeq \nu^{-\alpha} n^{1-\alpha} p_{gas}^{2\alpha} \left(B_{tot} \sin\psi\right)^{\alpha+1} \tag{4.6}$$

where $\alpha = 0.5$ and ψ is the angle of the magnetic field with respect to the viewer; p_{gas} is used as a proxy for temperature, as $p \sim nT$. The orientation of the magnetic field and the computation of ψ

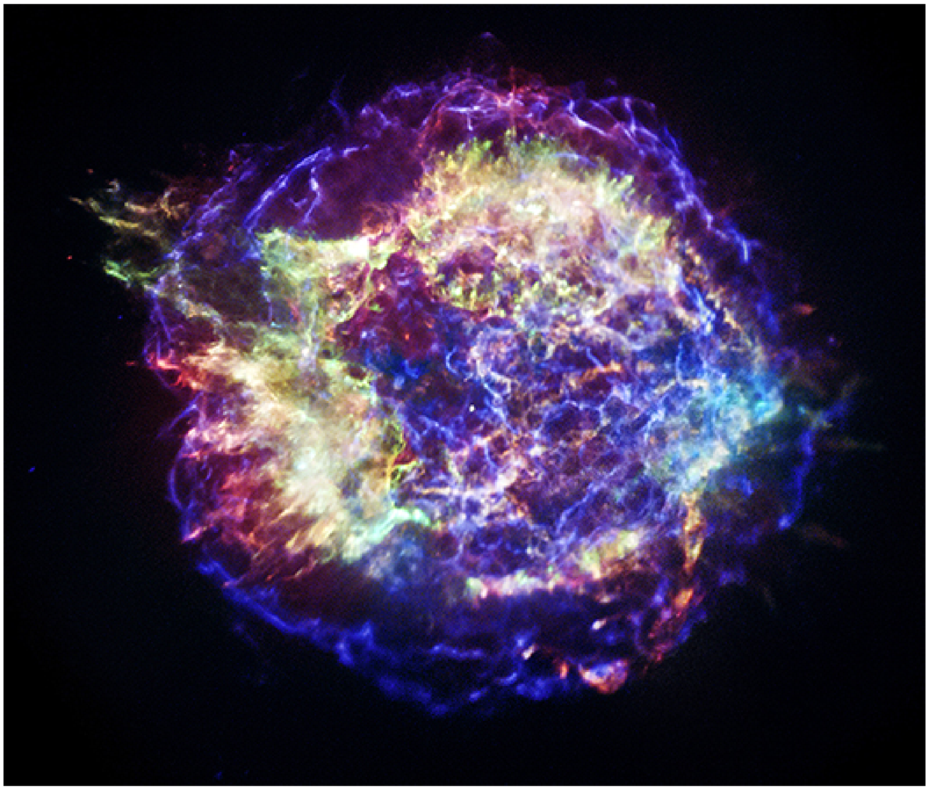

Figure 4.15: False-color image of the galactic SNR, Cas A. Low energy X-rays (~0.2-2 keV) in red, high energy X-rays (~8-10 keV) in blue, while green is the intermediate energies. Image credit: NASA/CXC/SAO

leads to the synchrotron emissivity not aligning with the ambient magnetic field, peaking instead in the $\mathbf{B} \perp \mathbf{u}$ direction.

The evolution of the magnetic field in this simulation also leads to the maxima occurring where the peak of the synchrotron emission found in Figure 4.16 occurs: along the NE/SW direction[4]. Reynoso et al. (2013) suggest that the acceleration efficiency, η in Equation 3.12, varies with the alignment of the magnetic field and the fluid flow, such that the most efficient particle acceleration is when the magnetic field and shock are quasi-parallel.

From the discussion in Section 2.6, some of the thermal emissions in the X-ray regime follow the temperature and density, $L_\nu \propto n^\alpha T^\beta$. In the case of the SNR models, the density peaks at the reverse shock (see Figure 4.1) while the temperature features a maximum value across the whole of the shocked region (of the order 10^8 K). These features are captured in the synthetic models of the X-ray emission from the shocked medium.

---

[4] We are assuming here that north is pointing straight upwards, aligned with the y axis.

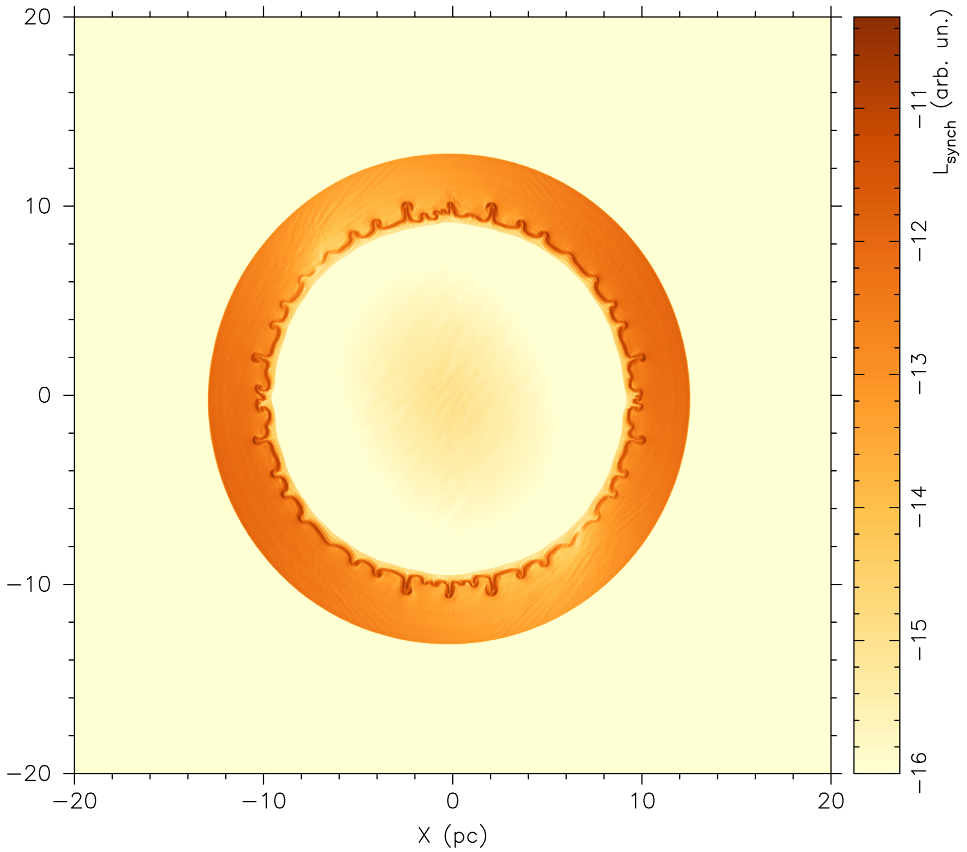

Figure 4.16: Synthetic emission map of synchrotron radiation for the case of $\nu > \nu_c$.

4.3.2 Synthetic γ-ray emissions

The cosmicp code mentioned in Section 3.2.5 is accurate to 1% when there are $\gtrsim 10$ energy bins per decade in energy. In order to capture the full spectrum, we require 10 decades of energy, from $E_\gamma = 10^{-5}$ GeV to $E_\gamma \sim 10^5$ GeV. However, the CGMV method employed in AstroBEAR uses only 16 total energy bins for the range $E_\gamma = 10^{-5}$ GeV to $E_\gamma = 10^4$ GeV, which presents a problem of resolution.

To remedy this, we use a polynomial interpolation to fill in the extra energy bins between the known data points. From the n known points, we can construct a polynomial of the form

$$p(x) = \sum_{i=0}^{n} \left(\prod_{0 \le j \le n, j \ne i} \frac{x - x_j}{x_i - x_j} \right) y_i \tag{4.7}$$

However, this introduces large oscillations, called Runge's phenomenon, near the boundaries. To overcome this issue, we use a piecewise interpolation where $n = 3$, choosing the closest three points to x.

From the `cosmicp` code, we generated a sequence of emission maps at ~ 20 year intervals. Figure 4.17 shows the remnant in γ-ray, due solely to the pion decay. The resolution of the map was artificially reduced so as to reproduce the expected image of an SNR as observed by *Fermi-LAT*; using the actual resolution from the simulation would result in an image similar to that of Figure 4.14. The region exterior to the remnant was also ignored in the computation of the emission, as the focus is on the signal from the remnant itself.

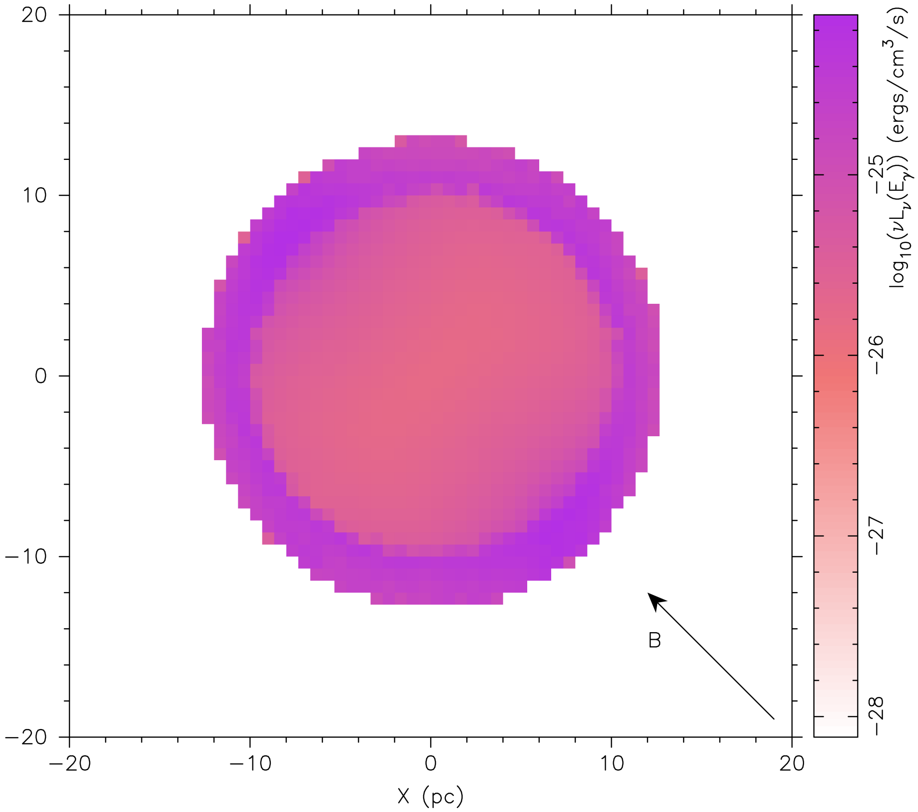

Figure 4.17: Synthetic emission map due to the production of cosmic ray protons in the model SNR.

The emissions trace the shocked region, where the remnant has swept up and accelerated ambient particles. The diffuse emissions in the interior are an artifact of the original particle spectra in that region. This expected feature follows the picture shown in Figure 4.6: the particle population exists mostly in the shock, with a diffuse population in the interior.

Though the pion decay would be unaffected by the existence of the magnetic field, the emissions from the interior seem to be slightly stronger along the direction parallel to the magnetic field, rather than the anti-parallel direction. Figure 4.18 shows the TeV emission of the galactic SNR SN 1006 (Acero et al., 2010), in which the largest emissions are along the NE and SW rims[5] In this case, the magnetic field points along the direction of the two bright lobes (Reynoso et al., 2013). Referring back to Figure 4.11, the cosmic ray pressure also appears to be dominant behind the reverse shock along the direction of the magnetic field, which would lead to the stronger emission in that region, as p_{cr} is a measure of the the particle population.

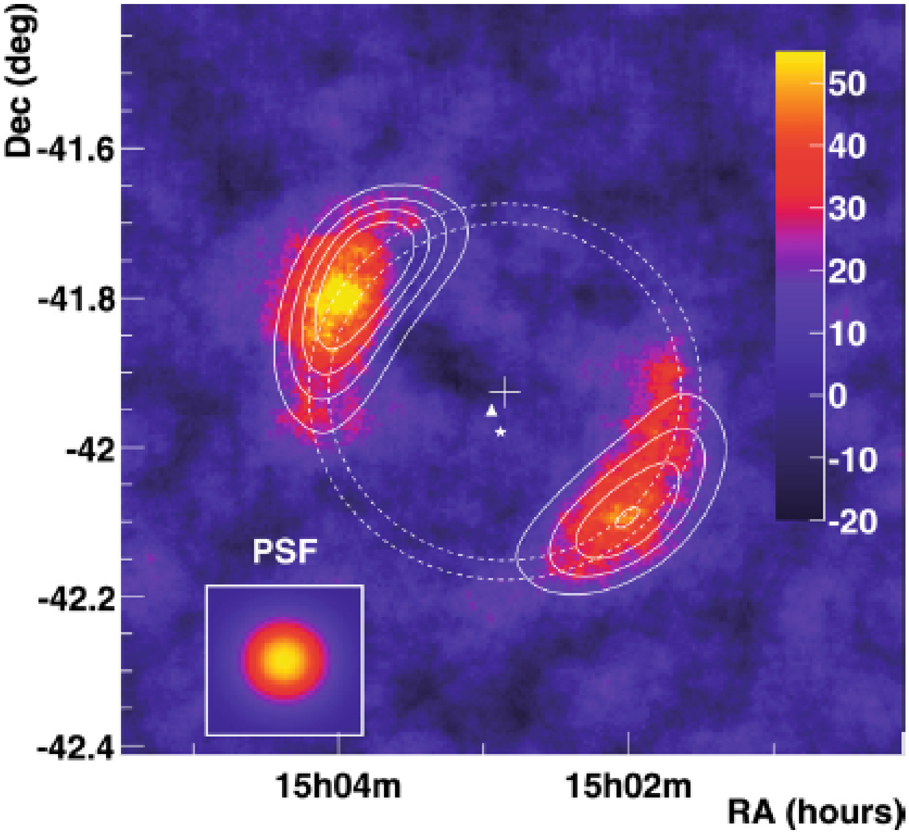

Figure 4.18: HESS γ-ray image of SN 1006; the linear color scale is in units of excess counts per $\pi \times (0.05^\circ)^2$. The white contours correspond to constant X-ray intensity from XMM-Newton. From Acero et al. (2010)

Integrating over the whole remnant shell, the γ-ray emissions from the remnant can be seen in Figure 4.19. For the leptonic emissions, we assume that the CR population evolved by AstroBEAR has a leptonic component that is appropriately scaled (see Footnote 7 in Chapter 2). We also set

---

[5] The West & East directions for SN 1006 are backwards compared to our terminology.

the distance of the remnant to 2 kpc. The asymmetry of the pion spectrum is due to the index being less than 2. The red curve in the image is the total emissions due to the decay of the pion and bremsstrahlung radiation.

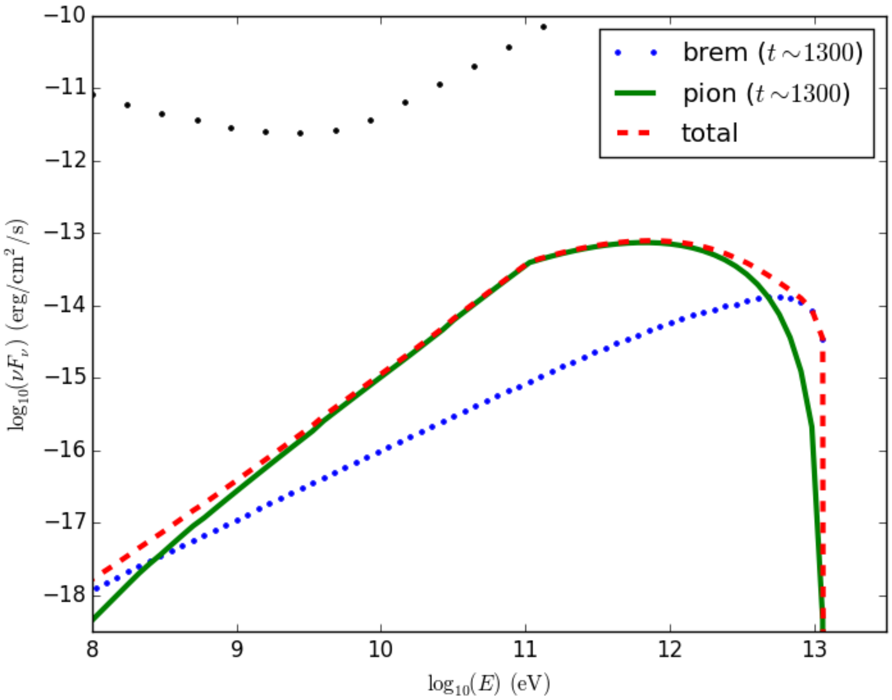

Figure 4.19: Integrated γ-ray spectrum of the SNR; the green solid curve is due to the $\pi^0 \rightarrow 2\gamma$ decay and the blue dotted curve that of the bremsstrahlung emission. The differential sensitivity of *Fermi-LAT* is well above this limit.

At the peak, the emissions here are roughly 3 orders of magnitude too dim to be observed by *Fermi-LAT*. At the lowest energy limit, where *Fermi-LAT* would be able to detect the difference between π^0 decay and the leptonic emissions, the strength of the emissions are roughly 6 orders of magnitude too dim to observe. At the highest energies, $E_\gamma > 100\,\mathrm{GeV}$, the emissions could be observed by an imaging atmospheric Cherenkov telescope (IACT) such as H.E.S.S. (Aharonian et al., 1997). Figure 4.20 shows the TeV emissions of the model remnant (same colors as Figure 4.19) with the 50 hour on-source sensitivity of H.E.S.S. shown in the black points.

The peak in the TeV range is consistent with the picture of particle acceleration as a function of SNR age. Figure 4.21 shows the γ-ray emissions of five galactic SNRs with different ages. The figure suggests that the younger remnants generate TeV emissions while the older remnants emit primarily in the GeV range. While we have not evolved our remnant to an old age, Figures 4.19 and

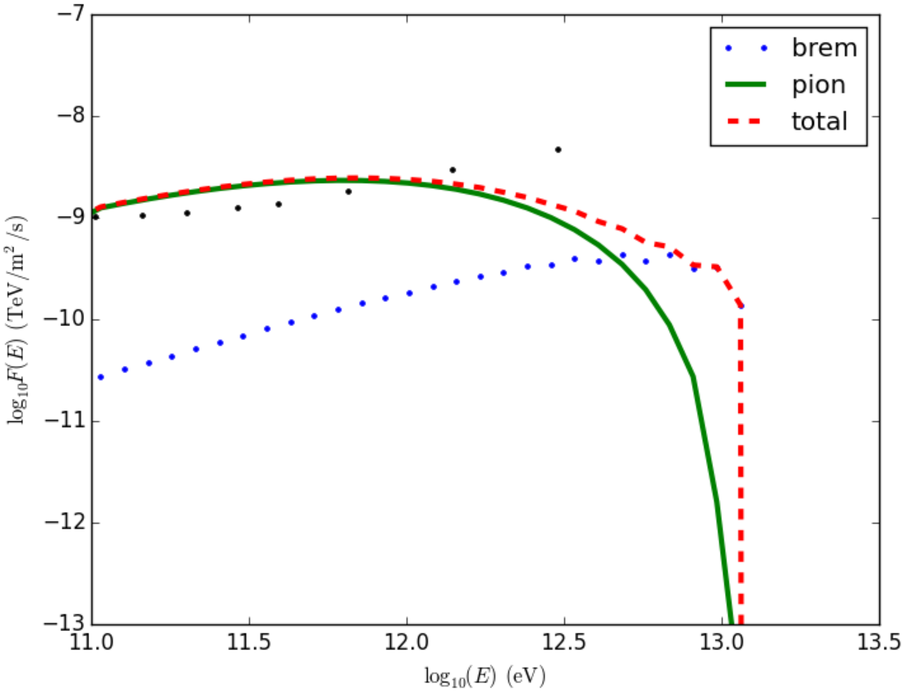

Figure 4.20: The same as Figure 4.19, except looking at the TeV emission spectrum. The black dots are the 50h on-source sensitivity limits for H.E.S.S.

4.20 seem to agree with the understanding of particle acceleration.

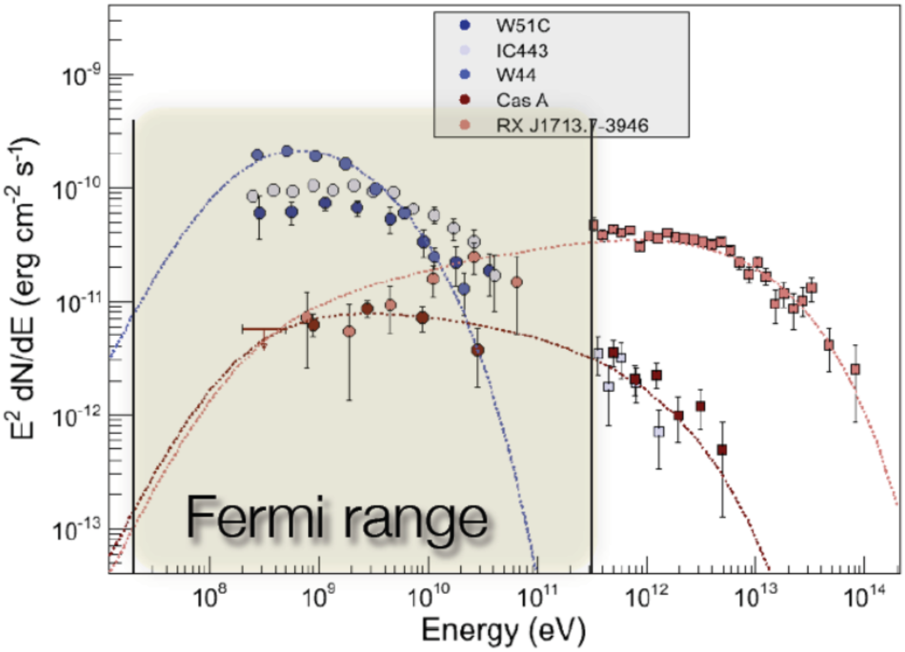

Figure 4.21: The γ-ray emissions from five galactic SNRs (labeled). The SNRs in blue are older than 10,000 years, Cas A (in the darker red) is roughly 300 years old, and RX J1713 (light red) is approximately 1600 years old. From Dermer (2011)

Chapter 5

Summary and Conclusions

In this final chapter, we summarize the dissertation (Section 5.1) and then conclude with a discussion and implications of the results from Chapter 4 (Section 5.2).

5.1 Summary

In Chapter 1, we presented the theory of cosmic ray production in supernova remnants, starting with the first observations of cosmic rays with Victor Hess and coming to present γ-ray observatories *Fermi-LAT* and H.E.S.S. The theory of Fermi acceleration was then presented to discuss a viable method by which a particle can, slowly over a long period of time, gain a substantial amount of energy. The physical model can then be described in the mathematical model of diffusive shock acceleration.

Then, in Chapter 2, we discussed the dynamic evolution of SNRs and methods of modeling them, via the magnetohydrodynamic equations. Incorporating multiple dimensions in the hydrodynamics introduced new possibilities of instabilities growing in the fluid flow, which could be damped through the inclusion of the cosmic ray acceleration. We also discussed the high energy emissions observed from SNRs, what processes can generate emissions in the X-ray and γ-ray regimes.

Chapter 3 presented the method by which we evolve the magnetohydrodynamics and the particle distribution, $f(\mathtt{x}, \mathtt{p}, t)$ in a self-consistent manner, using the code AstroBEAR. We then discussed the origins of the multidimensional diffusive shock acceleration solver algorithm, MAST, as developed by Edmon (2010). The solver allows for simulations of the production of cosmic rays in any shocked medium and in up to two dimensions[1], which allows for a deeper investigation into the role of cosmic ray production in SNR environments.

With this algorithm, we performed simulations of nonlinear CR production in two-dimensional studies of supernova remnant evolution, the first of its kind. We then used the distribution obtained from the simulation as an investigative tool into the production of high energy γ-ray emissions due to the decay of neutral pions. The results were then presented in Chapter 4.

5.2 Conclusion

5.2.1 Production of Cosmic Rays

We have modeled the dynamic evolution of a $4M_\odot$ SNR in a low-density environment with an accurate and efficient DSA solver to correctly capture the feedback mechanism of the cosmic ray pressure. Due to the low-diffusion coefficient used, the kinetic expansion of the gas occurs faster than the particles are able to diffuse downstream, which would normally preheat the ambient. For this reason, the particle population features ripples (see Figure 4.6). At later times, as the remnant grows in size, the diffusion coefficient would increase, allowing for the higher-energy particles to diffuse downstream and preheat the ambient, warning it of the oncoming shock. However, a time-dependent diffusion coefficient is not currently incorporated into the model.

Despite the rippled appearance of the particle population, the cosmic ray pressure still features a smooth distribution, see Figure 4.10. This is due to the fact that the different moments of the distribution function, $f(\mathbf{x}, \mathtt{p}, t)$, have different characteristic diffusion lengths due to the weighted diffusion coefficient,

$$D_{n_\ell} = \frac{1}{n_\ell} \int_{\mathtt{p}_\ell}^{\mathtt{p}_{\ell+1}} D(\mathtt{p})\mathtt{p}^2 f(\mathtt{p})\, d\mathtt{p}, \tag{5.1}$$

$$D_{g_\ell} = \frac{1}{g_\ell} \int_{\mathtt{p}_\ell}^{\mathtt{p}_{\ell+1}} D(\mathtt{p})\mathtt{p}^3 f(\mathtt{p})\, d\mathtt{p}, \tag{5.2}$$

so the distributions can diffuse to different positions, but the net effect of the interpolation of the moments n and g virtually eliminate the ripples in the pressure.

The preliminary test case shown in Figure 4.7 allowed for a larger diffusion length than the model presented, but failed due to numerical issues. The Lagrangian advection scheme used

---

[1] The algorithm is set up so as to allow for three-dimensional simulations, however it has not been tested.

in AstroBEAR, Equation 3.1e, requires that $\psi \leq 1$ and $u/u_{sc} \leq 1$ for stability purposes[2]. At some point before the first output file was written, the lowest three n_ℓ moments increased in magnitude to values > 1, leading to the instabilities that developed; the velocities all stayed less than $u/u_{sc} \leq 0.3$. It is currently unknown how these values manage to increase so greatly, as the initial conditions are otherwise the same between this test and the presented model.

It is well known that the cosmic ray pressure generates a large gradient at the forward shock (Kang et al., 2009); however few studies into the reverse shock have also been performed (Zirakashvili & Ptuskin, 2012). We have found that the cosmic ray pressure acts very strongly at the reverse shock as well (Figure 4.12). This extra pressure gradient is attributed to the agnostic injection algorithm employed which would allow for an injection at any shock. Other models tend to favor particle acceleration at the forward shock due to the fact that it is that population that escapes the forward shock to generate the observed hadronic and/or leptonic emissions.

We find that the existence of the accelerated particles at the reverse shock serves to reduce the flow of the ejecta and stunt the growth of the Rayleigh-Taylor instabilities (see Figures 4.2 and 4.3). It is also possible that the weak diffusion limit used in this model allowed for the build-up of CRs in the shocked region, which in turn gave rise to a pressure term that would, ordinarily, not be present. Thus, more extensive modeling of the SNR+CR interactions are needed to decide which of the two cases it should be.

The acceleration rate of particles is expected to be larger at perpendicular shocks (Ellison et al., 1995), as the magnetic field in the perpendicular region is compressed, increasing the magnetic field gradient. Figure 4.8 shows that the alignment of the perpendicular shock does lead to a wider injection region. As particles are accelerated by the magnetic gradient, a compressed magnetic field should result in a faster acceleration. However, the picture of SN 1006 by Reynoso et al. (2013) suggest that, while this aspect may be true, the brightest emissions come from the parallel shock (Figure 4.18). This could be explained by an increased injection efficiency in the parallel shocks as compared to the perpendicular shocks. Currently, such a spatially-dependent model of injection efficiency is not known.

---

[2] For numerical hydrodynamics, precision can be lost when multiplying a value of magnitude 10^{-8} and another value of magnitude 10^{24}; thus we scale all variables so as to be near 1. Here, $u_{sc} = 3.911 \times 10^9$ cm/s ~ 0.13c.

5.2.2 High Energy Emissions

The magnetohydrodynamics lead to a synthetic synchrotron emission, Figure 4.16, that shows a maximum when the alignment of the magnetic field is perpendicular to the flow, as $L_\nu \propto B_{tot}^{3/2}$. AstroBEAR requires that, for two dimensional studies, the magnetic field in the z direction be zero. If we modeled the remnant in three dimensions and integrated the synchrotron emission along a line of sight, it is likely that the non-zero B_z component of the field would contribute to the synchrotron emission.

The magnetic field evolution follows Faraday's Law, in conjunction with a zero Lorentz force,

$$\frac{\partial \mathbf{B}}{\partial t} = \nabla \cdot (\mathbf{B} : \mathbf{u} - \mathbf{u} : \mathbf{B}) \tag{5.3}$$

So when the two fields are aligned, then the magnetic field is obviously stationary (taking both components to be along the x direction):

$$\frac{\partial B_x}{\partial t} = \nabla \cdot (B_x u_x - u_x B_x) = 0 \tag{5.4}$$

Which should be true for any working model. Due to the limit of two dimensions, the emission map is a slice of the remnant and not the whole of the remnant. Adding a third dimension would obviously increase the simulation run-time, but would give a more accurate picture to the magneto-hydrodynamics, and thus the synchrotron emission.

Non-ideal effects in the magnetic field evolution could also play a role in the anti-alignment. When incorporating the current density, $\mathbf{j} = \eta \nabla \times \mathbf{B}$ with η the resistivity, the Lorentz force law modifies Faraday's equation to be,

$$\frac{\partial \mathbf{B}}{\partial t} = \nabla \cdot (\mathbf{B} : \mathbf{u} - \mathbf{u} : \mathbf{B}) - \nabla \times (\eta \nabla \times \mathbf{B}) \tag{5.5}$$

which can admit a non-zero solution along the parallel:

$$\frac{\partial B_x}{\partial t} = \eta \frac{\partial^2 B_x}{\partial y^2} + \eta \frac{\partial^2 B_x}{\partial z^2} \tag{5.6}$$

where we've assumed that η is either spatially independent or slowly-varying, such that $\nabla \eta = 0$.

It is thought that magnetic reconnection, driven by the resistive MHD model, can be a site of particle acceleration (Lazarian et al., 2012). Due to the nature of the acceleration mechanism in reconnection events, the kinetic DSA method presented here would not be able to model the particle acceleration. However, modeling the magnetic resistivity alongside the DSA mechanism is still an intriguing avenue of research.

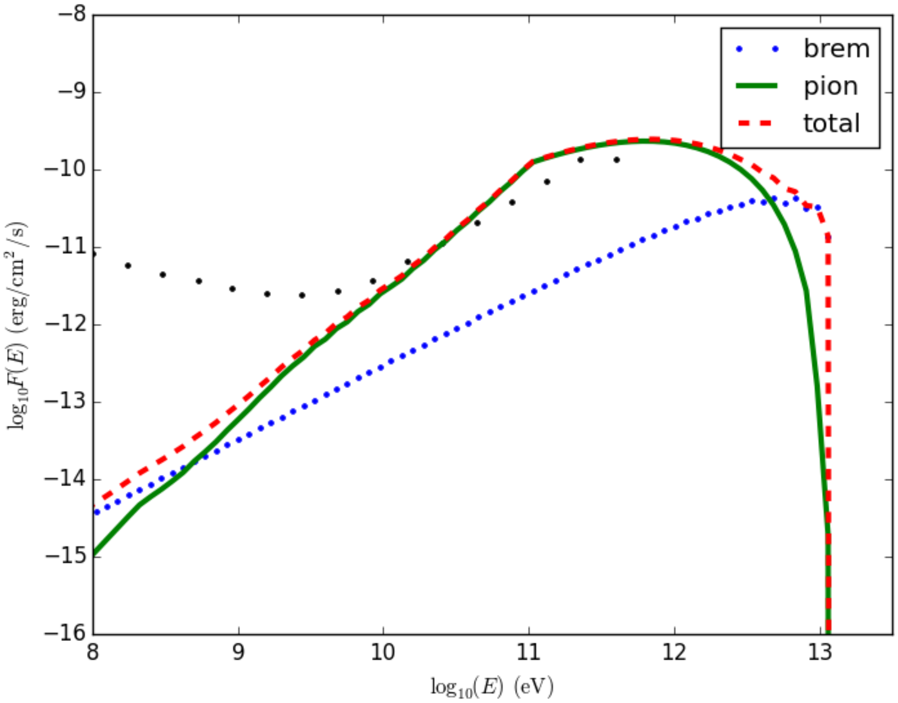

Figure 5.1: Integrated γ-ray spectrum of the SNR when using a molecular cloud of density $n_H \sim 100\,\mathrm{cm}^{-3}$ as the target, rather than the ambient ISM density of $n_H \sim 0.1\,\mathrm{cm}^{-3}$.

As expected, the γ-ray emissions are strongest in the shell of the SNR, with a slight alignment with the background field. Figure 4.19 shows that the integrated emissions of a naked remnant, at $t \approx 1300$ years, would be far too weak to be detectable with *Fermi-LAT*. If we had a molecular cloud, with an ambient density of $n_{MC} \sim 100\,\mathrm{cm}^{-3}$, interacting with this remnant, the signal would increase by three orders of magnitude ($n_{MC}/n_{ISM} \sim 1000$), as the spectrum is linear in ambient density,

$$\frac{dn_{pp,\gamma}}{dE_\gamma\,dt\,dV} = n_H F(E_\gamma) \tag{5.7}$$

where $F(E_\gamma)$ is the result of the integrals of Equation 2.34. Using the molecular cloud as the target would increase the signal by the three orders of magnitude, bringing it into view of *Fermi-LAT* (see Figure 5.1 above). However, the remnant's signal in the 100 MeV range is still too weak for

Fermi-LAT to observe and distinguish the two emission mechanisms.

Note also that this is for a relatively close remnant, at a distance of 2 kpc. Since the flux depends on the distance as D^{-2}, then the signal would rapidly decrease as we assumed a more distant remnant. In order to obtain a observable spectrum at further distances, the production of cosmic rays would have to increase. Since cosmic rays are only added via the injection parameter, we find that it is likely that $\eta > 10^{-4}$ that we have, based on the one dimensional studies, assumed here. Ferrand et al. (2010) show in their study of SNR evolution that the injection efficiency ought to be greater than 5×10^{-4}. Though their simulation was based on dynamically evolving the adiabatic index, the larger value of the injection efficiency will certainly result in a change of the particle spectrum.

From Figure 4.20, we see that the emission from a young, nearby, naked SNR should be observable with an IACT, such as H.E.S.S. The catalog by Ferrand & Safi-Harb (2012) contains 9 objects that were detected with H.E.S.S and not with *Fermi-LAT*. Of those, 3 fit the age criterion of our model, but two are interacting with a molecular cloud and the details of the environment of the third source are currently unknown (Aharonian et al., 2008). With this small sample size of observations and simulations, we cannot conclude or rule out our model the production of *in situ* γ-ray emissions in the early evolution of a naked SNR; however the simulation does present a spectrum that, if the SNR were interacting with a molecular cloud, would be observable with an IACT, giving credence to the model.

While the DSA solver efficiently produced an accurate picture of nonlinear cosmic ray production in supernova remnants, more simulations are required to further understand the role of diffusion and injection in the SNR shell, in particular the role of the magnetic field in both. The future models must also be done in three dimensions, so as to ensure capturing the total emissions, both the synchrotron and pion decay, along the line of sight.

Appendices

Appendix A Rankine-Hugoniot Jump Conditions

A.1 MHD Jump Conditions

The jump conditions come from considering a stationary state ($\partial\mathbf{U}/\partial t = 0$) and looking at the gradient across the x-direction, $d\mathbf{T}/dx = 0$. For the MHD equations, this reduces to,

$$[b_x]_1^2 = 0 \tag{8}$$

$$[u_x b_y - u_y b_x]_1^2 = 0 \tag{9}$$

$$[\rho u_x]_1^2 = 0 \tag{10}$$

$$[\rho u_x^2 + p + \frac{1}{2} b_y^2]_1^2 = 0 \tag{11}$$

$$[\rho u_x u_y - b_x b_y]_1^2 = 0 \tag{12}$$

$$\left[\frac{1}{2}\rho u^2 u_x + \frac{\gamma}{\gamma - 1} p u_x + b_y \left(u_x b_y - u_y b_x\right)\right]_1^2 = 0 \tag{13}$$

where $u^2 = u_x^2 + u_y^2$, $b = B/\sqrt{\mu_0}$, $[A]_1^2 = A_2 - A_1$ and all other terms take their normal meaning.

The general solution to this, using two dimensions, is taking $\mathbf{b} = (b_x, b_y)$ and $\mathbf{u} = (u_x, u_y)$ such that

$$u_x b_y - u_y b_x = 0$$

via Equation (2). From this, Equation (5) reduces to

$$\frac{b_{y,1}}{b_{y,2}} = \sigma \frac{u_2^2 - u_{A,2}^2}{u_2^2 - \sigma u_{A,2}^2} = \sigma \frac{M_{A,2}^2 - 1}{M_{A,2}^2 - \sigma} \tag{14}$$

where $\sigma = \rho_1/\rho_2 = u_2/u_1$ is the compression ratio (see Equation (3)) and $M_A = u/u_A$ is the Alfvenic Mach number[3].

We then compute the pressure ratios from (4) and (6). The first gives us

$$\frac{p_1}{p_2} = 1 + \gamma M_2^2 \left(1 - \frac{1}{\sigma}\right) + \beta_2^{-1} \left[1 + \sigma^2 \left(\frac{M_{A,2}^2 - 1}{M_{A,2}^2 - \sigma}\right)^2\right] \tag{15}$$

while the second gives us

$$\frac{p_1}{p_2} = \sigma + \frac{1}{2}(\gamma - 1) M_2^2 \left[\sigma - \frac{1}{\sigma}\right] \tag{16}$$

---

[3] The Alfvenic Mach number is the Mach number in the *normal* direction, not the tangential direction

where $\beta = p/\frac{1}{2}b^2$ is the ratio of gas pressure to magnetic pressure and $M = u/c_s$ is the Mach number.

Setting these equal to each other, we have,

$$1 + \gamma M_2^2 \left(1 - \frac{1}{\sigma}\right) + \beta_2^{-1} \left[1 + \sigma^2 \left(\frac{M_{A,2}^2 - 1}{M_{A,2}^2 - \sigma}\right)^2\right] = \sigma + \frac{1}{2}(\gamma - 1)M_2^2 \left[\sigma - \frac{1}{\sigma}\right]$$

which reduces to[4]

$$M_2^2 \left[\frac{\sigma}{2}(\gamma - 1) + \frac{1}{2\sigma}(\gamma + 1) - \gamma\right] + \beta_2^{-1} \left[1 + \sigma^2 \left(\frac{M_{A,2}^2 - 1}{M_{A,2}^2 - \sigma}\right)^2\right] + (\sigma - 1) = 0 \qquad (17)$$

In the case of $M_2 \to \infty$, we find that $\sigma \approx (\gamma + 1)/(\gamma - 1)$. If we assume a parallel flow, $b_y = 0$, then we can ignore the β_2 term (i.e., $\beta_2 \to \infty$) as the magnetic terms disappear from (4) and (6). This reduces the above to the common hydrodynamic relation,

$$\sigma = \frac{(\gamma + 1)M_2^2}{(\gamma - 1)M_2^2 + 2} \qquad (18)$$

A.2 Cosmic Ray Modified MHD Jump Conditions

The MHD equations from the previous section are modified slightly such that we account for the particle pressure, p_c,

$$[b_x]_1^2 = 0 \qquad (19)$$

$$[u_x b_y - u_y b_x]_1^2 = 0 \qquad (20)$$

$$[\rho u_x]_1^2 = 0 \qquad (21)$$

$$[\rho u_x^2 + p + \frac{1}{2}b_y^2 + p_c]_1^2 = 0 \qquad (22)$$

$$[\rho u_x u_y - b_x b_y]_1^2 = 0 \qquad (23)$$

$$\left[\frac{1}{2}\rho u^2 u_x + \frac{\gamma}{\gamma - 1} p u_x + b_y\left(u_x b_y - u_y b_x\right) + p_c u_x\right]_1^2 = 0 \qquad (24)$$

---

[4] To account for angles, $M_A \to M_A(\cos\theta)^{-1}$ and $\beta \to \beta(\sin\theta)^{-2}$ where the magnetic field components used, b_x, b_y, are replaced with the magnitude $|b|$.

The analysis is very much the same leading to only a slightly modified version of the previously determined jump conditions,

$$\begin{aligned} M_2^2 \left[\frac{\sigma}{2}(\gamma-1) + \frac{1}{2\sigma}(\gamma+1) - \gamma\right] + \beta_2^{-1} \left[1 + \sigma^2 \left(\frac{M_{A,2}^2 - 1}{M_{A,2}^2 - \sigma}\right)^2\right] \\ +(\sigma - 1) + \frac{p_{c,2}}{p_2}\left[\frac{\gamma\sigma - \sigma - \gamma}{\gamma}\right] + \frac{1}{\gamma}\frac{p_{c,1}}{p_2} = 0 \end{aligned} \tag{25}$$

The unfortunate side-effect of incorporating the cosmic ray pressure in the (magneto)hydrodynamics is that the new pressure terms eliminate the ability to solve the jumps purely in terms of the downstream region, due to the presence of the $p_{c,1}/p_2$ term.

Appendix B Derivation of Differential Energy Spectrum

Beginning with Equations 1.7 and 1.9,

$$N_n = (1 - P_{esc})^n N_0 \tag{1}$$

$$E_n = (1 + \alpha)^n E_0 \tag{2}$$

where $P_{ret} = 1 - P_{esc}$. We then take the natural logarithm of this,

$$\log\left(\frac{N_n}{N_0}\right) = n \log(1 - P_{esc}) \tag{3}$$

$$\log\left(\frac{E_n}{E_0}\right) = n \log(1 + \alpha) \tag{4}$$

which gives us n from both equations,

$$n = \frac{\log(N_n/N_0)}{\log(1 - P_{esc})} \tag{5}$$

$$n = \frac{\log(E_n/E_0)}{\log(1 + \alpha)} \tag{6}$$

Then setting these two equal to each other, we obtain

$$\frac{\log(N_n/N_0)}{\log(1 - P_{esc})} = \frac{\log(E_n/E_0)}{\log(1 + \alpha)} \tag{7}$$

Since both the energy gain, α, and escape probability, P_{esc}, are constants (see below), we can define

$$s = \frac{\log(1 - P_{esc})}{\log(1 + \alpha)} \tag{8}$$

we obtain

$$\log\left(\frac{N}{N_0}\right) = s \log\left(\frac{E}{E_0}\right) \tag{9}$$

or

$$\frac{N}{N_0} = \left(\frac{E}{E_0}\right)^s \tag{10}$$

and

$$\frac{dN}{dE} = \frac{N_0 s}{E_0}\left(\frac{E}{E_0}\right)^{s-1} \tag{11}$$

which is Equation 1.10.

The rate at which particles cross the shock is $nc/4$ (regardless of direction) where n is the number density of particles. The particles are advected downstream at a rate of $nU/4$ (where U is the shock velocity). Thus, the fraction of particles lost is

$$P_{esc} = \frac{nU/4}{nc/4} = \frac{U}{c} \tag{12}$$

Which, since $U \ll c$, means very few particles escape, as expected. The logarithm of one minus this is then,

$$\log(1 - P_{esc}) = \log\left(1 - \frac{U}{c}\right) \approx -\frac{U}{c} \tag{13}$$

and similarly for the energy gain term,

$$\log\left(1 + \alpha\right) = \log\left(1 + \frac{4}{3}\beta\right) \approx \frac{4}{3}\frac{V}{c} = \frac{U}{c} \tag{14}$$

where the V is the velocity at which the particle sees the shock in either frame and is equal to $3U/4$, hence the canceling of the 4/3 term. Thus, $s = -1$ and Equation 11 is

$$\frac{dN}{dE} = \frac{N_0 s}{E_0}\left(\frac{E}{E_0}\right)^{-2} \tag{15}$$

Appendix C Non-dimensionalized Hydrodynamic Equations

Using the primitive variables, ρ, u, p_{gas} instead of the conservative variables $\rho, \boldsymbol{\pi}, E$, the Eulerian hydrodynamics equations become

$$\frac{\partial \rho}{\partial t} = -\nabla \cdot \rho \mathbf{u} \tag{1}$$
$$\frac{\partial u}{\partial t} = -\mathbf{u} \cdot \nabla \mathbf{u} - \frac{1}{\rho}\nabla p_{gas} \tag{2}$$
$$\frac{\partial p_{gas}}{\partial t} = -\mathbf{u} \cdot \nabla p_{gas} - \rho c_s^2 \nabla \cdot \mathbf{u} \tag{3}$$

where $c_s^2 = \gamma p_{gas}/\rho$ is the adiabatic speed of sound for an ideal gas. For the general spherically symmetric case,

$$\nabla \cdot \mathbf{A} = \frac{1}{r^s}\frac{\partial r^s A_r}{\partial r}$$

where $s = 0$ for a planar coordinate system, $s = 1$ for a cylindrical coordinate system, and $s = 2$ for a spherical coordinate system. The primitive equations then become,

$$\frac{\partial \rho}{\partial t} = -\frac{1}{r^s}\frac{\partial}{\partial r}\left(r^s \rho u\right) \tag{4}$$
$$\frac{\partial u}{\partial t} = -u\frac{\partial u}{\partial r} - \frac{1}{\rho}\frac{\partial p_{gas}}{\partial r} \tag{5}$$
$$\frac{\partial p_{gas}}{\partial t} = -u\frac{\partial p_{gas}}{\partial r} - \frac{\gamma p_{gas}}{\rho}\left(\frac{\partial \rho}{\partial t} + u\frac{\partial \rho}{\partial r}\right) \tag{6}$$

where u is the radial velocity and Equation 1 was used in the last line. Applying the derivatives,

$$\frac{\partial \rho}{\partial t} = -u\frac{\partial \rho}{\partial r} - \rho\left(\frac{\partial u}{\partial r} + \frac{su}{r}\right) \tag{7}$$
$$\frac{\partial u}{\partial t} = -u\frac{\partial u}{\partial r} - \frac{1}{\rho}\frac{\partial p_{gas}}{\partial r} \tag{8}$$
$$\frac{\partial p_{gas}}{\partial t} = -u\frac{\partial p_{gas}}{\partial r} - \frac{\gamma p_{gas}}{\rho}\left(\frac{\partial \rho}{\partial t} + u\frac{\partial \rho}{\partial r}\right) \tag{9}$$

Then using the relations

$$u \equiv \dot{R}U(\eta), \qquad \rho \equiv \rho_0 \Omega(\eta), \qquad p = \rho_0 \dot{R}^2 P(\eta) \tag{10}$$

and

$$\frac{\partial h(\eta)}{\partial t} = \frac{\partial h}{\partial \eta}\frac{\partial \eta}{\partial t} = -\eta\frac{\dot{R}}{R}h' \tag{11}$$

$$\frac{\partial h(\eta)}{\partial r} = \frac{\partial h}{\partial \eta}\frac{\partial \eta}{\partial r} = \frac{1}{R}h' \tag{12}$$

we get

$$-\rho_0\Omega'\frac{\eta\dot{R}}{R} = -\dot{R}U\rho_0\Omega'\frac{1}{R} - \rho_0\Omega\left(\dot{R}U'\frac{1}{R} + \frac{s}{\eta R}\dot{R}U\right) \tag{13}$$

$$\ddot{R}U - \dot{R}U'\frac{\dot{R}}{R}\eta = -\dot{R}U\dot{R}U'\frac{1}{R} - \frac{1}{\rho_0\Omega}\left(\rho_0\dot{R}^2P'\frac{1}{R}\right) \tag{14}$$

$$2\rho_0\ddot{R}\dot{R}P - \rho_0\dot{R}^2P'\frac{\dot{R}}{R}\eta = -\dot{R}U\rho_0\dot{R}^2P'\frac{1}{R} - \gamma\frac{\rho_0\dot{R}^2P}{\rho_0\Omega}\left(-\rho_0\Omega'\frac{\dot{R}}{R}\eta + \dot{R}U\rho_0\Omega'\frac{1}{R}\right) \tag{15}$$

The first line has a common factor of $\rho_0\dot{R}/R$; the second line has a common factor of $1/R$ but we can also divide by $\dot{R}^2$; the third line has a common factor of ρ_0 but we can also multiply by $R/\dot{R}^3$,

$$-\Omega'\eta = -U\Omega' - \Omega\left(U' + \frac{s}{\eta}U\right) \tag{16}$$

$$\frac{R\ddot{R}}{\dot{R}^2}U - U'\eta = -UU' - \frac{1}{\Omega}P' \tag{17}$$

$$2\frac{R\ddot{R}}{\dot{R}^2}P - P'\eta = -P'U - \gamma P\left(-\eta + U\right)\frac{\Omega'}{\Omega} \tag{18}$$

which can be further reduced to Equation 2.13 by simple rearrangement,

$$\left[U - \eta\right]\Omega' + \Omega U' + \frac{s}{\eta}U\Omega = 0 \tag{19a}$$

$$\frac{R\ddot{R}}{\dot{R}^2}U\Omega + \left[U - \eta\right]U'\Omega + P' = 0 \tag{19b}$$

$$2\frac{R\ddot{R}}{\dot{R}^2}P + \left[U - \eta\right]\left[P' - \gamma P\frac{\Omega'}{\Omega}\right] = 0 \tag{19c}$$

For the blast wave problem, we have that

$$R(t) = \xi \left(\frac{E}{\rho}\right)^{1/5} t^{2/5} \tag{20}$$

$$\dot{R}(t) = \frac{2}{5}\xi \left(\frac{E}{\rho}\right)^{1/5} t^{-3/5} = \frac{2}{5}\frac{R}{t} \tag{21}$$

$$\ddot{R}(t) = -\frac{6}{25}\xi \left(\frac{E}{\rho}\right)^{1/5} t^{-8/5} = -\frac{6}{25}\frac{R}{t^2} \tag{22}$$

so then the product $R\ddot{R}/\dot{R}^2$ becomes

$$\frac{R\ddot{R}}{\dot{R}^2} = (R)\left(-\frac{6}{25}\frac{R}{t^2}\right)\left(\frac{25}{4}\frac{t^2}{R^2}\right) = -\frac{3}{2} \tag{23}$$

and Equation 19 becomes

$$[U-\eta]\,\Omega' + \Omega U' + \frac{s}{\eta}U\Omega = 0 \tag{24a}$$

$$-\frac{3}{2}U\Omega + [U-\eta]\,U'\Omega + P' = 0 \tag{24b}$$

$$-3P + [U-\eta]\left[P' - \gamma P\frac{\Omega'}{\Omega}\right] = 0 \tag{24c}$$

which is Equation 2.15.

Bibliography

Abdo, A. A., Ackermann, M., Ajello, M., Baldini, L., Ballet, J., Barbiellini, G., Baring, M. G., Bastieri, D., Baughman, B. M., Bechtol, K., Bellazzini, R., Berenji, B., Blandford, R. D., Bloom, E. D., Bonamente, E., Borgland, A. W., Bregeon, J., Brez, A., Brigida, M., Bruel, P., Burnett, T. H., Buson, S., Caliandro, G. A., Cameron, R. A., Caraveo, P. A., Casandjian, J. M., Cecchi, C., Çelik, Ö., Chekhtman, A., Cheung, C. C., Chiang, J., Ciprini, S., Claus, R., Cognard, I., Cohen-Tanugi, J., Cominsky, L. R., Conrad, J., Cutini, S., Dermer, C. D., de Angelis, A., de Palma, F., Digel, S. W., do Couto e Silva, E., Drell, P. S., Dubois, R., Dumora, D., Espinoza, C., Farnier, C., Favuzzi, C., Fegan, S. J., Focke, W. B., Fortin, P., Frailis, M., Fukazawa, Y., Funk, S., Fusco, P., Gargano, F., Gasparrini, D., Gehrels, N., Germani, S., Giavitto, G., Giebels, B., Giglietto, N., Giordano, F., Glanzman, T., Godfrey, G., Grenier, I. A., Grondin, M.-H., Grove, J. E., Guillemot, L., Guiriec, S., Hanabata, Y., Harding, A. K., Hayashida, M., Hays, E., Hughes, R. E., Jackson, M. S., Jóhannesson, G., Johnson, A. S., Johnson, T. J., Johnson, W. N., Kamae, T., Katagiri, H., Kataoka, J., Katsuta, J., Kawai, N., Kerr, M., Knödlseder, J., Kocian, M. L., Kramer, M., Kuss, M., Lande, J., Latronico, L., Lemoine-Goumard, M., Longo, F., Loparco, F., Lott, B., Lovellette, M. N., Lubrano, P., Lyne, A. G., Madejski, G. M., Makeev, A., Mazziotta, M. N., McEnery, J. E., Meurer, C., Michelson, P. F., Mitthumsiri, W., Mizuno, T., Monte, C., Monzani, M. E., Morselli, A., Moskalenko, I. V., Murgia, S., Nakamori, T., Nolan, P. L., Norris, J. P., Noutsos, A., Nuss, E., Ohsugi, T., Omodei, N., Orlando, E., Ormes, J. F., Paneque, D., Parent, D., Pelassa, V., Pepe, M., Pesce-Rollins, M., Piron, F., Porter, T. A., Rainò, S., Rando, R., Razzano, M., Reimer, A., Reimer, O., Reposeur, T., Rochester, L. S., Rodriguez, A. Y., Romani, R. W., Roth, M., Ryde, F., Sadrozinski, H. F.-W., Sanchez, D., Sander, A., Parkinson, P. M. S., Scargle, J. D., Sgrò, C., Siskind, E. J., Smith, D. A., Smith, P. D., Spandre, G., Spinelli, P., Stappers, B. W., Stecker, F. W., Strickman, M. S., Suson, D. J., Tajima, H., Takahashi, H., Takahashi, T., Tanaka, T., Thayer, J. B., Thayer, J. G., Theureau, G., Thompson, D. J., Tibaldo, L., Tibolla, O., Torres, D. F., Tosti, G., Tramacere, A., Uchiyama, Y., Usher, T. L., Vasileiou, V., Venter, C., Vilchez, N., Vitale, V., Waite, A. P., Wang, P., Winer, B. L., Wood, K. S., Yamazaki, R., Ylinen, T., & Ziegler, M. 2010, Science, 327, 1103

Acero, F., Aharonian, F., Akhperjanian, A. G., Anton, G., Barres de Almeida, U., Bazer-Bachi, A. R., Becherini, Y., Behera, B., Beilicke, M., Bernlöhr, K., Bochow, A., Boisson, C., Bolmont, J., Borrel, V., Brucker, J., Brun, F., Brun, P., Bühler, R., Bulik, T., Büsching, I., Boutelier, T., Chadwick, P. M., Charbonnier, A., Chaves, R. C. G., Cheesebrough, A., Conrad, J., Chounet, L.-M., Clapson, A. C., Coignet, G., Dalton, M., Daniel, M. K., Davids, I. D., Degrange, B., Deil, C., Dickinson, H. J., Djannati-Ataï, A., Domainko, W., O'C. Drury, L., Dubois, F., Dubus, G., Dyks, J., Dyrda, M., Egberts, K., Eger, P., Espigat, P., Fallon, L., Farnier, C., Fegan, S., Feinstein, F., Fiasson, A., Förster, A., Fontaine, G., Füßling, M., Gabici, S., Gallant, Y. A., Gérard, L., Gerbig, D., Giebels, B., Glicenstein, J. F., Glück, B., Goret, P., Göring, D., Hauser, D., Hauser, M., Heinz, S., Heinzelmann, G., Henri, G., Hermann, G., Hinton, J. A., Hoffmann, A., Hofmann, W., Hofverberg, P., Holleran, M., Hoppe, S., Horns, D., Jacholkowska, A., de Jager, O. C., Jahn, C., Jung, I., Katarzyński, K., Katz, U., Kaufmann, S., Kerschhaggl, M., Khangulyan, D., Khélifi, B., Keogh, D., Klochkov, D., Kluźniak, W., Kneiske, T., Komin, N., Kosack, K., Kossakowski, R., Lamanna, G., Lemoine-Goumard, M., Lenain, J.-P., Lohse, T., Marandon, V., Marcowith, A., Masbou, J., Maurin, D., McComb, T. J. L., Medina, M. C., Méhault, J., Moderski, R., Moulin, E., Naumann-Godo, M., de Naurois, M., Nedbal, D., Nekrassov, D., Nicholas, B., Niemiec, J., Nolan, S. J., Ohm, S., Olive, J.-F., de Oña Wilhelmi, E., Orford, K. J., Ostrowski, M., Panter, M., Paz Arribas, M., Pedaletti, G., Pelletier, G., Petrucci, P.-O., Pita, S., Pühlhofer, G., Punch, M., Quirrenbach, A., Raubenheimer, B. C., Raue, M., Rayner, S. M., Reimer, O., Renaud, M., de Los Reyes, R., Rieger, F., Ripken, J., Rob, L., Rosier-Lees, S., Rowell, G., Rudak, B., Rulten, C. B., Ruppel, J., Ryde, F., Sahakian, V., Santangelo, A., Schlickeiser, R., Schöck, F. M., Schönwald, A., Schwanke, U., Schwarzburg, S., Schwemmer, S., Shalchi, A., Sushch, I., Sikora, M., Skilton, J. L., Sol, H., Stawarz, Ł., Steenkamp, R., Stegmann, C., Stinzing, F., Superina, G., Szostek, A., Tam, P. H., Tavernet, J.-P., Terrier, R., Tibolla, O., Tluczykont, M., van Eldik, C., Vasileiadis, G., Venter, C., Venter, L., Vialle, J. P., Vincent, P., Vink, J., Vivier, M., Völk, H. J., Volpe, F., Vorobiov, S., Wagner, S. J., Ward, M., Zdziarski, A. A., Zech, A., & H.E.S.S. Collaboration. 2010, A&A, 516, A62

Ackermann, M., Ajello, M., Albert, A., Allafort, A., Atwood, W. B., Axelsson, M., Baldini, L., Ballet, J., Barbiellini, G., Bastieri, D., Bechtol, K., Bellazzini, R., Bissaldi, E., Blandford, R. D., Bloom, E. D., Bogart, J. R., Bonamente, E., Borgland, A. W., Bottacini, E., Bouvier, A., Brandt, T. J., Bregeon, J., Brigida, M., Bruel, P., Buehler, R., Burnett, T. H., Buson, S., Caliandro, G. A., Cameron, R. A., Caraveo, P. A., Casandjian, J. M., Cavazzuti, E., Cecchi, C., Çelik, Ö., Charles, E., Chaves, R. C. G., Chekhtman, A., Cheung, C. C., Chiang, J., Ciprini, S., Claus, R., Cohen-Tanugi, J., Conrad, J., Corbet, R., Cutini, S., D'Ammando, F., Davis, D. S., de Angelis, A., DeKlotz, M., de Palma, F., Dermer, C. D., Digel, S. W., Silva, E. d. C. e., Drell, P. S., Drlica-Wagner, A., Dubois, R., Favuzzi, C., Fegan, S. J., Ferrara, E. C., Focke, W. B., Fortin, P., Fukazawa, Y., Funk, S., Fusco, P., Gargano, F., Gasparrini, D., Gehrels, N., Giebels, B., Giglietto, N., Giordano, F., Giroletti, M., Glanzman, T., Godfrey, G., Grenier, I. A., Grove, J. E., Guiriec, S., Hadasch, D., Hayashida, M., Hays, E., Horan, D., Hou, X., Hughes, R. E., Jackson, M. S., Jogler, T., Jóhannesson, G., Johnson, R. P., Johnson, T. J., Johnson, W. N., Kamae, T., Katagiri, H., Kataoka, J., Kerr, M., Knödlseder, J., Kuss, M., Lande, J., Larsson, S., Latronico, L., Lavalley, C., Lemoine-Goumard, M., Longo, F., Loparco, F., Lott, B., Lovellette, M. N., Lubrano, P., Mazziotta, M. N., McConville, W., McEnery, J. E., Mehault, J., Michelson, P. F., Mitthumsiri, W., Mizuno, T., Moiseev, A. A., Monte, C., Monzani, M. E., Morselli, A., Moskalenko, I. V., Murgia, S., Naumann-Godo, M., Nemmen, R., Nishino, S., Norris, J. P., Nuss, E., Ohno, M., Ohsugi, T., Okumura, A., Omodei, N., Orienti, M., Orlando, E., Ormes, J. F., Paneque, D., Panetta, J. H., Perkins, J. S., Pesce-Rollins, M., Pierbattista, M., Piron, F., Pivato, G., Porter, T. A., Racusin, J. L., Rainò, S., Rando, R., Razzano, M., Razzaque, S., Reimer, A., Reimer, O., Reposeur, T., Reyes, L. C., Ritz, S., Rochester, L. S., Romoli, C., Roth, M., Sadrozinski, H. F.-W., Sanchez, D. A., Saz Parkinson, P. M., Sbarra, C., Scargle, J. D., Sgrò, C., Siegal-Gaskins, J., Siskind, E. J., Spandre, G., Spinelli, P., Stephens, T. E., Suson, D. J., Tajima, H., Takahashi, H., Tanaka, T., Thayer, J. G., Thayer, J. B., Thompson, D. J., Tibaldo, L., Tinivella, M., Tosti, G., Troja, E., Usher, T. L., Vandenbroucke, J., Van Klaveren, B., Vasileiou, V., Vianello, G., Vitale, V., Waite, A. P., Wallace, E., Winer, B. L., Wood, D. L., Wood, K. S., Wood, M., Yang, Z., & Zimmer, S. 2012, ApJS, 203, 4

Ackermann, M., Ajello, M., Allafort, A., Baldini, L., Ballet, J., Barbiellini, G., Baring, M. G., Bastieri, D., Bechtol, K., Bellazzini, R., Blandford, R. D., Bloom, E. D., Bonamente, E., Borgland, A. W., Bottacini, E., Brandt, T. J., Bregeon, J., Brigida, M., Bruel, P., Buehler, R., Busetto, G., Buson, S., Caliandro, G. A., Cameron, R. A., Caraveo, P. A., Casandjian, J. M., Cecchi, C., elik, ., Charles, E., Chaty, S., Chaves, R. C. G., Chekhtman, A., Cheung, C. C., Chiang, J., Chiaro, G., Cillis, A. N., Ciprini, S., Claus, R., Cohen-Tanugi, J., Cominsky, L. R., Conrad, J., Corbel, S., Cutini, S., D'Ammando, F., de Angelis, A., de Palma, F., Dermer, C. D., do Couto e

Silva, E., Drell, P. S., Drlica-Wagner, A., Falletti, L., Favuzzi, C., Ferrara, E. C., Franckowiak, A., Fukazawa, Y., Funk, S., Fusco, P., Gargano, F., Germani, S., Giglietto, N., Giommi, P., Giordano, F., Giroletti, M., Glanzman, T., Godfrey, G., Grenier, I. A., Grondin, M.-H., Grove, J. E., Guiriec, S., Hadasch, D., Hanabata, Y., Harding, A. K., Hayashida, M., Hayashi, K., Hays, E., Hewitt, J. W., Hill, A. B., Hughes, R. E., Jackson, M. S., Jogler, T., Jhannesson, G., Johnson, A. S., Kamae, T., Kataoka, J., Katsuta, J., Kndlseder, J., Kuss, M., Lande, J., Larsson, S., Latronico, L., Lemoine-Goumard, M., Longo, F., Loparco, F., Lovellette, M. N., Lubrano, P., Madejski, G. M., Massaro, F., Mayer, M., Mazziotta, M. N., McEnery, J. E., Mehault, J., Michelson, P. F., Mignani, R. P., Mitthumsiri, W., Mizuno, T., Moiseev, A. A., Monzani, M. E., Morselli, A., Moskalenko, I. V., Murgia, S., Nakamori, T., Nemmen, R., Nuss, E., Ohno, M., Ohsugi, T., Omodei, N., Orienti, M., Orlando, E., Ormes, J. F., Paneque, D., Perkins, J. S., Pesce-Rollins, M., Piron, F., Pivato, G., Rain, S., Rando, R., Razzano, M., Razzaque, S., Reimer, A., Reimer, O., Ritz, S., Romoli, C., Snchez-Conde, M., Schulz, A., Sgr, C., Simeon, P. E., Siskind, E. J., Smith, D. A., Spandre, G., Spinelli, P., Stecker, F. W., Strong, A. W., Suson, D. J., Tajima, H., Takahashi, H., Takahashi, T., Tanaka, T., Thayer, J. G., Thayer, J. B., Thompson, D. J., Thorsett, S. E., Tibaldo, L., Tibolla, O., Tinivella, M., Troja, E., Uchiyama, Y., Usher, T. L., Vandenbroucke, J., Vasileiou, V., Vianello, G., Vitale, V., Waite, A. P., Werner, M., Winer, B. L., Wood, K. S., Wood, M., Yamazaki, R., Yang, Z., & Zimmer, S. 2013, Science, 339, 807

Adriani, O., Barbarino, G. C., Bazilevskaya, G. A., Bellotti, R., Boezio, M., Bogomolov, E. A., Bongi, M., Bonvicini, V., Borisov, S., Bottai, S., Bruno, A., Cafagna, F., Campana, D., Carbone, R., Carlson, P., Casolino, M., Castellini, G., Danilchenko, I. A., De Pascale, M. P., De Santis, C., De Simone, N., Di Felice, V., Formato, V., Galper, A. M., Karelin, A. V., Koldashov, S. V., Koldobskiy, S., Krutkov, S. Y., Kvashnin, A. N., Leonov, A., Malakhov, V., Marcelli, L., Mayorov, A. G., Menn, W., Mikhailov, V. V., Mocchiutti, E., Monaco, A., Mori, N., Nikonov, N., Osteria, G., Palma, F., Papini, P., Pearce, M., Picozza, P., Pizzolotto, C., Ricci, M., Ricciarini, S. B., Rossetto, L., Sarkar, R., Simon, M., Sparvoli, R., Spillantini, P., Stozhkov, Y. I., Vacchi, A., Vannuccini, E., Vasilyev, G., Voronov, S. A., Yurkin, Y. T., Wu, J., Zampa, G., Zampa, N., & Zverev, V. G. 2013, ApJ, 770:2

Aguilar, M., Alberti, G., Alpat, B., Alvino, A., Ambrosi, G., Andeen, K., Anderhub, H., Arruda, L., Azzarello, P., Bachlechner, A., & et al. 2013, Physical Review Letters, 110

Aharonian, F., Akhperjanian, A. G., Barres de Almeida, U., Bazer-Bachi, A. R., Behera, B., Beilicke, M., Benbow, W., Bernlöhr, K., Boisson, C., Bolz, O., Borrel, V., Braun, I., Brion, E., Brown, A. M., Bühler, R., Bulik, T., Büsching, I., Boutelier, T., Carrigan, S., Chadwick, P. M., Chounet, L.-M., Clapson, A. C., Coignet, G., Cornils, R., Costamante, L., Dalton, M., Degrange, B., Dickinson, H. J., Djannati-Ataï, A., Domainko, W., Drury, L. O., Dubois, F., Dubus, G., Dyks, J., Egberts, K., Emmanoulopoulos, D., Espigat, P., Farnier, C., Feinstein, F., Fiasson, A., Förster, A., Fontaine, G., Funk, S., Füßling, M., Gallant, Y. A., Giebels, B., Glicenstein, J. F., Glück, B., Goret, P., Hadjichristidis, C., Hauser, D., Hauser, M., Heinzelmann, G., Henri, G., Hermann, G., Hinton, J. A., Hoffmann, A., Hofmann, W., Holleran, M., Hoppe, S., Horns, D., Jacholkowska, A., de Jager, O. C., Jung, I., Katarzyński, K., Kendziorra, E., Kerschhaggl, M., Khélifi, B., Keogh, D., Komin, N., Kosack, K., Lamanna, G., Latham, I. J., Lemière, A., Lemoine-Goumard, M., Lenain, J.-P., Lohse, T., Martin, J. M., Martineau-Huynh, O., Marcowith, A., Masterson, C., Maurin, D., Maurin, G., McComb, T. J. L., Moderski, R., Moulin, E., de Naurois, M., Nedbal, D., Nolan, S. J., Ohm, S., Olive, J.-P., de Oña Wilhelmi, E., Orford, K. J., Osborne, J. L., Ostrowski, M., Panter, M., Pedaletti, G., Pelletier, G., Petrucci, P.-O., Pita, S., Pühlhofer, G., Punch, M., Ranchon, S., Raubenheimer, B. C., Raue, M., Rayner, S. M., Renaud, M., Ripken, J., Rob, L., Rolland, L., Rosier-Lees, S., Rowell, G., Rudak, B., Ruppel, J., Sahakian, V., Santangelo, A., Schlickeiser, R., Schöck, F., Schröder, R., Schwanke, U., Schwarzburg, S., Schwemmer, S., Shalchi, A., Sol, H., Spangler, D., Stawarz, Ł., Steenkamp, R., Stegmann, C., Superina, G., Tam, P. H., Tavernet, J.-P., Terrier, R., van Eldik, C., Vasileiadis, G., Venter, C., Vialle, J. P., Vincent, P., Vivier, M., Völk, H. J., Volpe, F., Wagner, S. J., Ward, M., Zdziarski, A. A., & Zech, A. 2008, A&A, 477, 353

Aharonian, F. A., Hofmann, W., Konopelko, A. K., & Völk, H. J. 1997, Astroparticle Physics, 6, 343

Alexiades, A., Amiez, G., & Gremaud, P. 1996, Communications in Numerical Methods in Engineering, 12, 31

Alfvén, H. 1946, Stockholms Observatoriums Annaler, 14, 1

Amato, E. 2014, International Journal of Modern Physics D, 23, 30013

Antoni, T., Apel, W. D., Bekk, K., Bernlöhr, K., Bollmann, E., Daumiller, K., Doll, P., Engler, J., Feßler, F., Gils, H. J., Glasstetter, R., Haeusler, R., Hafemann, W., Haungs, A., Heck, D., Hörandel, J. R., Holst, T., Kampert, K.-H., Klages, H. O., Knapp, J., Mathes, H. J., Mayer, H. J., Milke, J., Mühlenberg, D., Oehlschläger, J., Rebel, H., Risse, M., Roth, M., Schatz, G., Schieler, H., Schmidt, F. K., Thouw, T., Ulrich, H., Unger, J., Weber, J. H., Wentz, J., Wiegert, T., Wochele, D., Wochele, J., Kempa, J., Wibig, T., Zabierowski, J., Badea, F., Bozdog, H., Brancus, I. M., Petcu, M., Vulpescu, B., Chilingarian, A., & Vardanyan, A. 1999, Journal of Physics G Nuclear Physics, 25, 2161

Atwood, W. B., Abdo, A. A., Ackermann, M., Althouse, W., Anderson, B., Axelsson, M., Baldini, L., Ballet, J., Band, D. L., Barbiellini, G., & et al. 2009, ApJ, 697, 1071

Atwood, W. B., Bagagli, R., Baldini, L., Bellazzini, R., Barbiellini, G., Belli, F., Borden, T., Brez, A., Brigida, M., Caliandro, G. A., Cecchi, C., Cohen-Tanugi, J., De Angelis, A., Drell, P., Favuzzi, C., Fukazawa, Y., Fusco, P., Gargano, F., Germani, S., Giannitrapani, R., Giglietto, N., Giordano, F., Himel, T., Hirayama, M., Johnson, R. P., Katagiri, H., Kataoka, J., Kawai, N., Kroeger, W., Kuss, M., Latronico, L., Longo, F., Loparco, F., Lubrano, P., Massai, M. M., Mazziotta, M. N., Minuti, M., Mizuno, T., Morselli, A., Nelson, D., Nordby, M., Ohsugi, T., Omodei, N., Ozaki, M., Pepe, M., Rainò, S., Rando, R., Razzano, M., Rich, D., Sadrozinski, H. F.-W., Scolieri, G., Sgrò, C., Spandre, G., Spinelli, P., Sugizaki, M., Tajima, H., Takahashi, H., Takahashi, T., Yoshida, S., Young, C., & Ziegler, M. 2007, Astroparticle Physics, 28, 422

Baade, W. & Zwicky, F. 1934, Phys. Rev., 46, 76

Badenes, C., Borkowski, K. J., Hughes, J. P., Hwang, U., & Bravo, E. 2006, ApJ, 645, 1373

Balsara, D. & Spicer, D. 1999, Journal of Computational Physics, 149, 270

Bamba, A., Yamazaki, R., Ueno, M., & Koyama, K. 2003, ApJ, 589, 827

Becquerel, H. 1896, Comptes rendus de l' Académie des Sciences, 122, 559

Bell, A. 2004, MNRAS, 353, 550

Berger, M. & Colella, P. 1989, J. Comp. Phys., 82, 64

Berger, M. & Oliger, J. 1984, J. Comp. Phys., 53, 484

Bertolotti, M. 2013, Celestial Messengers: Cosmic Rays (Springer)

Blasi, P. 2002, Astroparticle Physics, 16, 429

Blondin, J. & Ellison, D. 2001, ApJ, 560, 244

Blondin, J. M., Wright, E. B., Borkowski, K. J., & Reynolds, S. P. 1998, ApJ, 500, 342

Bregeon, J., Charles, E., & Wood, M. 2013

Burton, M., Hollenbach, D., Haas, M., & Erickson, E. 1990, ApJ, 355, 197

Caprioli, D. 2011, JCAP, 26

Caprioli, D., Amato, E., & Blasi, P. 2010a, Astropart Phys, 33, 307

Caprioli, D., Kang, H., Vladimirov, A., & Jones, T. 2010b, MNRAS, 407, 1773

Carroll-Nellenback, J., Shroyer, B., Frank, A., & Ding, C. 2013, Journal of Computational Physics, 236, 461

Castelletti, G., Dubner, G., Brogan, C., & Kassim, N. E. 2007, A&A, 471, 537

Chevalier, R. 1982, ApJ, 258, 790

Chevalier, R. & Klein, R. 1978, ApJ, 219

Churchwell, E., Babler, B. L., Meade, M. R., Whitney, B. A., Benjamin, R., Indebetouw, R., Cyganowski, C., Robitaille, T. P., Povich, M., Watson, C., & Bracker, S. 2009, Publications of the Astronomical Society of the Pacific, 121, 213

Crank, J. & Nicolson, P. 1947, Proc. Camb. Phil. Soc., 43, 50

Cunningham, A., Frank, A., Varniére, P., Mitran, S., & Jones, T. 2009, ApJSS, 182, 519

Dalgarno, A. & McCray, R. 1972, ARA&A, 10

Dermer, C. 2011 (Fermi Summer School)

Dermer, C. D. 1986, A&A, 157, 223

Dermer, C. D., Strong, A. W., Orlando, E., & Tibaldo, L. 2013, ICRC

Duffy, P., Ball, L., & Kirk, J. G. 1995, ApJ, 447, 364

Edmon, P. 2010, PhD thesis, University of Minnesota

Edmon, P., Kang, H., Jones, T., & Ma, R. 2011, MNRAS, 414, 3521

Ellison, D. C., Baring, M. G., & Jones, F. C. 1995, ApJ, 453

Ellison, D. C. & Bykov, A. 2011, ApJ, 731

Ellison, D. C., Patnaude, D. J., Slane, P., Blasi, P., & Gabici, S. 2007, ApJ, 661, 879

Ellison, D. C., Patnaude, D. J., Slane, P., & Raymond, J. 2010, ApJ, 712, 287

Ellison, D. C., Slane, P., Patnaude, D. J., & Bykov, A. M. 2012, ApJ, 744, 39

Falkenburg, B. & Rhode, W. 2012, From Ultra Rays to Astroparticles (Springer Science+Business Media)

Falle, S. A. E. G. & Giddings, J. R. 1987, MNRAS, 225, 399

Ferland, G. J., Porter, R. L., van Hoof, P. A. M., Williams, R. J. R., Abel, N. P., L., L. M., Shaw, G., Henney, W. J., & Stancil, P. C. 2013, Revista Mexicana de Astronomia y Astrofisica, 49, 127

Ferrand, G., Decourchelle, A., Ballet, J., Teyssier, R., & Fraschetti, F. 2010, A&A, L10

Ferrand, G. & Safi-Harb, S. 2012, Advances in Space Research, 49, 1313

Fraschetti, F., Teyssier, R., Ballet, J., & Decourchelle, A. 2010, A&A, 515

Fryxell, B., Olson, K., Ricker, P., Timmes, F. X., Zingale, M., Lamb, D. Q., MacNeice, P., Rosner, R., Truran, J. W., & Tufo, H. 2000, ApJS, 131, 273

Gabici, S. 2011, PhD thesis, Laboratoire AstroParticule et Cosmologie

Gaisser, T. K., Protheroe, R. J., & Stanev, T. 1998, ApJ, 492, 219

Gehrels, N. & Michelson, P. 1999, Astroparticle Physics, 11, 277

Gerhard, O. 2002, Space Science Reviews, 100, 129

Ginzburg, V. L. & Syrovatskii, S. I. 1964, The origin of cosmic rays (Pergamon Press)

Gleeson, L. J. & Axford, W. I. 1967, ApJ, 149, L115

Gnat, O. & Sternberg, A. 2007, ApJSS, 168, 213

Goedbloed, H. & Poedts, S. 2004, Principles of Magnetohydrodynamics (Cambridge)

Green, D. 2009, Bull. Astr. Soc. India, 37

—. 2014, Bull. Astr. Soc. India

Greisen, K. 1966, Phys. Rev. Lett., 16, 748

Hayashida, N., Honda, K., Honda, M., Imaizumi, S., Inoue, N., Kadota, K., Kakimodo, F., Kamata, K., Kawaguchi, S., Kawasumi, N., Matsubara, Y., Murakami, Y., Nagano, M., Ohoka, H., Takeda, M., Teshima, M., Tsushima, I., Yoshida, S., & Yoshii, H. 1994, Phys. Rev. Lett., 73

Helder, E. A., Vink, J., Bykov, A. M., Ohira, Y., Raymond, J. C., & Terrier, R. 2012, SSRv, 173, 369

Hess, V. 1912, Phys. Z., 13, 1084

Higdon, J. C. & Lingenfelter, R. E. 2005, ApJ, 628, 738

Hillas, A. M. 1984, ARAA

Houck, J. C. & Allen, G. E. 2006, ApJS, 167, 26

Jokipii, J. R. 1987, Astrophys. J., 313, 842

Jones, T. & Kang, H. 2005, Astroparticle Physics, 24, 75

Jun, B. & Jones, T. W. 1997, ApJ, 481, 253

Kaastra, J. S., Mewe, R., & Nieuwenhuijzen, H. in , UV and X-ray Spectroscopy of Astrophysical and Laboratory Plasmas, ed. K. YamashitaT. Watanabe, 411–414

Kaastra, J. S., Paerels, F. B. S., Durret, F., Schindler, S., & Richter, P. 2008, SSRv, 134, 155

Kamae, T., Karlsson, N., Mizuno, T., Abe, T., & Koi, T. 2006, ApJ, 647, 692

Kang, H. 2012, Journal of The Korean Astronomical Society, 45, 111

Kang, H., Edmon, P. P., & Jones, T. W. 2012, ApJ, 745, 146

Kang, H., Jones, T., & Gieseler, U. 2002, ApJ, 579, 337

Kang, H., Jones, T. W., LeVeque, R. J., & Shyue, K. M. 2000, ApJ, 550, 737

Kang, H., Ryu, D., & T., J. 2009, ApJ, 695, 1273

Kappes, A., Hinton, J., Stegmann, C., & Aharonian, F. A. 2007, ApJ, 656, 870

Kelner, S. R., Aharonian, F. A., & Bugayov, V. V. 2006, Phys. Rev. D, 74

Keppens, R., Meliani, R., van Marle, A., Delmont, P., Vlasis, A., & van der Holst, B. 2012, Journal of Computational Physics, 231, 718

Khan, L. & Liu, P. 1998, Int. J. Numer. Meth. Fluids, 28, 461

Kifonidis, K., Plewa, T., Janka, H. T., & Müller, E. 2003, A&A, 408, 621

Kirk, J. 1994, Particle Acceleration (Saas-Fee Lectures)

Landi, E., Del Zanna, G., Young, P. R., Dere, K. P., Mason, H. E., & Landini, M. 2006, ApJS, 162, 261

L'Annunziata, M. 2007, Radioactivity: Introduction and History (Elsevier)

Lazarian, A., Vlahos, L., Kowal, G., Yan, H., Beresnyak, A., & de Gouveia Dal Pino, E. M. 2012, SSRv, 173, 557

Lequeux, J. 2005, The Interstellar Medium (Springer)

Leung, S. & Osher, S. 2005, UCLA Comp. and Applied Math. Report, 11

Leveque, R. 2002, Finite Volume Methods for Hyperbolic Problems (Cambridge University Press)

Linsley, J. 1963, Phys. Rev. Lett., 10, 146

Malkov, M. 1999, ApJ, 511, L53

Malkov, M. & O'C Drury, L. 2001, Rep. Prog. Phys., 64, 429

Marchuk, G. 1990, Handbook of Numerical Analysis, Vol I, Finite Difference Methods (North-Holland)

Matthews, J. N. 2001, Proceedings of the 27th ICRC

Matthiae, G. 2010, NJP, 12

Mignone, A., Bodo, G., Massaglia, S., Matsakos, T., Tesileanu, O., Zanni, C., & Ferrari, A. 2007, ApJSS, 170, 228

Millikan, R. 1925, Phys. Rev., 28, 851

Muraishi, H., Tanimori, T., Yanagita, S., Yoshida, T., Moriya, M., Kifune, T., Dazeley, S. A., Edwards, P. G., Gunji, S., Hara, S., Hara, T., Kawachi, A., Kubo, H., Matsubara, Y., Mizumoto, Y., Mori, M., Muraki, Y., Naito, T., Nishijima, K., Patterson, J. R., Rowell, G. P., Sako, T., Sakurazawa, K., Susukita, R., Tamura, T., & Yoshikoshi, T. 2000, A&A, 354

O'C Drury, L. 1983, Rep. Prog. Phys., 46, 973

Olive, K. A. & et al. (PDG). 2014, Chin. Phys., C38, 090001

O'Sullivan, S. & Downes, T. 2006, MNRAS, 366, 1329

Pacini, D., translated, Michela De Maria, c. b., & De Angelis, A. 2011, arXiv:1101.3015v3

Panov, A. D., Adams, J. H., Ahn, H. S., Bashinzhagyan, G. L., Watts, J. W., Wefel, J. P., Wu, J., Ganel, O., Guzik, T. G., Zatsepin, V. I., Isbert, I., Kim, K. C., Christl, M., Kouznetsov, E. N., Panasyuk, M. I., Seo, E. S., Sokolskaya, N. V., Chang, J., Schmidt, W. K. H., & Fazely, A. R. 2009, BRASP, 73, 564

Parker, E. 1969, Space Sci. Rev, 9, 325

Rampp, M. 2000, PhD thesis, Max-Planck-Institut fur Astrophysik

Reach, W. T. & Rho, J. 1996, A&A, 315, L277

Reynolds, S. P. 2008, ARAA, 46, 89

Reynoso, E. M., Hughes, J. P., & Moffett, D. A. 2013, AJ, 145, 104

Rho, J., Jarrett, T. H., Cutri, R. M., & Reach, W. T. 2001, ApJ, 547, 885

Rodríguez-González, A., Velázquez, P. F., Rosado, M., Esquivel, A., Reyes-Iturbide, J., & Toledo-Roy, J. C. 2011, ApJ, 733, 34

Rybicki, G. & Lightman, A. 1984, Radiative Processes in Astrophysics (Wiley-VCH)

Scalo, J. & Elmegreen, B. G. 2004, ARAA, 42, 275

Schlickeiser, R. 2002, Cosmic Ray Astrophysics (Springer)

Schure, K. & Bell, T. 2012, 370 years of Astronomy in Utrecht

Schure, K., Kosenko, D., Kaastra, J., Keppens, R., & Vink, J. 2009a, A&A, 508

Schure, R., Vink, J., Achterberg, A., & Keppens, R. 2009b, Advances in Space Research, 44, 433

Sedov, L. 1946, Journal of Applied Mathematics and Mechanics, 10, 241

Smith, B., Sigurdsson, S., & Abel, T. 2008, MNRAS, 385

Spitkovsky, A. 2008, ApJL, 682

Stecker, F. 1971, Cosmic Gamma Rays (NASA)

Stone, J., Gardiner, T., Teuben, T., Hawley, J., & Simon, J. 2008, ApJSS, 178, 137

Strong, A., Moskalenko, I., & Ptuskin, V. 2007, Ann. Rev. Nucl. Part. Sci., 57, 285

Sutherland, M. & Dopita, M. 2005, Astrophysics of the Diffuse Universe (Springer)

Sutherland, R. & Dopita, D. 1993, ApJSS, 88

Taylor, J. 1955, Philosophical Magazine, 46, 317

Teşileanu, O., Mignone, A., & Massaglia, S. 2008, AA, 488, 429

Toledo-Roy, J. C., Esquivel, A., Velzquez, P. F., & Reynoso, E. M. 2014, 442, 229

Toro, E. 2009, Riemann Solvers and Numerical Methods for Fluid Dynamics: A Practical Introduction (Springer)

Truelove, J. K. & McKee, C. F. 1999, ApJS, 120, 299

van Veelen, B., Langer, N., Vink, J., García-Segura, G., & van Marle, A. J. 2009, A&A, 503, 495

Vasiliev, E. 2013, MNRAS, 431, 638

Vasiliev, E. O., Nath, B. B., Bondarev, R., & Shchekinov, Y. 2015, MNRAS, 446, 1703

Vink, J. 2006, in ESA Special Publication, Vol. 604, The X-ray Universe 2005, ed. A. Wilson, 319

Vink, J. 2012, Astron Astrophys Rev, 20

Völk, H. J., Berezhko, E. G., & Ksenofontov, L. T. 2005, A&A, 433, 229

Walitt, L. Liu, C. & Harp, J. 1978, SAE Technical Paper

Walter, M. & Wolfendale, A. W. 2012, Euro. Phys. J. H., 37, 323

Webber, W., McDonald, F., Higbie, P., & Heikkila, B. 2011, arxiv.org/1111.2377

Weiler, K. W. & Sramek, R. A. 1988, ARAA, 26, 295

Whalen, D., van Veelen, B., O'Shea, B. W., & Norman, M. L. 2008, ApJ, 682, 49

Wulf, T. 1910, Phys. Z., 10, 152

Yanenko, N. 1971, The Method of Fractional Steps (Springer)

Yoshiike, S., Fukuda, T., Sano, H., Moribe, N., Torii, K., Hayakawa, T., Okuda, T., Yamamoto, H., & Tajima, H. 2013, ApJ, 768

Zatsepin, G. T. & Kuz'min, V. A. 1966, Soviet Journal of Experimental and Theoretical Physics Letters, 78

Zhang, W., Howell, L., Almgren, A., Burrows, A., & Bell, J. 2011, ApJS, 196, 20

Zirakashvili, V. N. & Ptuskin, V. S. 2009, Proceedings of the 31st ICRC

—. 2012, Astropart. Phys., 39, 12